Manganese promotion of a Co/SiO_2 Fischer-Tropsch catalyst

Dissertation

in partial fulfilment for the degree of

MSc Chemical Engineering

by

Silethukuthula Mathe

Supervisor: Professor Eric Van Steen

Catalysis Institute

Department of Chemical Engineering

University of Cape Town

2021

Plagiarism declaration

I, Silethukuthula Mathe, declare that I am the sole author of this dissertation, except for the information gathered from literature and my supervisor, I received no assistance from anyone. Both contributions to other people's work, as well as quotations, have been cited and referenced.

Signed by candidate

Signature: Date: 30 April 2021

Acknowledgements

I would like to express my deep and sincere gratitude to my research supervisor, Prof. Eric van Steen, who has given me the opportunity to pursue research. His valuable support and guidance throughout the whole project are highly appreciated. Furthermore, his constructive criticism and motivation have deeply shaped me into a better individual. He has taught me to carry out research efficiently and with an open mind. It was great privilege and honour to be under his guidance and supervision. I am extremely grateful for what he has offered me.

Many thanks to Dr. Gerard Leteba. He supported me emotionally throughout this journey. He has been my pillar of strength. I am very grateful for his love, care and sacrifices.

I would like to thank the Catalysis Research Institute staff and students for making the working environment a jolly place to work in. Moreover, I would like to thank DST-NFT Centre of Excellence in Catalysis (c*change) for the financial support, which made this research possible.

Finally, I would like to express my gratitude to my cousin, Monalisa Mathe, for her unwavering support throughout this journey. I am extremely grateful for her kindness and for being my Aunt Dora whenever I felt like throwing in the towel. Thank you so much for believing in me.

Abstract

This study tests the hypothesis that the incorporation of manganese into cobalt-based/silica (SiO_2) catalyst influences the activity and selectivity of the Fischer-Tropsch synthesis via the enhancement of CO adsorption and dissociation. The base catalyst is prepared by impregnation (IMPR) of the SiO_2 support with cobalt(II) nitrate hexahydrate followed by calcination at 230 °C under a continuous flow of air. This IMPR approach resulted in the successful formation of well-defined and monodisperse cobalt nanoclusters over SiO_2 support material. The catalyst precursor containing 22 wt.% Co/SiO_2 were doped with different manganese concentrations using strong electrostatic adsorption (SEA) and IMPR approaches. The physico-chemical properties of the catalyst precursors were characterised using ICP-OES, XRD, TEM, STEM-EDS, H_2-TPR, TGA, H_2 chemisorption and CO-TPD. The catalytic performances of the reduced catalysts in the Fischer-Tropsch synthesis were tested in a fixed bed reactor at 220 °C and 20 barg with $(H_2/CO)_{inlet} = 2$.

The incorporation of small amounts of manganese into the Co/SiO_2 catalyst precursor, via SEA, resulted in enhanced catalytic activity and this was attributed to the higher degree of cobalt reduction obtained with these materials. However, high manganese contents resulted in decreased catalytic performance, which may be associated with the blockage of catalytically active, cobalt surface sites. There was no evidence of enhanced CO adsorption and dissociation over Co/SiO_2 catalyst as a result of the inclusion of selectively adsorbed manganese. Furthermore, the addition of selectively adsorbed manganese on Co/SiO_2 catalyst did not significantly change the CH_4, C_{2-4} and C_{5+} selectivities. The olefin content was the lowest with very small amount of manganese when compared to unpromoted cobalt catalyst, however, a further increase in manganese concentration resulted in an increased olefin content. Lastly, changing the doping method from SEA to IMPR (without pH adjustment) did not significantly change the activity and selectivity of cobalt catalysts. Thus, the change in the method of doping did not influence the activity and selectivity of the cobalt-based catalysts.

Contents

Plagiarism declaration ii
Acknowledgements iii
Abstract iv
LIST OF TABLES vii
LIST OF FIGURES ix
NOMENCLATURE xii
1 INTRODUCTION 1
2 LITERATURE REVIEW 4
2.1 The Fischer-Tropsch synthesis 4
2.2 Conditions for the Fischer-Tropsch synthesis 6
2.3 Fischer-Tropsch selectivity 7
2.4 Catalysts for the Fischer-Tropsch synthesis 8
2.5 Catalyst promoters 11
2.5.1 Manganese promotion of cobalt-based Fischer-Tropsch catalysts 12
2.6 Aim of the study 17
2.6.1 Hypothesis 17
2.6.2 Key Questions 18
3 EXPERIMENTAL PROCEDURE 19
3.1 Discussion of method and programme 19
3.2 Catalyst preparation 19
3.3 Catalyst characterisation 20
3.4 Catalytic testing 26
3.4.1 Catalyst reduction 29
3.4.2 Start-up of the Fischer-Tropsch synthesis 29
3.4.3 Product Analysis 30
4 RESULTS 34
4.1 Inductively coupled plasma optical emission spectroscopy (ICP-OES) 34
4.2 Powder X-ray diffraction (PXRD) 36
4.3 Transmission electron microscopy (TEM) 38

4.4 Scanning transmission electron microscopy coupled with energy dispersive X-ray spectroscopy (STEM-EDS) 41
4.5 Temperature programmed reduction (TPR) 42
4.6 Thermogravimetric analysis (TGA) 44
4.7 Hydrogen chemisorption 46
4.8 Temperature programmed desorption of CO (CO-TPD) 48
4.9 Fischer-Tropsch synthesis 53
4.10 Performance of Mn-promoted Co/SiO_2 prepared by impregnation 72
5 DISCUSSION 78
5.1 Effect of Mn promotion on Co particle size distribution 78
5.2 Effect of Mn on reducibility of Co 79
5.3 Effect of Mn promotion on CO and H_2 adsorption 79
5.4 Effect of manganese on activity 80
5.5 Effect of manganese on chain growth probability 81
5.6 Effect of manganese on product selectivity 82
5.7 Effect of preparation method on activity 83
5.8 Effect of preparation method on Fischer-Tropsch product selectivity 84
6 CONCLUSIONS AND RECOMMENDATIONS 85
7 REFERENCES 87
8 APPENDICES 97
9 ETHICS CLEARANCE FORM 131

LIST OF TABLES

Table 2.1: Current commercial Fischer-Tropsch operating plants in the world (Energy database, 2014; van de Loosdrecht *et al.,* 2013). 5

Table 2.2: Differences between fixed bed reactor and a slurry bed reactor (extracted from Tijmensen *et al.,* 2002). 6

Table 2.3: Fischer-Tropsch comparison of cobalt and iron (Khodakov *et al.,* 2007; van Steen *et al.,* 2018)..... 9

Table 3.1: Microwave digester conditions. 21

Table 3.2: The amount of H_2 adsorbed to form a monolayer and equilibrium constants obtained from modelling H_2 adsorption Langmuir isotherm via linear regression. 24

Table 3.3: Fischer-Tropsch synthesis conditions. 30

Table 3.4: GC-TCD operating conditions. 31

Table 3.5: Standard gas composition mixture. 31

Table 3.6: GC-FID operating conditions..... 32

Table 4.1: Summary of the elemental compositions determined using ICP-OES, before and after exposing the catalyst precursors to a solution of $KMnO_4$ containing different manganese concentration ($[Mn]_{initially}$, mg/L) at pH = 1 for 1 hr, followed by washing and calcination at 230 °C in flowing air. 34

Table 4.2: Summary of the crystalline domain sizes of Co_3O_4 in the calcined Mn-Co/SiO_2 catalyst precursor prepared using strong electrostatic adsorption (SEA) from a $KMnO_4$ solution at pH = 1 (Co loading = 22 wt.%). 38

Table 4.3: Mean sizes of Co_3O_4 nanoclusters in the calcined Mn-Co_3O_4/SiO_2 catalyst precursor prepared using strong electrostatic adsorption (SEA) from a $KMnO_4$ solution at pH = 1 (Co loading = 22 wt.%). 40

Table 4.4: H_2 consumption during TPR experiments for Mn^{SEA}-Co/SiO_2 catalysts (m = 0.1 g, ramp rate 10 C/min in 5% H_2/Ar (50 ml (NTP)/min). 44

Table 4.5: Degree of reduction of Mn-Co/SiO_2 catalysts prepared using strong electrostatic adsorption (SEA) after reduction for 4 hrs in 5% H_2/N_2 at 350 °C..... 46

Table 4.6: H_2 chemisorption summary results for Mn^{SEA}-Co/SiO_2 reduced at 350 °C for 4 hrs in pure H_2. 48

Table 4.7: Summary of H_2 and CO outlet flowrate for unpromoted cobalt catalyst at pseudo steady state..... 54

Table 4.8: Reactions carried out at T = 220 °C, P = 20 barg and H_2/CO = 2 with 0.5 g of each Mn^{SEA}-Co/SiO_2 catalyst loaded in a fixed bed reactor. 56

Table 4.9: Performance of unpromoted cobalt catalyst: Mn0 at steady state under Fischer-Tropsch conditions. 59

Table 4.10: Summary of CO-conversion and selectivities of Mn^{SEA}-Co/SiO_2 catalysts at steady state under Fischer-Tropsch conditions. 69

Table 4.11: H_2 uptake from H_2 chemisorption measurements for Mn-Co/SiO_2 catalysts prepared by IMPR (catalysts reduced at 350 °C for 4 hrs in pure H_2). 72

Table 4.12: Reactions carried out at T = 220 °C, P = 20 barg and H_2/CO = 2 with 0.5 g of each Mn^{IMPR}-Co/SiO_2 catalyst loaded in a fixed bed reactor. 73

Table 4.13: Comparison of the pseudo steady state catalytic activity obtained with manganese promoted cobalt-based Fischer-Tropsch catalysts prepared via IMPR. 77

Table 5.1: Stoichiometric ratio for the adsorption of H_2 and CO on Mn-Co/SiO_2 catalysts prepared using strong electrostatic adsorption (SEA). 80

Table 5.2: Catalytic performances of Mn^{SEA}-Co/SiO_2 catalysts at pseudo steady state obtained with manganese promoted cobalt-based Fischer-Tropsch catalysts. 81

Table 5.3: Fischer-Tropsch synthesis catalytic performance of Mn^{SEA}-Co/SiO_2 catalysts at 220 °C, 20 barg, syngas flowrate of 60 ml (NTP)/min and H_2/CO ratio of 2, at pseudo steady state. 82

Table 5.4: Comparison of the pseudo steady state catalytic activity obtained with manganese promoted cobalt-based Fischer-Tropsch catalysts at different manganese loadings, prepared using SEA and IMPR approaches. 83

Table 5.5: Comparison of selectivities of Mn-Co/SiO_2 catalysts towards hydrocarbons at pseudo steady state obtained using different manganese loadings, prepared using SEA and IMPR approaches. 84

Table 8.1: H_2 mass flow calibration measurements at different set points. 98

Table 8.2: CO mass flow calibration measurements at different set points. 99

Table 8.3: N_2 mass flow calibration measurements at different set points. 100

Table 8.4: Summary results from the loop calibration calculations. 103

Table 8.5: Peaks obtained from 5% H_2/Ar pulse chemisorption. 104

Table 8.6: Peaks obtained from CO pulse chemisorption. 107

Table 8.7: Internal calibration factors in CO pulse chemisorption for Mn^{SEA}-Co/SiO_2. 107

Table 8.8: A summary of peak areas (A) for $Mn26^{SEA}$-Co/SiO_2 obtained from a gaussian model. 109

LIST OF FIGURES

Figure 1.1: Cost contributions for each BTL plant section (Boerrigter, 2006). 2

Figure 2.1: Product selectivity (in wt.%) as a function of the chain growth probability (extracted from Claeys & van Steen, (2004)). 8

Figure 3.1: Process instrumentation diagram (PID) of the laboratory test unit..... 27

Figure 3.2: Cross sectional view of an ampoule sampler extracted from Schulz *et al.* (1984). 28

Figure 3.3: Schematic diagram of how the fixed bed reactor was packed (not drawn to scale). 29

Figure 4.1: Manganese uptake by the catalyst precursor, Co_3O_4/SiO_2, exposed to SEA solution at pH = 1 containing different manganese concentrations for 1 hr, followed by washing and calcining at 230 °C in flowing air (●: initial manganese concentration in the SEA-solution; ▲: calculated manganese concentration in the final solution)..... 36

Figure 4.2: XRD patterns of Co_3O_4/SiO_2 with different manganese loadings prepared using strong electrostatic adsorption (SEA). 37

Figure 4.3: TEM bright field (TEM-BR) images of the calcined catalyst precursor before and after exposing to a $KMnO_4$ solution at pH = 1 for 1 hr, followed by washing and calcining at 230 ℃ in flowing air: (a) Mn0, (b) $Mn16^{SEA}$, (c) $Mn26^{SEA}$, (d) $Mn42^{SEA}$ and (e) $Mn55^{SEA}$ nanostructures. Inserts are enlarged TEM-BR micrographs of these Co_3O_4-based structures showing the spherical nanoclusters of single crystals. 39

Figure 4.4: Log-normal distributions of the measured sizes of 300 nanoclusters: (a) Mn0, (b) $Mn16^{SEA}$, (c) $Mn26^{SEA}$, (d) $Mn42^{SEA}$ and (e) $Mn55^{SEA}$. 40

Figure 4.5: (a-c) HAADF images (first column), cobalt distribution (second column, blue), manganese distribution (the last column, green) in (a) Mn0, (b) $Mn42^{SEA}$ and (c) $Mn55^{SEA}$ showing homogeneous distributions on Co_3O_4/SiO_2 prepared using strong electrostatic adsorption (SEA). 41

Figure 4.6: H_2-TPR profiles of calcined Mn-Co/SiO_2 catalysts with different Mn loadings prepared using strong electrostatic adsorption (SEA). 43

Figure 4.7: TGA weight loss curves for reduction of Co_3O_4/SiO_2 in 5% H_2/N_2 mixture for 4 hrs with different manganese loadings prepared using strong electrostatic adsorption (SEA). 45

Figure 4.8: Adsorption isotherms (blue dots) and Langmuir adsorption fitted isotherms (solid black line) for manganese promoted cobalt catalysts prepared using strong electrostatic adsorption (SEA): (a) Mn0, (b) $Mn16^{SEA}$, (c) $Mn26^{SEA}$, (d) $Mn42^{SEA}$ and (e) $Mn55^{SEA}$..... 47

Figure 4.9: CO and CO_2 profiles of $Mn16^{SEA}$ as detected using a mass spectrometer. 49

Figure 4.10: CO-TPD profile of Mn-Co/SiO_2 samples prepared using strong electrostatic adsorption (SEA) with different manganese loadings. 50

Figure 4.11: Total amount of CO adsorbed as a function of manganese loading in catalysts prepared using strong electrostatic adsorption (SEA). 51

Figure 4.12: Maximum peak temperature for each peak in the CO-TPD profile for Mn-Co/SiO_2 catalysts prepared using strong electrostatic adsorption (SEA). 52

Figure 4.13: Area ratio of the high temperature peak in the CO-TPD relative to the total area as a function of the manganese loading in the calcined catalysts prepared using strong electrostatic adsorption (SEA). 53

Figure 4.14 54

Figure 4.15: H_2 and CO flowrate with respect to time for Mn^{SEA}-Co/SiO_2 catalysts with different manganese concentrations in 50 ml of potassium permanganate solution: (a) Mn0 , (b) $Mn16^{SEA}$, (c) $Mn26^{SEA}$, (d) $Mn42^{SEA}$ and (e) $Mn55^{SEA}$ at 220 °C, 20 barg, an H_2/CO ratio of 2, and syngas flowrate of 60 ml(NTP)/min. 55

Figure 4.16: CO-conversion of the unpromoted cobalt supported on silica (Mn0; 0.5 g) at 220 °C, 20 barg, syngas flowrate of 60 ml (NTP)/min, and H_2/CO of 2: R1 (first reaction) and R2 (repeated reaction). 57

Figure 4.17: CH_4 selectivity of the unpromoted cobalt supported on silica (Mn0; 0.5 g) at 220 °C, 20 barg, syngas flowrate of 60 ml (NTP)/min, and H_2/CO of 2: R1 (experiment 1) and R2 (repeated experiment). 58

Figure 4.18: CO_2 selectivity of the unpromoted cobalt supported on silica (Mn0; 0.5 g) at 220 °C, 20 barg, syngas flowrate of 60 ml (NTP)/min, and H_2/CO of 2: R1 (experiment 1) and R2 (repeated experiment). 59

Figure 4.19: Time-dependency of CO-conversion obtained over Mn-Co/SiO_2 at 220 °C, 20 barg, syngas flowrate of 60 ml (NTP)/min, and H_2/CO of 2. (a) Mn0, (b) $Mn16^{SEA}$, (c) $Mn26^{SEA}$, (d) $Mn42^{SEA}$ and (e) $Mn55^{SEA}$. 62

Figure 4.20: Time-dependency of CH_4 selectivity obtained over Mn^{SEA}-Co/SiO_2 catalysts ((a) Mn0, (b) $Mn16^{SEA}$, (c) $Mn26^{SEA}$, (d) $Mn42^{SEA}$ and (e) $Mn55^{SEA}$) at 220 °C, 20 barg, syngas flowrate of 60 ml (NTP)/min, and H_2/CO of 2. 64

Figure 4.21: Time-dependency of CO_2 selectivity obtained over Mn^{SEA}-Co/SiO_2 ((a) Mn0, (b) $Mn16^{SEA}$, (c) $Mn26^{SEA}$, (d) $Mn42^{SEA}$ and (e) $Mn55^{SEA}$) catalysts prepared using strong electrostatic adsorption (SEA) in the Fischer-

Tropsch synthesis at 220 °C, 20 barg, syngas flowrate of 60 ml (NTP)/min, and H_2/CO of 2..... 66

Figure 4.22: The ASF plots obtained over Mn-Co/SiO_2 catalysts: (a) Mn0, (b) $Mn16^{SEA}$, (c) $Mn26^{SEA}$, (d) $Mn42^{SEA}$ and (e) $Mn55^{SEA}$..... 68

Figure 4.23: Total olefin content in the fraction of linear hydrocarbons as a function of carbon number for Mn-Co/SiO_2 catalysts prepared using strong electrostatic adsorption (SEA). 70

Figure 4.24: 1-olefin content in the fraction of linear olefins as a function of carbon number for Mn-Co/SiO_2 catalysts prepared using strong electrostatic adsorption (SEA)..... 71

Figure 4.25: H_2 and CO flowrate with respect to time for Mn^{IMPR}-Co/SiO_2 catalysts prepared by impregnating manganese(II) acetate tetrahydrate on pre-formed Co_3O_4/SiO_2 with no pH adjustments: (a) $Mn16^{IMPR}$ and (b) $Mn26^{IMPR}$ at 220 °C, 20 barg and an H_2/CO ratio of 2 and syngas flowrate of 60 ml (NTP)/min. 73

Figure 4.26: Time-dependency of CO-conversion obtained over $Mn16^{SEA}$ and $Mn26^{SEA}$ compared with $Mn16^{IMPR}$ and $Mn26^{IMPR}$ with manganese loading of 0.16 wt.% and 0.26 wt.% respectively at 220 °C, 20 barg, syngas flowrate of 60 ml (NTP)/min and an H_2/CO of 2..... 74

Figure 4.27: Time-dependency of CH_4 selectivity obtained over $Mn16^{IMPR}$ and $Mn26^{IMPR}$ at 220 °C, 20 barg, syngas flowrate of 60 ml (NTP)/min and H_2/CO of 2..... 75

Figure 4.28: Time-dependency of CO_2 selectivity over $Mn16^{IMPR}$ and $Mn26^{IMPR}$ in the Fischer-Tropsch synthesis at 220 °C, 20 barg, syngas flowrate of 60 ml (NTP)/min, and an H_2/CO of 2. 76

Figure 4.29: ASF plots obtained with $Mn16^{IMPR}$ and $Mn26^{IMPR}$. 77

Figure 8.1: Fixed bed reactor temperature profile with R1 = the first experiment and R2 = the repeated experiment. 97

Figure 8.2: H_2 mass flow calibration curve..... 99

Figure 8.3: CO mass flow calibration curve. 100

Figure 8.4: N_2 mass flow calibration curve..... 101

Figure 8.5: H_2-TPR profile of Mn0-Co/SiO_2. 105

Figure 8.6: CO-TPD profile for $Mn26^{SEA}$-Co/SiO_2 showing deconvoluted peaks. .. 108

NOMENCLATURE

Term	Description
LTFT	Low Temperature Fischer-Tropsch
TEM	Transmission Electron Microscopy
XRD	Powder X-Ray Diffraction
ICP-OES	Inductively Coupled Plasma Optical Emission Spectroscopy
STEM EDS	Scanning Transmission Electron Microscopy Energy-Dispersive X-Ray Spectroscopy
TPR	Temperature Programmed Reduction
TPD	Temperature Programmed Desorption
GC-TCD	Gas Chromatogram equipped with a Thermal Conductivity detector
GC-FID	Gas Chromatogram equipped with a Flame Ionisation Detector
SF	Stoichiometric Factor
DoR	Degree of Reduction
TGA	Thermogravimetric Analysis
FT	Fischer-Tropsch
SSITKA	Steady State Isotopic Transient Kinetic Analysis

1 INTRODUCTION

Transportation fuels are typically produced from crude oil, which is extracted from the ground and refined into liquid fuels in oil refineries such as Astron Energy in Cape Town, South Africa with heavy gas oil often used as a source of energy for generating electricity. As a feedstock, crude oil is also used for the production of essential chemical products. However, the concentration of greenhouse gases, including CO_2 and methane, due to combustion of crude oil has been the main contributor to the rising CO_2 concentrations in the atmosphere, resulting in global climate change. Thus, this has led to a fast-growing interest in the use of alternative sources of energy such biomass/waste to supplement the products made from crude oil (Owusu & Asumadu-Sarkodie, 2016).

The potential of biomass to serve as a renewable source of carbon-neutral fuel to supplement products made from crude oil has been well recognized (Owusu & Asumadu-Sarkodie, 2016: Roddy, 2012). Biomass is attractive because it is a renewable resource, it has an overall positive environmental impact and it has a potential of improving the economic growth for local communities (Maji *et al*., 2019; Owusu & Asumadu-Sarkodie, 2016).

The biomass-to-liquid (BTL) process offers an opportunity to obtain carbon-neutral fuels from biomass (Liu *et al.,* 2011). The BTL-process proceeded through 3 distinctly different generations. The first generation includes the production of biodiesel, bioethanol or biogas via transesterification of food sources such as vegetable oils or animal fats. The first generation BTL-process is, however, associated with many concerns, such as feedstock requirements and land availability (Dimitriou *et al.,* 2018). More arable agricultural land is needed for large-scale feedstock processing, resulting in reduced terrain for humans and animal food production (Dimitriou *et al.,* 2018; Naik *et al.,* 2010). The second generation BTL-processes have been introduced to stop utilizing food resources (Dimitriou *et al.,* 2018) and may use a wide variety of biomass feedstock from various industries such as agriculture, horticulture, forestry, paper and wastes such as municipal solid waste (Dimitriou *et al.,* 2018). Algal biomass is linked to the third generation of BTL-processes, which can be linked to the use of CO_2 as feedstock (Lee & Lavoie, 2013). This study will consider the manufacture of second generation liquid fuels from gasification of non-food biomass/waste to synthesis gas, which may generate a synthesis gas with $H_2/CO=2$. After a water gas shift process to adjust the H_2/CO ratio to ca. 2 for the Fischer-Tropsch synthesis, the synthesis gas is converted into liquid fuels using the Fischer-Tropsch process (Claeys & van Steen, 2004). Fischer-Tropsch synthesis is an industrial process that converts synthesis gas

into a wide range of carbon-based products such as diesel, petrol, jet fuel, wax, and chemicals (Dry, 2002).

The BTL-process, however, faces significant challenges. BTL plants are typically limited in scale due to biomass needing to be either obtained locally or transported at a significant cost (Boerrigter, 2006). Thus, ideally, a BTL plant should be designed to operate at small to medium scale within proximity to the feedstock i.e. biomass (Tucker & van Steen, 2020). However, operating at small to medium scale impacts the economy of scale of this highly capital-intensive process and, thus, it is critical to minimize capital costs to ensure economic viability.

Figure 1.1 illustrates the estimate of the capital costs for a BTL plant. Syngas production (air separation and gasification) is responsible for the largest proportion of the BTL plant investment costs with air separation unit contributing significantly towards the plant investment (Rostrup-Nielsen, 2002; Aasberg-Petersen *et al.,* 2003). Thus, Rostrup-Nielsen, (2002) suggested using air instead of pure oxygen in the gasification section. This will reduce the investments costs for Fischer-Tropsch processes. However, this is only possible if the Fischer-Tropsch unit operates in a single pass without recycling the unreacted products as the syngas contains a large volume of N_2 (Rostrup-Nielsen, 2002). This is to ensure that there is no build-up of N_2 in the system. Therefore, the Fischer-Tropsch unit must operate at a high conversion, for the overall process to be economically viable.

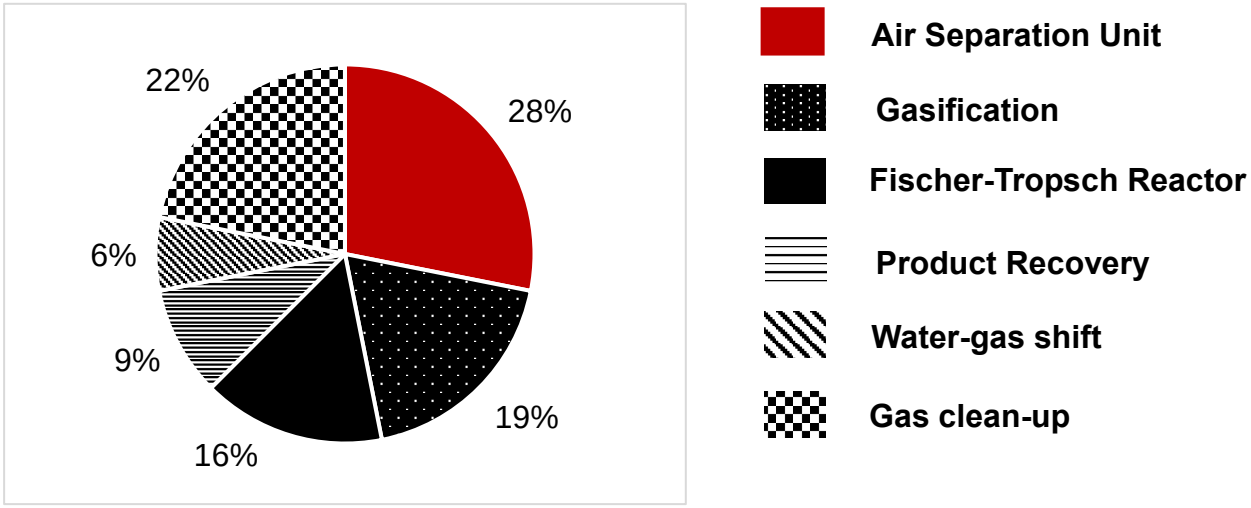

Figure 1.1: Cost contributions for each BTL plant section (Boerrigter, 2006).

The problem with operating the Fischer-Tropsch synthesis at high conversion is the high partial pressure of H_2O and low partial pressures of CO and H_2 within the reactor, which results in high selectivity towards undesired by-products. It was observed that

high conversion over a cobalt-based Fischer-Tropsch catalyst results in high methane selectivity (Tucker & van Steen, 2020). As such, the use of manganese as a promoter in cobalt-based Fischer-Tropsch catalysts was suggested. Studies have shown that the addition of manganese on a cobalt-based Fischer-Tropsch catalyst decreases methane and CO_2 selectivity, increases C_{5+} selectivity (Bezemer *et al.*, 2006; Morales *et al.*, 2007; Dinse *et al.*, 2012; Johnson *et al.*, 2015) and enhances activity of the cobalt-based catalysts (Dinse *et al.,* 2012; Johnson *et al.,* 2015).

2 LITERATURE REVIEW

2.1 The Fischer-Tropsch synthesis

The Fischer-Tropsch synthesis is a catalytic hydrogenation of carbon monoxide yielding long chain hydrocarbons (Dry, 2002). This reaction is facilitated via monomer units formed on the surface of the catalyst from synthesis gas (CO + H_2). The monomers are subsequently polymerized to produce a wide range of products containing mainly paraffins from C_1 to C_{40} and oxygenated compounds (Dry, 2002). In a Fischer-Tropsch environment, simultaneous chemical reactions take place to generate both desired and undesired products.

Table 2.1 below shows the current commercial plants of Fischer-Tropsch synthesis. Despite the fact that the Shell Pearl Plant appears to be world's largest commercial Fischer-Tropsch plant (260 000 bpd), it should be noted that 140 000 bpd is Fischer-Tropsch gas-to-liquid products, whilst the remainder are liquid products in natural gas (C_{2+}), and thus not Fischer-Tropsch derived products. As a result, Sasol Secunda, with capacity of 160 000 bpd is the leading commercial Fischer-Tropsch plant.

Table 2.1: Current commercial Fischer-Tropsch operating plants in the world (Energy database, 2014; van de Loosdrecht *et al.,* 2013).

Plant Name	Location	Products	Liquid Capacity (bpd)	Catalyst used	Start Operation
Escravos	Nigeria	Naphtha, kerosene, Diesel, paraffins and lubricants	34 000	Co/Al_2O_3	2014
Pearl	Qatar	Naphtha, kerosene, Diesel, paraffins and lubricants	260 000	Co/TiO_2	2011
Bintulu	Malaysia	Naphtha, Kerosene, Diesel, paraffins, lubricants and waxes	14 700	Co/TiO_2, Co/SiO_2	1993
Oryx	Qatar	Naphtha and diesel	34 000	Co/Al_2O_3	2006
Mossel Bay	South Africa	Kerosene, Gasoline, diesel, lubricants, and chemicals	36 000	Fused Fe/K	1993
Sasol Secunda	South Africa	Kerosene, Gasoline, diesel, lubricants, and chemicals	160 000	Fused Fe/K	1972
Sasol Sasolburg	South Africa	Waxes and chemicals	3 000	Precipitated Fe/K	1955
Shenhua Ningmei/ Ningxia Hui	China	Kerosene, Gasoline, diesel, lubricants, waxes and chemicals	100 000	Fe	2006
Niquan GTL	Trinidad and Tobago	Diesel, naphtha, kerosene, base oils, waxes, LPG	2 400	Co	2008
Yitai CTL	China	Diesel, naphtha, kerosene, base oils, waxes, LPG	25 000	Fe	2009
Yitai Ürümqi CTL	China	Diesel, naphtha, kerosene, base oils, waxes, LPG	46 000	Fe	2016
Yitai Ordos CTL	China	Diesel, naphtha, kerosene, base oils, waxes, LPG	46 000	Fe	2016
Yitai Hangjinqi CTL	China	Diesel, naphtha, kerosene, base oils, waxes, LPG	23 200	Fe	2017

2.2 Conditions for the Fischer-Tropsch synthesis

Fischer-Tropsch synthesis uses H_2 and CO at a stoichiometric ratio of ca. 2:1 (Dry, 2002; Tijmesen *et al.,* 2002) and typically operates at a pressure of 20-40 barg and a temperature of 180-250 °C (Tijmesen *et al.,* 2002). The activity and selectivity of Fischer-Tropsch catalysts are affected by a variety of factors such as reaction temperature, reaction pressure, feed composition (ratio of H_2/CO), catalyst particle size, residence time, flowrates and choice of reactor. A small alteration of any of these parameters is enough to alter the activity and selectivity of Fischer-Tropsch catalysts, therefore, these parameters should be closely monitored (Claeys & van Steen, 2004; Makhura *et al.,* 2019).

As mentioned above, type of reactor plays a role in the performance of the Fischer-Tropsch catalyst. There are three main kinds of FT reactors used, viz. fluidised reactor, fixed bed reactor, and a slurry reactor (Dry, 2002; Tijmesen *et al.,* 2002). The slurry reactor is widely used in industry because it is simple to construct, has excellent heat/mass transfer rates with low energy input, thus making it ideal for gas-to-liquid processes (Wang *et al.,* 2007). The difficulty in separating catalyst and fluid in slurry reactors is, however, a disadvantage. The slurry reactor allows for online catalyst removal and addition, which reduces downtime. However, in-situ regeneration can be used in the fixed fed reactor to reduce catalyst consumption and avoid an extensive unloading-reloading procedure (Rytter & Holmen, 2015).

Table 2.2: Differences between fixed bed reactor and a slurry bed reactor (extracted from Tijmensen *et al.,* 2002).

	Fixed bed reactor	**Slurry bed reactor**
Economic O & M	Maintenance and labour intensive. In-situ-regeneration can be used to keep catalyst active	Lower down time due to lower catalyst replacement
Economics of scale	Easily scalable (multiplying of tubes)	Possible, but difficult
Conversion efficiency (once through conversion)	Max of 80 %	Increased overall conversion
C_{5+} selectivity	>90%	>90%
Pressure drop	3-7 bar	< 1 bar
Technical aspects; Wax/catalyst separation	Performed easily and at low costs	More difficult for commercial application
Status	Technology verified	Technology verified

2.3 Fischer-Tropsch selectivity

The Fischer-Tropsch synthesis yields a wide range of hydrocarbons. The selectivity towards the hydrocarbon products is governed by the Anderson-Schulz-Flory distribution and the chain growth probability (Claeys & van Steen, 2004).

A mathematical model representing the Fischer-Tropsch distribution has been developed by a number of scholars, with Anderson-Schulz-Flory (ASF) distribution being the most fundamental kinetic model (Claeys & van Steen, 2004). The ASF kinetic model is based on the widely held assumption that the Fischer-Tropsch reaction is initiated by addition of a C_1 monomer. The molar product distribution can be expressed by equation 2.1. Equation 2.1 is used for surface chain growth probability (α) in ideal ASF linear products with carbon number C_N (Claeys & van Steen, 2004).

$$\mathrm{M_{C_N}} = (1-\alpha)\cdot\alpha^{C_N-1} \tag{2.1}$$

$\mathrm{M_{C_N}}$ is the molar content of the linear hydrocarbon products with carbon number, C_N, within the organic product fraction. A straight line can be observed in a semi-logarithmic plot of the molar content as a function of the carbon number, from which the chain growth probability can be estimated from the slope ($\log\alpha$)

$$\log M_{C_N} = \log\left(\frac{1-\alpha}{\alpha}\right) + C_N\cdot\log\alpha \tag{2.2}$$

The experimental product distribution for catalysts show some deviations from the ideal Anderson-Schulz-Flory distribution (Claeys & van Steen, 2004):

(a) Relatively high methane content.
(b) Relatively low C_2 molar content.
(c) A curvature of ASF distribution at low carbon numbers, suggesting chain length dependent (the chain growth probability seems to reach an asymptotic value at high carbon number).

In the ideal Anderson-Schulz-Flory distribution, the relationship between chain growth probability and hydrocarbon product selectivity is shown in Figure 2.1. The Fischer-Tropsch process aims to maximize the high-value products such as olefins, paraffins and oxygenates. When the target of the process is liquid fuels, the aim is to maximize the weight of liquid products above C_{5+} carbon compounds.

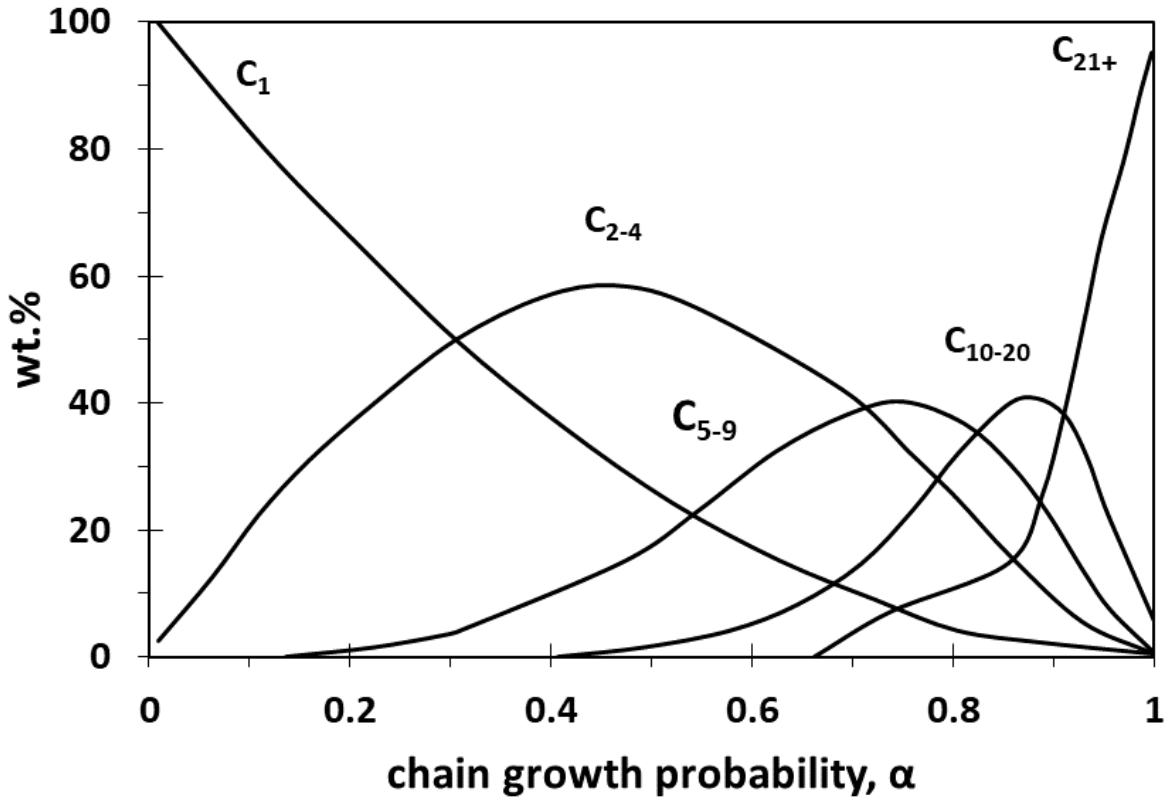

Figure 2.1: Product selectivity (in wt.%) as a function of the chain growth probability (extracted from Claeys & van Steen, (2004)).

The Anderson-Schulz-Flory distribution presumes the formation of a single product compound in the Fischer-Tropsch synthesis. However, the product contains linear olefins, n-paraffins, branched compounds, oxygenated compounds, etc. The formation of different product classes does affect the product selectivity as a function of the chain length (Ghosh *et al.*, 2020).

2.4 Catalysts for the Fischer-Tropsch synthesis

The first catalysts proposed for Fischer-Tropsch synthesis were cobalt and iron. (Fischer & Tropsch, 1925). However, ruthenium and nickel are also highly active for CO hydrogenation (Vannice, 1975). Ruthenium is rare and costly. Nickel is highly active for hydrogenation at relatively high temperatures, thus resulting in high methane selectivity, but will form nickel carbonyl and volatilize (Khodakov *et al.,* 2007) when operating at low temperatures with a relatively high partial pressure of synthesis gas.

Both iron-based and cobalt-based catalysts have been used industrially in the Fischer-Tropsch synthesis. Table 2.3 gives a brief comparison of cobalt and iron catalysts.

Cobalt catalysts are more costly, however, they are less susceptible to deactivation (Khodakov *et al.,* 2007). Although low-conversion productivity is comparable for both iron and cobalt-based catalysts (van Steen *et al.*, 2018), high conversion productivity is more important for cobalt catalysts (Khodakov *et al.,* 2007; van Steen *et al.*, 2018).

Table 2.3: Fischer-Tropsch comparison of cobalt and iron (Khodakov *et al.,* 2007; van Steen *et al.,* 2018).

Parameter	Cobalt catalysts	Iron catalysts
Cost	More expensive	Less expensive
Lifetime	Months to years	Several weeks effective life
Activity at low conversion	Comparable	
Productivity at high conversion	Higher	Lower
Water gas shift reaction	Not very significant: noticeable at higher conversion	significant
H_2/CO ratio	~2	0.5-2.5
Attrition resistance	Good	Not very resistant

The cobalt-based catalyst serves as an optimal choice for producing long-chain hydrocarbons in the low temperature Fischer-Tropsch (LTFT). This is due to the fact that it has a low water gas shift activity. It should be noted that the inclusion of MnO introduces water gas shift activity, which is not common in most FT cobalt catalysts (Riedel *et al.,* 1999). Additionally, cobalt has a high activity as well as a long catalyst life cycle and its ability to selectively form linear paraffins (Dry, 2002). There are several industries that use cobalt-based catalysts in the Fischer-Tropsch synthesis (see Table 2.1). Since cobalt is a relatively costly metal, it is imperative to minimize the amount of cobalt used, whilst at the same time maximizing the available metal surface area of cobalt in the catalyst. Thus, cobalt is dispersed on stable, high surface area oxidic support such as Al_2O_3, SiO_2 or TiO_2 (Dry, 2002; Hashemzehi *et al.,* 2017; Oukaci *et al.,* 1999).

The technique used to synthesize cobalt catalysts and the nature of precursors used have a significant role in the catalyst structure as well as its performance (Khodakov *et al.,* 2007; Munnik *et al.,* 2015; Pedersen *et al.,* 2018). There are several ways to synthesize supported cobalt-based catalysts including, but not limited to, impregnation, precipitation and selective adsorption. Impregnation, one of the most common methods, is when oxide support is contacted with a liquid solution containing the precursor of the catalytically active metal, e.g a cobalt salt dissolved in distilled water (Munnik *et al.,* 2015). With all synthesis techniques, once the precursor is adsorbed,

the catalyst is subjected to calcination and reduction treatments to convert the metal precursor into its active metallic form, yielding nanoparticles (Arsalanfar *et al.,* 2013). Impregnation has two categories, dry (incipient wetness) impregnation, and wet (slurry) impregnation (Deraz, 2018; Munnik *et al.,* 2015).

Incipient wetness impregnation occurs when all pores of the support are filled with liquid and there is no excess moisture over and above the liquid required to fill the pores (Deraz, 2018; Munnik *et al.,* 2015). The advantage of using this method is that the metal loading is fixed, as such, no filtering is required, making it the simplest method (Arsalanfar *et al.,* 2013). It is also highly efficient and scalable.

Wet impregnation, also known as slurry impregnation, occurs with an excess amount of liquid (Deraz, 2018; Munnik *et al.,* 2015). The contacting solution has a volume that is larger than the pore volume of the support (Deraz, 2018; Munnik *et al.,* 2015). The contacting solution is mixed with the support and stirred constantly to ensure a homogenous metal distribution (Munnik *et al.,* 2015). Because the excess volume of the metal precursor is added, not all the metal precursor is deposited on the support surface. Wet impregnation is more advantageous because it is easy to prepare a layer of active matter on the catalyst's surface (Deraz, 2018). This is attributed to a change in solution transport from capillary action to the diffusion process, which takes longer (Liu *et al.,* 2009; Munnik *et al.,* 2015). Because of this, the final distribution of active components within the support is often favourable (Munnik *et al.,* 2015).

The form and structure of the support affects the dispersion, particle size and reducibility, hence the activity of cobalt-based Fischer-Tropsch catalysts (Iglesia, 1992; Iglesia, 1997; Reuel, 1984; Storstæter *et al.,* 2005). Cobalt dispersion is also influenced by the texture properties of the support such as the surface area, pore structure, and surface chemistry (Munirathinam *et al.,* 2018). High surface area supports result in high cobalt dispersion and generate highly active Fischer-Tropsch catalysts provided that there are no detrimental metal-support interactions that yield catalytically inactive species (Zowtiak & Bartholomew, 1983). The acidity of the support is considered to play a role in determining the selectivity of methane, $C_{2\text{-}4}$ and C_{5+} hydrocarbons (Johnson & Bell, 2016).

Several types of materials such as aluminium oxide, titanium dioxide, silicon oxide and carbonaceous materials have been widely used as support for cobalt catalysts in Fischer-Tropsch synthesis (Jung *et al.,* 2012; Marin *et al.,* 2014; Pan & Bukur, 2011). Alumina, silica and titania are the most commercially used supports for cobalt-based Fischer-Tropsch catalysts (Gholami *et al.,* 2020).

Silica has a high surface area, narrow pore size distribution, ordered pore structure, which at relatively high metal loadings results in high metal dispersion, reducibility, catalyst activity and thermal stability of the catalyst (Gholami *et al.,* 2017; Munirathinam *et al.,* 2018). Compared to alumina and titania support, silica has weaker metal-support interactions, which results in high reducibility of cobalt oxide (Han *et al.,* 2018).

2.5 Catalyst promoters

Promotion of catalysts involves the addition of small amount of a modifying species to modify the activity and selectivity of a catalyst (Kiskinova, 1992). Promoters can be classified as structural, textural, electronic modifier, stabilizers and catalyst-poison-resistant (Morales *et al.,* 2006). By enhancing the metal-support interactions, structural promoters are able to modify the surface properties, thereby improving the metal dispersion and number of active metals, although metal-support interactions may also induce promotional effects (Macheli *et al.*, 2020; Macheli *et al.*, 2021). Electronic promoters can modify the electron density on the catalyst surface by adding or withdrawing electron density in the valence band near the Fermi level (Morales *et al.,* 2006; Xu *et al.,* 2020). Additionally, electronic promoters may enhance the dissociation of chemical bonds of the reactants, which alters the catalytic performance. Noble metals, transition metal oxides, alkali and alkaline earth metals are typically used as promoters for cobalt-based Fischer-Tropsch catalysts (Gholami *et al.,* 2020).

Noble metals

The addition of small amounts of these noble metals promotes the reduction of Co_3O_4 and increases the number of active metal sites by hydrogen dissociation and spill over from the surface of the promoter (Shimura *et al.,* 2015; Nabaho *et al.*, 2016; Rytter *et al.,* 2018;). Platinum, ruthenium, and iridium are the most patented promoters for cobalt-based Fischer-Tropsch catalysts (de Beer *et al.*, 2014; Gholami *et al.,* 2020).

Alkali and alkaline earth metals

Alkali metals have been widely used for many industrial catalytic processes as promoters. They have extensively been used as promoters for iron-based Fischer-Tropsch catalysts to enhance catalytic activity and product selectivity (Petersen *et al.*, 2015; Tian *et al.,* 2019). Alkali metals are defined as chemical promoters for Fischer-Tropsch catalysts that increase the activity and C_{5+} selectivity and reduce methane selectivity (Gholami *et al.,* 2020). Alkalis have high basicity, and they can modify the local electron density of the transition metal, either directly or through the support (Li *et al.,* 2015; Shi *et al.,* 2018). A study of how alkali metals (Li, Na, K, Rb and Cs) affect the catalyst performance of Co/Al_2O_3 catalysts was done (Eliseev *et al.,* 2013). It was

found that there was an increase in activity and C_{5+} selectivity and a decrease in CH_4 selectivity upon addition of these alkali metals (Eliseev *et al.,* 2013). However, previous research on cobalt-based Fischer-Tropsch catalysts has demonstrated that addition of a certain concertation of alkali elements (~1000 ppm) reduced the catalytic activity and increased C_{5+} selectivity (Lillebø *et al.,* 2013; Borg *et al.,* 2011; Gaube & Klein, 2008; Balonek *et al.,* 2010; Uner, 1998). The cobalt catalyst behaviour is ascribed to the electronic effects from alkali addition, which result in decreased surface H concentrations and increased CO adsorption and dissociation (Li *et al.,* 2015; Xiong *et al.,* 2015; Jiang *et al.,* 2017; Shi *et al.,* 2018).

Transition metal oxides

Johnson & Bell, (2016) investigated the effect of different metal oxides, including Zr, Mn, La, Gd and Ce, on catalytic performance for Fischer-Tropsch synthesis using Co/SiO_2 catalyst. It was observed that for all promoted catalysts the selectivity towards CH_4 decreased and C_{5+} increased by increasing the promoter/Co ratio. Additionally, it was observed that the selectivities were insensitive to a further increase of the promoter loading. For the purposes of this study, we will zoom into manganese.

2.5.1 Manganese promotion of cobalt-based Fischer-Tropsch catalysts

Studies have shown that manganese promotion has an effect on the activity and product distribution of cobalt-based Fischer-Tropsch catalysts (Dinse *et al.,* 2012; Johnson *et al.,* 2015; Morales *et al.,* 2005). These studies investigated the catalytic performances for both unpromoted and manganese promoted cobalt-based catalysts at 493 K using different reaction pressures ranging from 1 – 20 atm with a H_2/CO feed ratio of 2:1. Dinse *et al*. (2012) and Johnson *et al*. (2015) synthesized $Mn/Co/SiO_2$ catalysts via incipient wetness impregnation. Manganese(II) acetate and cobalt(II) nitrate were used as the manganese and the cobalt source, respectively. Morales *et al*. (2005) synthesized Co/TiO_2 using homogenous deposition precipitation and incipient wetness impregnation to add manganese in the form of manganese(II) nitrate to the catalyst. Johnson *et al.* (2015) modelled the rate of reaction as a function of the reaction conditions. One of the outcomes was that the kinetic inhibition factor increased with increasing manganese content. They concluded that the strength of carbon monoxide adsorption increases, which in turn enhances the activity of manganese promoted catalysts (Dinse *et al.,* 2012; Johnson *et al.,* 2015; Morales *et al.,* 2005). This is not necessarily a valid reasoning. Fitting a kinetic expression can confirm a mechanism but not prove a mechanism, i.e. a validation of a hypothesis via kinetics is not without problems and may be open to dispute on its interpretation.

The product distribution in the Fischer-Tropsch synthesis is also affected by the addition of manganese to a cobalt-based catalyst (Dinse *et al.,* 2012; Johnson *et al.,* 2015; Morales *et al.,* 2005). A strong shift in the product distribution to higher molecular weight products was observed for unpromoted cobalt catalysts upon increasing manganese content. This was attributed to olefin re-adsorption, which can lead to secondary olefin hydrogenation or to olefin re-incorporation into the chain growth scheme (Dinse *et al.,* 2012). The latter is expected to be favoured upon a reduction in coverage of catalyst surface by hydrogen atoms relative to CO (Dinse *et al.,* 2012). A plausible explanation for this is the intimate interaction of MnO_x with Co active sites which leads to Mn^{2+} acting as a Lewis acid that enhances the adsorption and dissociation of CO (Johnson *et al.,* 2015).

Characterisation of surface manganese

Cobalt and manganese are typically in intimate contact as observed, via element mapping that there is an intimate interaction between Co and Mn (Morales *et al.,* 2005; Johnson *et al.,* 2015; Johnson & Bell, 2016). Morales *et al.* (2005) observed the migration of MnO particles towards the TiO_2 during H_2 reduction which was attributed to strong metal-support interactions. However, MnO_x islands were frequently seen in proximity to the cobalt particles (Morales *et al.,* 2005). Moreover, manganese is found to have a high affinity for oxygen hence it exists in its oxidic form before and after reduction (Morales *et al.,* 2005; Johnson *et al.,* 2015; Johnson & Bell, 2016).

Effect of manganese on cobalt particle size

The effect of manganese on particle size of cobalt seems to be unclear. Johnson *et al.* (2015) and Johnson & Bell, (2016) observed an insignificant change in the size of Co particles, which nullifies the effect of particle size towards activity and selectivity of the catalysts. The particle size of cobalt for all manganese loadings was close to 10 nm, a point when the turnover frequency for the Fischer-Tropsch synthesis over cobalt becomes insensitive to the particle size (Bezemer *et al.,* 2006). However, Dinse *et al*. (2012) observed a decrease in particle size, whilst Feltes *et al.* (2010) observed an increase in the Co particle size, which is contradicting and may need further investigation.

Manganese as an electronic promoter

Manganese has also been reported to have an electronic promoting effect for cobalt-based Fischer-Tropsch catalysts. The surface properties of Mn-Co/SiO_2 catalysts were investigated via infrared spectroscopy in combination with CO probe molecules (Morales *et al.,* 2007; Johnson *et al.,* 2015; Johnson & Bell, 2016). CO as probe

molecules accept electrons from the metal surface sites, forming metal-carbonyl complexes (Morales *et al.,* 2007). These complexes can be characterised using infrared spectroscopy with the changes in the vibrational energy explained by the molecular orbital theory (Morales *et al.,* 2007). The 5σ orbital of the CO molecule forms a σ bond with the vacant metal orbital. For electron rich surfaces, there is back-donation of electrons from the metal d-orbital into the π^* antibonding orbital of the CO molecule (Bezemer *et al.,* 2006; Morales *et al.,* 2007; Dinse *et al.,* 2012; Johnson *et al.,* 2015).

The addition of manganese, which in its ionic form may act as a Lewis acid (Dinse *et al.,* 2012; Morales *et al.,* 2005; Morales *et al.,* 2007; Johnson *et al.,* 2015; Johnson & Bell, 2016), results in the withdrawal of electron density from the Co surface active sites, thus decreasing the number of electrons back-donated from the metal d-orbital into the π^* antibonding orbital of the CO molecule (Bezemer *et al.,* 2006; Morales *et al.,* 2007; Dinse *et al.,* 2012; Johnson *et al.,* 2015). Consequently, the C-O bond gains strength, causing a greater amount of linearly adsorbed CO molecules (Morales *et al.,* 2007). This was qualitatively consistent with decreased hydrogenation rate, resulting in low methane selectivity and high C_{5+} selectivity (Dinse *et al.,* 2012; Morales *et al.,* 2005; Morales *et al.,* 2007; Johnson *et al.,* 2015; Johnson & Bell, 2016).

Manganese improving CO dissociation and adsorption

It has been argued, via reaction kinetics, that manganese increases the strength of CO adsorption and enhances CO dissociation (Dinse *et al.,* 2012; Johnson *et al.,* 2015; Johnson & Bell, 2016). A rate law was derived mathematically, assuming CO dissociation to be the rate limiting step (Dinse *et al.,* 2012; Johnson *et al.,* 2015).

$$-r_{CO} = \frac{abP_{CO}P_{H2}}{(1 + bP_{CO})^2} \tag{2.3}$$

a is the apparent rate constant and b is the CO adsorption constant. The two parameters increased with an increase in the manganese loading (Dinse *et al.,* 2012; Johnson *et al.,* 2015; Johnson & Bell, 2016). It was then concluded that there is an increased strength of CO and increased rate of CO dissociation on cobalt-based catalysts. It has been speculated that manganese enhances the strength of CO

adsorption and CO dissociation via reaction kinetics. As mentioned above, reaction kinetics may only confirm a mechanism but cannot prove a mechanism and validation via reaction kinetics may not be suitable.

Johnson *et al.* (2015) used temperature programmed desorption (TPD) of carbon monoxide to show enhancement of the strength of adsorption of CO. The temperature programmed desorption of CO technique may also give information on dissociation of adsorbed CO (Wang *et al.,* 2005). Passivated Mn/Co/SiO_2 catalysts were reduced at 400 °C for 2 hrs in H_2 with a heating rate of 4 °C/min. Subsequently, the temperature was cooled to -60 °C and CO pulses were introduced to the catalysts using He as a carrier. This was done till no further uptake was observed. The samples were then flushed in He for 10 mins and the temperature was raised to 800 °C at 10 °C /min to desorb chemisorbed CO from the catalyst surface. CO-TPD profiles obtained by Johnson *et al.* (2015) each had 3 peaks, 2 low temperature peaks and one high temperature peak. The first low temperature peak was attributed to physisorbed CO. This may not be true. The critical point of CO is -140 °C and CO pulses were introduced at -60 °C, a temperature above the critical point, which makes it difficult for physisorption to occur. Physisorption is analogous to condensation and thus cannot occur at temperatures above critical point (Zhou, 2005). The second low temperature peak was attributed to chemisorbed CO. The third high temperature peak was assumed to be due to the adsorbed CO in contact with MnO promoter. An increased rate of CO dissociation was seen with an increase in high temperature peak to low temperature peak ratio (Johnson *et al.,* 2015). These calculations were based on the assumption that the higher temperature peak is as a result of adsorption of CO which is in close contact with MnO promoter, which then facilitates CO dissociation via the Lewis acid interactions.

An increase in CO desorption activation energy due to the shift of the first chemisorbed peak to higher temperatures was observed as a result of manganese promotion. The changes in desorption temperatures appeared to be relatively small (peaks shifted by 5 °C for samples with a low amount of manganese (Mn:Co=0.01) promotion and by 20 °C for samples with a higher manganese loading (Mn:Co=0.5)) to validate the enhancement of CO adsorption strength on manganese promoted catalysts. From the CO-TPD experiments, it was concluded that manganese increases the strength of CO adsorption and enhances CO dissociation (Johnson *et al.,* 2015).

Effect of Mn:Co molar ratio on cobalt-based Fischer-Tropsch catalysts

The amount of manganese added to the cobalt-based Fischer-Tropsch catalyst appears to play an imperative role in the catalytic performance. The addition of a small

amount of manganese (Mn:Co < 0.15 w/w) has been reported (Dinse *et al.,* 2012; Johnson *et al.,* 2015; Thiessen *et al.,* 2012) to improve the rate of the Fischer-Tropsch synthesis for cobalt-based catalyst, whilst higher manganese loadings had the opposite effect. This ascribed to the blockage of Co active sites. Dinse *et al.* 2012 reported a strong decrease upon promotion of 12 wt.% Co/SiO_2 (prepared via incipient impregnation) with small amounts of manganese (Mn/Co=0.05 w/w). This was accompanied by an increase in C_{5+} selectivity and an increase in the olefin/paraffin ratio. However, beyond Mn/Co=0.05 w/w, no change was observed. Thissen *et al.* 2012 reported on the manganese promotion of 9.6 wt.% Co/CNT (prepared via wet impregnation) in as low as a Mn/Co ratio of 0.01 w/w, which led to a 50 % decrease in methane selectivity and more than 100 % increase in C_{5+} selectivity. Johnson *et al.* 2015 reported an optimal loading of Mn/Co = 0.1 w/w at higher pressures. The optimal amount Mn/Co to obtain optimum catalyst performance is not clear based on the data collected in literature. One may argue that this depends on the materials and procedures used for catalyst preparation, which influences the interaction of cobalt and manganese on the support (Johnson *et al.,* 2015). Therefore the interaction of Co and manganese may vary with different materials and catalyst preparation methods.

Effect of manganese on cobalt reducibility

Studies have shown that the hydrogen uptake by the cobalt-based Fischer-Tropsch catalysts decreases with an increase in the manganese loading (Dinse *et al.,* 2012; Morales *et al.,* 2005; Morales *et al.,* 2007; Johnson *et al.,* 2015; Johnson & Bell, 2016). This may be due to blockage of Co surface by manganese species (Dinse *et al.,* 2012; Feltes *et al.,* 2010; Johnson *et al.,* 2015).

It was found that manganese decreases the extent of Co_3O_4 reduction (Dinse *et al.,* 2012; Morales *et al.,* 2005; Morales *et al.,* 2007; Johnson *et al.,* 2015; Johnson & Bell, 2016). This is assumed to be due to the formation of Co-Mn mixed spinel structure (Dinse *et al.,* 2012; Morales *et al.,* 2005; Morales *et al.,* 2007; Johnson *et al.,* 2015; Johnson & Bell, 2016).

Feltes *et al*. (2010) examined the potential of strong electrostatic adsorption preparation method for the synthesis of $Mn/Co/TiO_2$ at pH = 1 using potassium permanganate as a manganese precursor. This method resulted in enhanced activity of $Mn/Co/TiO_2$ due to enhancement of cobalt reducibility, thus it was deemed a vialable preparation method that produces an effective promoted catalyst with intimate promoter-metal interactions which cannot be accomplished by the current industrial methods of preparation (e.g sequential impregnation and co-precipitation). However there has not been an attempt to compare the catalytic performances of manganese promoted cobalt-based catalysts prepared using strong electrostatic adsorption and

the current industrial methods of preparation. Zhao *et al.* (2011) used the temperature programmed reduction and Z-contrast imaging coupled with electron energy-loss spectrum imaging to study the elemental distribution and morphology of calcined and reduced manganese promoted cobalt catalysts prepared using strong electrostatic method (use of $KMnO_4$ solution at pH = 1) and dry impregnation method (use of manganese(II) acetate tetrahydrate as precursor with no pH adjustment). It was found that with dry impregnation, large particles of manganese formed on both silica and cobalt surface whereas with strong electrostatic adsorption, the manganese covers the cobalt particle surface. With these differences in elemental distribution of manganese, it would be interesting to know how each of the catalyst performs in the Fischer-Tropsch synthesis.

Most of these current industrial methods make use of manganese(II) acetate tetrahydrate or manganese(II) nitrate tetrahydrate as a source of manganese. Previous studies have explored the impregnation of manganese(II) acetate tetrahydrate and manganese(II) nitrate tetrahydrate on cobalt-based Fischer-Tropsch catalysts (Johnson *et al.,* 2015; Morales *et al.,* 2007; Morales *et al.,* 2006; Dinse *et al.,* 2012; Bezemer *et al.,* 2006).

Despite the abundant work on the effect of manganese in cobalt-based Fischer-Tropsch, the manner in which manganese affects the activity and selectivity of cobalt-based catalysts is not fully understood.

2.6 Aim of the study

This study aims to investigate the effect of manganese (achieved by selectively adsorbing $[MnO_4]^-$ anion from a potassium permanganate solution of pH = 1) on activity and selectivity of Co/SiO_2, paying attention to the role it plays in CO adsorption. Additionally, impregnation of manganese(II) acetate tetrahydrate (with no pH adjustments) on pre-formed Co/SiO_2 was investigated. This was done to compare the catalytic performances of the two batches of catalysts prepared using two different manganese precursors, with the assumption that potassium in the potassium permanganate precursor might play a role in the catalytic activity.

2.6.1 Hypothesis

Manganese enhances CO adsorption and dissociation on cobalt-based Fischer-Tropsch catalysts which results in an increase in the turnover frequency of cobalt-based Fischer-Tropsch catalysts, whilst at the same time limiting methane selectivity. This is due to Mn^{2+} acting as an electron promoter for the catalytically active metallic cobalt surface.

2.6.2 Key Questions

- Does the inclusion of manganese increase the strength of CO adsorption on cobalt-based catalysts?
- Does the inclusion of manganese enhance CO dissociation on cobalt-based catalysts?
- Does manganese enhance activity and selectivity of cobalt-based catalysts? If yes, can it be ascribed to enhanced CO adsorption and dissociation?
- Does potassium in potassium permanganate precursor get adsorbed onto pre-formed Co/SiO_2 catalysts at pH = 1? If that is the case, does it play a role in enhancing the activity of $Mn\text{-}Co/SiO_2$?

3 EXPERIMENTAL PROCEDURE

3.1 Discussion of method and programme

An unmodified Co_3O_4/SiO_2 catalyst precursor was prepared via a two-step wet impregnation (IMPR) technique, followed by calcination at high temperatures. A strong electrostatic adsorption (SEA) of potassium permanganate precursor from a solution adjusted to pH = 1 was used to adsorb different manganese concentrations to Co_3O_4/SiO_2 using the method described by Feltes *et al.* (2010). The prepared catalysts were characterised using ICP OES, XRD, TEM, STEM EDS element mapping, TGA, H_2-TPR and CO-TPD techniques. A second batch of Co_3O_4/SiO_2 catalyst precursor, where different concentrations of manganese were added by IMPR of manganese(II) acetate tetrahydrate ($Mn(CH_3COO)_2.4H_2O$) with no pH adjustments, was synthesized. The two batches were tested in a fixed bed reactor under the following Fischer-Tropsch conditions: 220 °C at a constant pressure of 20 barg and H_2/CO molar feed ratio of 2:1. Under these conditions, CO-conversion and hydrocarbon product selectivity data were analysed using a gas chromatography (GC) technique.

3.2 Catalyst preparation

Co/SiO_2 catalyst precursors were prepared using a wet impregnation (IMPR) approach reported by Espinoza *et al.* (1998), with a target metal loading of 22 wt.%. In a typical wet impregnation procedure: 10 g of cobalt(II) nitrate hexahydrate ($Co(NO_3)_2.6H_2O$, Sigma Aldrich) dissolved in 30 ml of deionised water, was dispersed on 12.5 g of silica (Davisil 646, 36-60 mesh, pore diameter = 150 Å, surface area = 300 m^2/g). The slurry was then treated for 2.5 hrs at 75 °C in a rotary evaporator with a rotating speed of 75 rpm and a pressure of 72 mbar to remove the excess solvent and dry the impregnated carrier. The dried, impregnated carrier was calcined at 230 °C under a continuous flow of air (38 ml (NTP)/min) for 2 hrs with a ramping rate of 2 °C/min in a fluidised bed (bed height = 4 cm). The resultant calcined sample was re-slurried in a solution prepared by dissolving 8.75 g $Co(NO_3)_2.6H_2O$ in 30 ml of deionised water. The new slurry was treated in a rota evaporator again for 2.5 hrs at 75 °C and 72 mbar until free flowing in a rota evaporator. The new dried impregnated carrier was calcined in a fluidised bed at 230 °C in flowing air (38 ml (NTP)/min) for 2 hrs (Espinoza *et al.*, 1998). The final product of Co_3O_4/SiO_2 catalyst (~18 g) was divided into 5 equal batches prior to doping with different manganese concentrations.

Different manganese loadings were adsorbed onto the sub batches using either strong electrostatic adsorption (SEA) or impregnation (IMPR) approach. Manganese was adsorbed on Co_3O_4/SiO_2 using SEA of potassium permanganate solution (Feltes *et al.,* 2010). Different amounts of potassium permanganate were dissolved in 50 ml of deionised water, giving different concentrations of manganese: 290 mg/L(5 mmol/L),

330 mg/L (6mmol/L), 952 mg/L (17 mmol/L), and 1897 mg/L (35 mmol/L). The pH of the solutions was adjusted to 1 by adding concentrated nitric acid (0.1 M HNO_3) (Zhao *et al.,* 2011). The choice of the pH was dictated by the zeta potential of silica gel and Co_3O_4 (de Beer *et al.*,2014). Samples (~3.6 g each) were placed in a 50 ml potassium permanganate solution and the pH was carefully monitored for 1 hr. The samples were then washed 3 times in a vacuum filtration unit using distilled water. After washing, the samples were put on a watch glass, dried at 60 °C in an oven overnight and calcined in a fluidised bed (bed height = 4 cm) at 230 °C in flowing air (38 ml (NTP)/min) for 2 hrs (ramping rate of 2 °C/min).

A second batch of Co_3O_4/SiO_2 was prepared according to the method described above. Manganese was added by impregnating (IMPR) $Mn(CH_3COO)_2.4H_2O$ on the pre-formed Co_3O_4/SiO_2 catalyst, with no pH adjustments. Different manganese concentrations of 45.4 mg/L (0.83 mmol/L) and 142 mg/L (2.6 mmol/L) were prepared by dissolving $Mn(CH_3COO)_2.4H_2O$ in 50 ml of deionised water. Co_3O_4/SiO_2 (~3.6 g) was added to 50 ml of the as-prepared manganese acetate solution and then treated for 2.5 hrs at 75 °C in a rotary evaporator with a rotating speed of 75 rpm and a pressure of 72 mbar to remove the excess solvent and dry the impregnated carrier. The dried, impregnated carrier was calcined at 230 °C in flowing air (38 ml (NTP)/min) for 2 hrs with a ramping rate of 2 °C/min in a fluidised bed (bed height = 4 cm).

3.3 Catalyst characterisation

Catalyst characterisation plays a big role in determining the physical and chemical characteristics of a synthesized catalyst. The following sections cover a few catalyst characterisation techniques used.

3.3.1 Induced Coupled-Plasma- Optical Emission Spectroscopy (ICP-OES)

Elemental analysis of the Mn^{SEA}-Co_3O_4/SiO_2 and Mn^{IMPR}-Co/SiO_2 catalysts was carried out using ICP-OES, a versatile technique used to determine concentrations of elements (Sneddon & Vincent, 2008). Each sample (ca. 100 mg) was digested in a mixture of aqua regia and hydrofluoric acid (HF) using a Mars 6 Microwave digester (see Table 3.1). The sample was subsequently neutralized using boric acid (H_3BO_3). The digested sample was transferred into a volumetric flask and diluted to 50 ml using deionised water. Prior to elemental analysis of cobalt, manganese and potassium, the sample was filtered using a 0.2 μm filter. The amount of manganese, potassium and cobalt was analysed in Mn-Co_3O_4/SiO_2 catalyst.

ICP-OES, calibrated using a multi-elemental standard calibration solution containing vanadium, chromium, cobalt, manganese, iron, aluminium, copper, zinc, silver,

potassium and cadmium, was used to perform the calibration of a Varian 730 ES ICP-Optical Emission Spectrophotometer with concentrations 0.2, 0.5, 1, 2, 5 and 10 ppm. The emission lines chosen for each element were based on high intensity signal and no spectral interferences.

Table 3.1: Microwave digester conditions.

	Acids	Ramp time (min)	Hold time (min)	Final temperature (°C)
Digestion	9 ml Aqua Regia and 1 ml HF	30	30	220
Neutralisation	10 ml H_3BO_3	30	10	170

3.3.2 Powder X-Ray Diffraction (PXRD)

Powder X-ray diffraction (PXRD) is a common technique for characterising crystal structures. It gives information on the structural parameters such as crystalline domain size, crystallinity and the phases present in the material (Bunaciu *et al.,* 2015). The technique is based on constructive interference of X-rays in the crystal sample. A cathode ray tube (with a filter) generates the X-rays and gets directed to the sample. The constructive interference is produced only when the conditions of Bragg's law are satisfied (Bunaciu *et al.,* 2015):

$$n \cdot \lambda = 2d \cdot \sin\theta \qquad (3.1)$$

n is an integer, λ is the wavelength of the X-ray, d is the lattice spacing generating the diffraction and θ is the angle of diffraction (Bunaciu *et al.,* 2015). Scanning a sample through a range of 2θ values yields a diffraction pattern determined by the lattice structure (Bunaciu *et al.,* 2015). The conversion of the diffraction peaks to the d-spacing of lattice structure allows identification of the sample because each sample has a unique d-spacing with standard reference pattern (Bunaciu *et al.,* 2015).

PXRD measurements were carried out on a D8 Advance Bruker laboratory instrument with a cobalt source (λ=1.78897 **Å**), operating at 35 kV and 40 mA. The calcined Mn-Co_3O_4/SiO_2 catalyst precursors were spread flat onto a sample holder using a microscope slide. They were then carefully put into the X-ray diffractometer for characterization. The specimens were scanned at 2θ = 5 °-120 ° with a step size of 0.043 °/step and a scan time of 0.1 s/step. The international centre for diffraction data PDF-2 database was used to identify the phases in the x-ray diffractograms. The average crystallite size of Co_3O_4 in the catalyst precursor was determined by applying the Debye-Scherrer equation on the most intense diffraction line, viz. Co_3O_4(311):

$$\tau = K\frac{\lambda}{\beta\cos\theta} \quad (3.2)$$

where τ is the crystallite domain size in Å, K is a shape factor typically assumed to be 0.9, λ is the radiation wavelength in Å, β is the width of the peak (taken as full width at half maximum height, FWHM) and θ is the Bragg angle in either degrees or radians (Bunaciu *et al.,* 2015).

3.3.3 Transmission electron microscopy (TEM)

Transmission electron microscopy (TEM) is one of the powerful techniques used to image the materials at nanoscale. From the acquired TEM micrographs: the particle sizes, shapes and particle size distributions of the materials can be determined. Prior to TEM characterization, the calcined Mn-Co_3O_4/SiO_2 samples were ground using a micronizer, followed by suspending the fine powder in approximately 2 ml of ethanol and the resultant mixture was ultrasonicated for 3 mins. Specimens for TEM characterization were prepared by one-drop casting of the suspended samples onto carbon-coated copper grids. The prepared TEM specimens were allowed to dry under ambient conditions. A FEI Tecnai F20 field emission cryo-TEM, operating at 200 kV, was used for imaging.

3.3.4 Scanning transmission electron microscopy coupled energy dispersive X-ray spectroscopy (STEM EDS)

The elemental distributions of Mn-Co_3O_4 on SiO_2 support material were analysed using high-angle annular dark field scanning transition electron microscopy (HAADF-STEM) coupled with energy dispersive X-ray spectroscopy (EDS), on a FEI Nova NanoSEM 230, operating at 20 keV. The sample preparation method for STEM-EDS analyses is similar to the one described in section 3.3.3, for TEM imaging.

3.3.5 Hydrogen-temperature programmed reduction (H_2-TPR)

Cobalt is active in its metallic form as a catalyst for the Fischer-Tropsch synthesis (Iglesia, 1992). Hence, the calcined catalyst precursor must be reduced to transform it into its active state. The reduction process can be performed in H_2, CO or synthesis gas (Jalama *et al.,* 2012), but reduction in a H_2 atmosphere is preferred (Dry, 2002).

The reduction of Co_3O_4 in H_2 is thought to take place in two steps: (1) the reduction of Co_3O_4 to CoO and (2) the reduction of CoO to metallic cobalt (Castner *et al.,* 1990; Dry, 2002; Ernst *et al.,* 1998). The following equations describe these two-step reduction processes:

$$Co_3O_4 + H_2 \rightarrow 3CoO + H_2O \quad (3.3)$$

$$3CoO + 3H_2 \rightarrow 3Co + 3H_2O \quad (3.4)$$

Temperature programmed reduction (TPR) experiments were conducted on a Micrometrics Autochem HP 2950. Approximately 37 mg of the calcined Mn-Co_3O_4/SiO_2 sample was sandwiched between a small amount of quartz wool in a quartz U-tube reactor. The samples were dried at 120 °C in a flow of Ar (10 ml (NTP)/min) for 60 mins. The samples were then allowed to cool down to 60 °C and linearly raised to 920 °C (ramp rate 10 °C /min) whilst flowing 5% H_2/Ar (50 ml (NTP)/min) over the sample. The sample gas was diverted to a cold trap containing iso-propanol/liquid nitrogen mixture at ~0° C to condense any volatiles/water before being sent to the detector. The concentration of H_2 was recorded as a TCD signal as a function of temperature.

3.3.6 Thermogravimetric analysis (TGA)

To determine the degree of reduction of Co_3O_4 in Mn-Co_3O_4/SiO_2 catalysts, mass loss was measured during the reduction in a Mettler-Toledo TGA/SDTA851^o. The mass of the alumina crucibles (the reference and the sample crucibles) was determined and approximately 13 mg of each sample was loaded into a crucible. The samples were heated in N_2 flow of 95 ml (NTP)/min from room temperature to an equilibration temperature of 50 °C. The samples were further heated up in a mixture of 5% H_2/N_2 (100 ml (NTP)/min) to 350 °C, with a ramp rate of 10 °C/min. The samples were reduced at 350 °C for 4 hrs. The degree of reduction was calculated according to equation 3.4 below, in which it was assumed that oxygen (O) was lost from Co_3O_4 during reduction. Therefore, the degree of reduction is directly linked to the mass loss through the oxygen removal, assuming the reduction process takes a direct $Co_3O_4 \rightarrow Co^o$ route.

$$DoR = \frac{m_{Co^0}}{m_{Co,total}} \cdot 100\% = \frac{\frac{\Delta m}{16} \cdot \left(58.9332 + \frac{4}{3} \cdot 16\right)}{m_{Co,total}} \cdot 100\% = \frac{\Delta m}{m_{Co,total}} \cdot 501.7\% \quad (3.5)$$

3.3.7 Metal surface area - H_2 chemisorption

The metal cobalt surface area was determined from the H_2 uptake on the reduced catalyst. Approximately 0.1 g of each sample was loaded in a quartz U-tube. The samples were degassed for 3 hrs at 200 °C (ramp rate = 5 °C/min) under a He flow (50 ml (NTP)/min). The samples were subsequently cooled to 60 °C, before ramping the temperature linearly to 350 °C (ramp rate 10 °C/min) whilst flowing pure H_2 (50 ml (NTP)/min) over the samples. Subsequently, the samples were kept at 350 °C under a continuous flow of pure H_2 (50 ml (NTP)/min) for 4 hrs. Thereafter, the system was flushed with He and evacuated. The H_2 adsorption isotherms were measured at 125 °C and collected in the pressure range of 0-600 mmHg. The H_2 chemisorption data, i.e quantity of H_2 adsorbed with respect to partial pressure was fitted into a Langmuir adsorption isotherm model given by equation 3.6 below.

$$\theta_H = \frac{V_{H_{2,uptake}}}{V_{H_2\,monolayer}} = \frac{\left(K.P_{H_2}\right)^{\frac{1}{2}}}{1+\left(K.P_{H_2}\right)^{\frac{1}{2}}} \tag{3.6}$$

θ_H is the fractional coverage of H on an adsorption site, K is the equilibrium adsorption constant and P_{H_2} is the partial pressure of H_2. Due to the slow increase of H_2 uptake with pressure, a new equilibrium constant was introduced, thus the H_2 uptake was measured using the following equation:

$$V_{H_{2,uptake}} = V_{H_2\,monolayer}.\frac{\left(K_1.P_{H_2}\right)^{\frac{1}{2}}}{1+\left(K_1.P_{H_2}\right)^{\frac{1}{2}}} + K_2.P_{H_2} \tag{3.7}$$

The parameters K_1, K_2 and $V_{H_2\,monolayer}$ were obtained using linear regression and Table 3.2 shows the data obtained for these parameters:

Table 3.2: The amount of H_2 adsorbed to form a monolayer and equilibrium constants obtained from modelling H_2 adsorption Langmuir isotherm via linear regression.

[Mn], mmol/L	**0**	**5**	**6**	**17**	**35**
$V_{H_2\,monolayer}$, **cm³/g**	2.92	2.84	2.63	2.41	2.46
K_1	0.37	0.51	0.46	0.53	0.46
K_2 **x 10⁻⁴**	7	8	4	5	4

Using the amount of H_2 adsorbed to for a monolayer, active metal surface area, dispersion and mean particle size were determined as follows:

Metal surface area

$$Co\ metal\ surface\ area = \left(\frac{6.023 \times 10^{23} atoms \times V_{H_2-monolayer} \left(\frac{cm^3}{g}\right) \times SF}{\frac{14.6 atoms}{nm^2}\ (number\ of\ Co\ atoms\ per\ nm^2} \right) . Co\ wt.\% \quad (3.8)$$

SF is the stoichiometric factor of H_2/Co (2).

Cobalt dispersion

$$Co - dispersion = \frac{\frac{V_{H_{2-uptake}}}{22.413 \cdot cm^3(STP)} \times SF}{\frac{w_{Co}\left(\frac{mg}{g}\right)}{58.9332 \cdot \frac{mmol}{mg}}} \quad (3.9)$$

with w_{Co} the cobalt loading in the catalyst in mg/g and the cobalt dispersion corrected for the degree of reduction:

$$corrected\ Co - dispersion = \frac{Co - dispersion}{DoR} \quad (3.10)$$

Average particle size

$$d_{Cp} = \frac{96}{corrected\ Co - dispersion} \quad (3.11)$$

3.3.8 Temperature programmed desorption of CO (CO-TPD)

Temperature programmed desorption (TPD) of carbon monoxide (CO) was conducted on a Micrometric Autochem 2920. Approximately 150 mg of each sample was loaded in a quartz U-tube reactor sandwiched between glass wool with temperature measured at the top of the sample. The samples were dried for 1 hr under a continuous flow of Ar (10 ml (NTP)/min). The samples were subsequently cooled down to 40 °C and reduced at 350 °C for 4 hrs (ramp rate of 10 °C/min) in flowing H_2 (20 ml (NTP)/min). Post reduction, the temperature was cooled down to 40 °C in 50 ml (NTP)/min of helium. A sample loop was filled by constantly flowing CO (20 ml (NTP)/min) through. A maximum of 80 doses of CO were pulsed into the carrier gas, He (50 ml (NTP)/min).

Dosing was stopped when the surface was saturated as determined from a thermal conductivity detector (TCD) response produced by the successive injections of equal volumes of CO on the sample. During the first few injections, CO may be taken up completely by the sample, hence no change in signal is recorded by the detector. As the sample reaches saturation, peaks representing the amount of unreacted CO appear. When the surface is saturated, each of the injected gas volumes emerges from the sample tube unchanged and the detected peak areas are constant. Thereafter, excess CO was removed from the catalyst bed by flowing initially 50 ml (NTP)/min of He for 30 mins at 40 °C. The temperature was subsequently raised linearly to 900 °C (with a ramp rate of 10 °C/min) whilst flowing He (20 ml (NTP)/min) over the sample. The CO concentration in the effluent was measured using the TCD.

3.4 Catalytic testing

The Fischer-Tropsch synthesis was carried in a laboratory test unit schematically shown in Figure 3.1. The flow of N_2, H_2 and CO are controlled by 3 mass flow controllers. N_2 was added to serve as an internal standard in the analysis of the effluent using GC-TCD. Ar was added pressure-controlled, and its flow was dictated by opening the flow controlling needle valve in the effluent line. This allows a constant pressure operation for the reaction with contractions.

To ensure homogeneity, prior to being fed into the reactor, the reactants were mixed (H_2 and CO). The mixture was fed to the reactor via a four-way valve, which allows the feed to flow directly into the reactor or bypass the reactor. The Fischer-Tropsch synthesis occurred in the isothermal zone region (see Appendix A). The temperature in the various zones was controlled using LabVIEW.

The liquid Fischer-Tropsch products (wax) were trapped in the hot trap operating at 200 °C. The more volatile Fischer-Tropsch products remained in the vapour phase and subsequently the effluent was mixed with the pressure-controlled added Ar. The stream passed the flow controlling needle valve and mixed with N_2, which was added to act as an internal standard for analysis. After expansion, the gaseous reactor effluent went through a cold trap. The cold trap is always at room temperature to condense out water before being sent to the online GC-TCD for analysis.

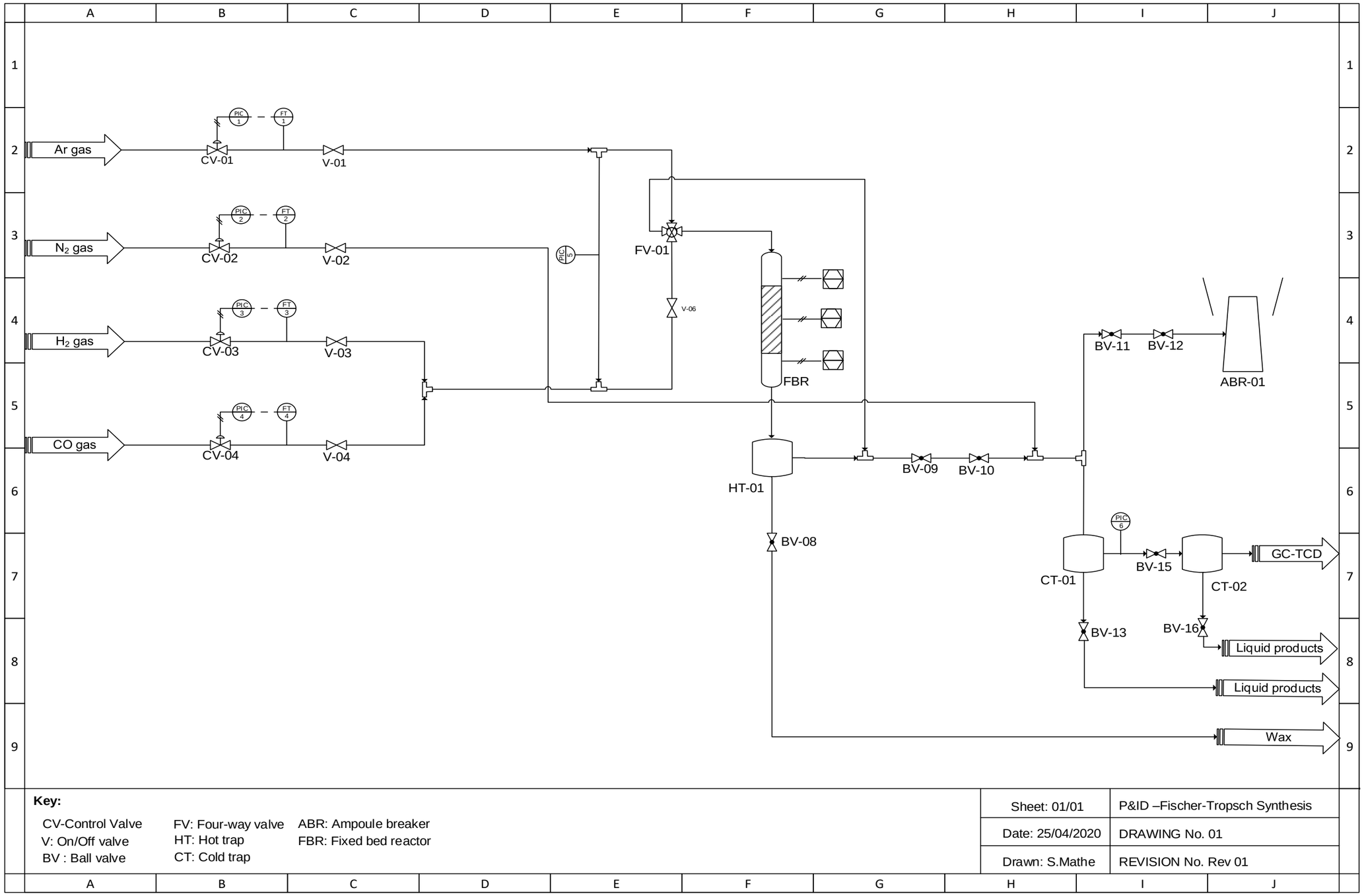

Figure 3.1: Process instrumentation diagram (PID) of the laboratory test unit.

The organic product content of the effluent was determined using an off-line GC-FID. The effluent was sampled using the so-called ampoule technique (Schulz *et al*., 1984), which makes use of pre-evacuated glass ampoules (volume of approximately 2 ml). The long capillary end of the ampoule was pushed through a sealing rubber into the sampling chamber filled with the product stream. By breaking the capillary tip using a fork, the ampoule was filled with gaseous products. After a few seconds, the ampoule was pulled out a bit and sealed using a flame from a gas burner. This ensured that the captured gas is contained in the ampoule. Figure 3.2 shows a cross section of an ampoule sampler sketched by Schulz *et al*. (1984).

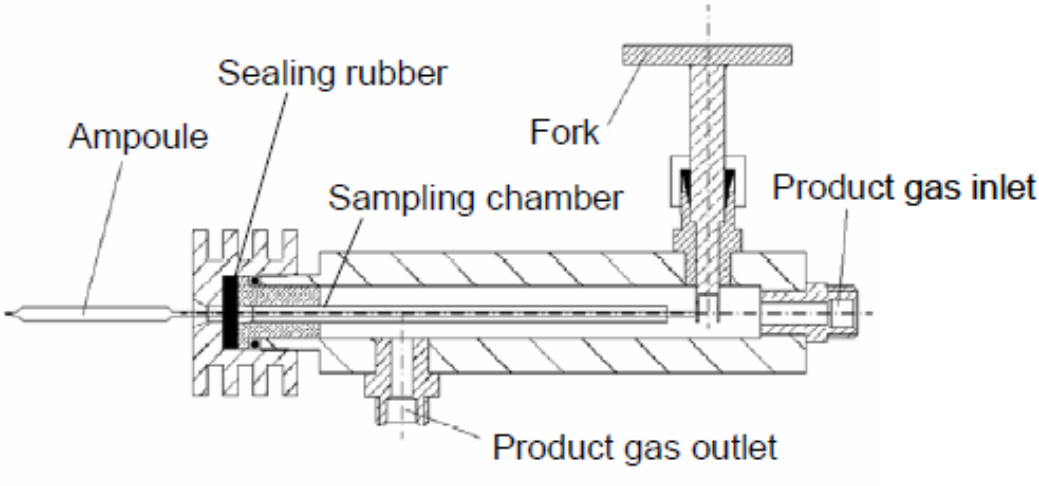

Figure 3.2: Cross sectional view of an ampoule sampler extracted from Schulz *et al.* (1984).

Reactor loading

Fixed bed reactors are frequently used for many catalytic reactions, but inadequate removal of the reaction heat in highly exothermic reactions can lead to bad performance of catalysts or fast deactivation (Bianchi *et al.,* 2006). The use of diluent increases the heat transfer area and thus may result in a flatter temperature profile in the reactor. The reactor tube (OD = 0.5 inch, L = 300 mm), made of stainless steel, was packed as shown in Figure 3.3. The bottom of the reactor was packed with silicon carbide (SiC). The calcined catalyst precursor (0.5 g) diluted with ~1.5 g of SiC (particle size = 300 µm) was packed in a fixed bed reactor in the annular space given by the thermowell (OD = 0.25 inch, stainless steel). The annular space above the catalyst bed was filled with SiC which served as a mixing and pre-heating zone for the reactants.

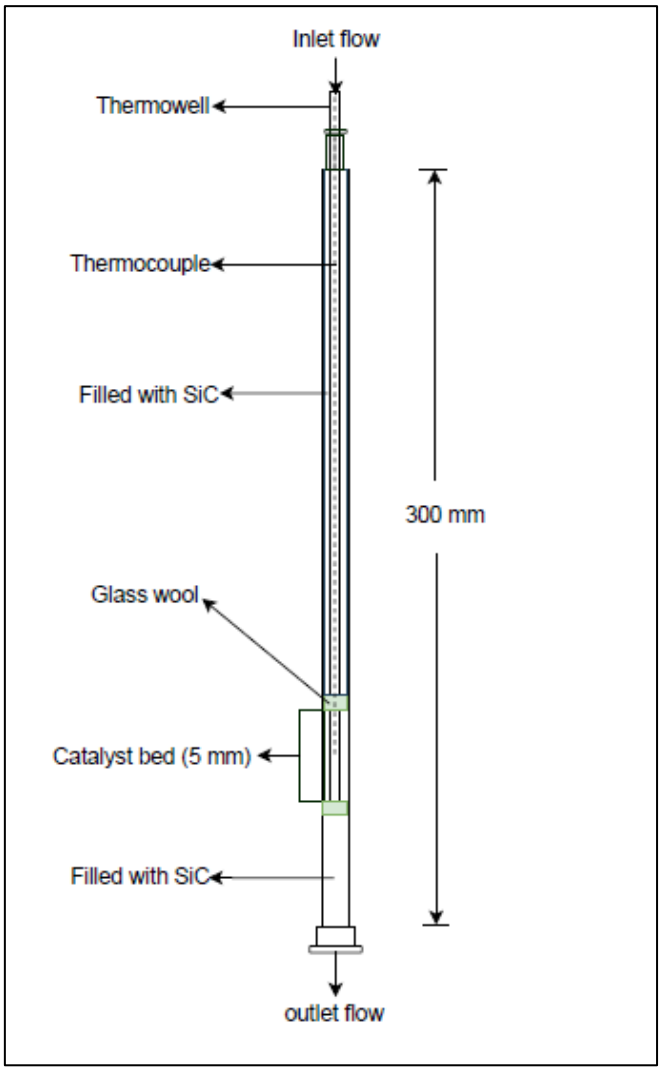

Figure 3.3: Schematic diagram of how the fixed bed reactor was packed (not drawn to scale).

3.4.1 Catalyst reduction

The reactor was depressurized to 1 barg in preparation of the reduction process. The calcined catalyst precursors were then reduced at 350 °C for 4 hrs in 130 ml (NTP)/min H_2 flow with a ramp rate of 10 °C/min.

3.4.2 Start-up of the Fischer-Tropsch synthesis

After the reduction process, the reactor was cooled down to 200 °C and flushed with Ar. The reactor was subsequently pressurized to 20 barg. High-pressure Ar was added pressure-controlled to maintain the reactor pressure. The flow controlling needle valve was adjusted in a way that it allows an outlet flowrate equal to total flowrate of syngas plus ~20 ml (NTP)/min of Ar. The syngas flow of 300 ml (NTP)/min (H_2/CO=2) whilst the reactor is on bypass mode. N_2 flow, which serves as an internal standard in the analysis of the effluent, was set to 10 % of the total flowrate of syngas. The total syngas

flowrate was then directed to the GC-TCD for analysis to determine the feed composition. Thereafter, the total syngas flow was directed to the reactor. Subsequently, the reactor was heated up to 220 °C at a ramp rate of 0.8 °C/min to avoid temperature runaways caused by the highly exothermic Fischer-Tropsch reaction. As soon as it reached the reactor temperature, the reactor effluent was directed to the GC-TCD for product analysis. The reaction was performed for a total reaction time of 48 hrs. The Fischer-Tropsch reaction conditions are listed in Table 3.3.

Table 3.3: Fischer-Tropsch synthesis conditions.

Catalyst weight (g)	0.5
Temperature (°C)	220
Pressure (barg)	20
H_2/CO ratio	2

Since the FT synthesis is aimed to operate at high conversion, the space velocity was slowly decreased to achieve a high conversion of CO. High conversion was obtained with a syngas flow rate of 60 ml (NTP)/min.

3.4.3 Product Analysis

The permanent gases in the effluent of the reactor were separated and analysed using an online GC-TCD. Samples of the effluent were collected in previously evacuated ampoules and analysed for the organic compound products.

Online GC-TCD Analysis

The permanent gases such as H_2, CO, CO_2 and CH_4 were analysed using a Agilent 7820A GC system equipped with a thermal conductivity detector (TCD). The mixture was separated with a 80/100 Porapak Q column of 1.83 m length and 2 mm inner diameter, as well as a 60/80 MolSeive 5A column of 1.83 m length and 2 mm inner diameter. Ar was used as a carrier gas, and sampling after every 14 mins was done using a 6-way valve. Table 3.4 shows the GC-TCD operating conditions.

Table 3.4: GC-TCD operating conditions.

Parameter	Conditions
Injector Temperature	100 °C
Column Temperature	70 °C
Column Pressure	150 kPa
Detector temperature	250 °C

The TCD response factors for the gases used in FT synthesis, that is H_2, CO, N_2 and the reactor products such as CO_2 and CH_4, were determined from a standard gas mixture (see Table 3.5). To obtain these response factors, the GC-TCD was calibrated using the gas mixture and the response factors were calculated using the following equation:

$$f_{TCD} = \frac{[Ref\ gas] \cdot A_{analyte}}{[Analyte] \cdot A_{Ref\ gas}} \tag{3.12}$$

Table 3.5: Standard gas composition mixture.

Compound	Vol%	Response factors relative to N_2
H_2	39.70	9.33 ± 1.12
CO	19.90	0.971 ± 0.132
N_2	4.90	1
CO_2	9.70	1.33 ± 0.10
CH_4	15.30	3.92 ± 0.61
Ar	10.50	-

Peak areas (A) and response factors (f_{TCD}) were used to calculate molar flowrates ($n_{analyte}$) for the reactor effluent knowing the flow rate of the internal standard N_2.

$$\dot{n}_{analyte} = \left(\frac{1}{f_{TCD}}\right)\left(\frac{A_{analyte}}{A_{N_2}}\right).\dot{n}_{N_2} \tag{3.13}$$

Using N_2 as reference (A_{N_2}), the conversion of carbon monoxide (X_{CO}) was calculated as follows:

$$X_{CO} = 1 - \frac{A_{CO,out} / A_{N_2,out}}{A_{CO,in} / A_{N_2,in}} \quad (3.14)$$

The following equations were used to determine CH_4 selectivity and CO_2 selectivity:

$$S_{CH_4} = \frac{\dot{n}_{CH_4}}{\dot{n}_{CO_{in}} - \dot{n}_{CO_{out}}} \cdot 100\% \quad (3.15)$$

$$S_{CO_2} = \frac{\dot{n}_{CO_2}}{\dot{n}_{CO_{in}} - \dot{n}_{CO_{out}}} \cdot 100\% \quad (3.16)$$

Offline GC-FID Analysis

GC-FID was used to analyse organic compound products formed during the Fischer-Tropsch synthesis. Ampoules were filled and taken to GC-FID for analysis. Table 3.6 summarizes the operating conditions of the GC-FID.

Table 3.6: GC-FID operating conditions.

Mode	**Split**
Split Ratio	7.00
Injector temperature	200 °C
Column	CP-Sil 5CB
Temperature program	-55 °C hold 1.50 mins
	-55 °C to 0 °C at 20 °C/min
	0 °C to 100 °C at 14 °C/min
	100 °C to 280 °C at 10 °C/min
Detector temperature	200 °C
H_2 flow	30 ml/min
Air flow	300 ml/min
Make up gas (N_2) flowrate	25 ml/min

The reactor gaseous effluent was drawn out of a sample ampoule using a syringe and injected into the FID unit. The analysis time was ca. 70 mins.

The molar flowrates of the organic products detected from the GC-FID analysis was linked to the CH_4 flowrate as determined from the GC-TCD measurements (equation 3.13).

$$\dot{n}_{\iota} = \frac{\left(\frac{A_i}{C_{n-i}}\right)}{\left(\frac{A_{CH_4}}{C_{CH_4}}\right).C_{n-i}} \cdot \dot{n}_{CH_4} \tag{3.17}$$

C_{CH_4} is the carbon number of the reference gas (CH_4) and C_{n-i} is the carbon number of the organic product with i carbon atoms. Equation 3.18 was used to calculate selectivity for each hydrocarbon.

$$S_{C_i} = \frac{\dot{n}_{C_i}}{\dot{n}_{CO_{in}} - \dot{n}_{CO_{out}}} \tag{3.18}$$

Organic product selectivities, on a carbon basis, for $C_{2\text{-}4}$ and C_{5+}, were calculated as follows:

$$S_{C_{2-4}} = S_{CH_4} \cdot \frac{\sum_{i=2}^{C_{n-4}} i \cdot \dot{n}_{\iota}}{\dot{n}_{CH_4}} \tag{3.19}$$

$$S_{C_{5+}} = 1 - S_{C_{2-4}} - S_{CH_4} - S_{CO_2} \tag{3.20}$$

The n-olefin content and 1-olefin content in mol % were calculated directly from the product distribution obtained from the GC-FID:

$$S_{n-olefin,C_N} = \frac{\sum A_{n\ olefin,C_N}}{\sum A_{C_n-i}} \times 100\ \% \tag{3.21}$$

$$S_{1-olefin,C_N} = \frac{\sum A_{1-\ olefin,C_N}}{\sum A_{n-olefin\ ,C_N}} \times 100\ \% \tag{3.22}$$

$\sum A_{n\ olefin}$ is the sum of FID areas of all n-olefins with carbon number, C_N and $\sum A_{C_n-i}$ is the sum of FID areas of all linear hydrocarbons. $\sum A_{1-\ olefin,C_N}$ = the sum of FID areas of all 1-olefins with carbon number, C_N.

4 RESULTS

4.1 Inductively coupled plasma optical emission spectroscopy (ICP-OES)

Table 4.1 summarizes the cobalt and manganese loadings of the calcined supported catalyst precursors as determined using inductively coupled plasma optical emission spectroscopy (ICP-OES). $[Mn]_{initially}$ indicates the concentration of manganese (mg/L) in the potassium permanganate ($KMnO_4$) solution (V = 50 ml; pH = 1) to which the pre-calcined Co_3O_4/SiO_2 (m = 3.6 g) was exposed for 1 hr. The cobalt loading in the unpromoted catalyst was 22 wt.%. The addition of manganese did not significantly alter the cobalt loading of the calcined supported catalyst precursors. A negligible change in the cobalt loading is expected seeing the low solubility of Co_3O_4 and SiO_2 under these conditions (Elmer & Nordberg, 1958). The samples were further analysed to check if any potassium was adsorbed on the cobalt/silica catalyst during SEA of $[MnO_4]^{-1}$ anion from the potassium permanganate solution of pH = 1. No potassium was detected in the calcined catalysts. The potassium loading was below the detection limit of 0.01 wt.% in all samples.

Table 4.1: Summary of the elemental compositions determined using ICP-OES, before and after exposing the catalyst precursors to a solution of $KMnO_4$ containing different manganese concentration ($[Mn]_{initially}$, mg/L) at pH = 1 for 1 hr, followed by washing and calcination at 230 °C in flowing air.

Catalysts	$[Mn]_{initially}$, mg/L	$[Mn]_{initially}$, mmol/L	Co wt.%	Mn wt.%
Mn0	0	0	22	0.00
Mn16^{SEA}	290	5.3	21	0.16
Mn26^{SEA}	330	6.0	22	0.26
Mn42^{SEA}	952	17	21	0.42
Mn55^{SEA}	1897	35	22	0.55

The uptake of manganese by the calcined Co_3O_4/SiO_2 catalyst precursor from the SEA solution containing different concentrations of manganese can be reasonably described using a Langmuir isotherm:

$$Mn_{loading}(wt.\%) = 0.80 \cdot \frac{0.00115 \cdot [Mn]}{1 + 0.00115 \cdot [Mn]}$$

with [Mn] in mg/L. The manganese content should be correlated with the final concentration of manganese in the solution as manganese taken up by the catalyst and the manganese in the equilibrated solution. The manganese concentration in the equilibrated solution was not determined but could be calculated from the initial manganese concentration and the amount of manganese taken up from the solution (the manganese uptake was between 20% and 50% of the initial amount of manganese in the solution). The uptake of manganese can be again described using a Langmuir isotherm, albeit with a slightly higher adsorption constant (0.0019 L/mg). The maximum uptake was close to the maximum uptake determined using the initial concentration of manganese (0.73 wt.%).

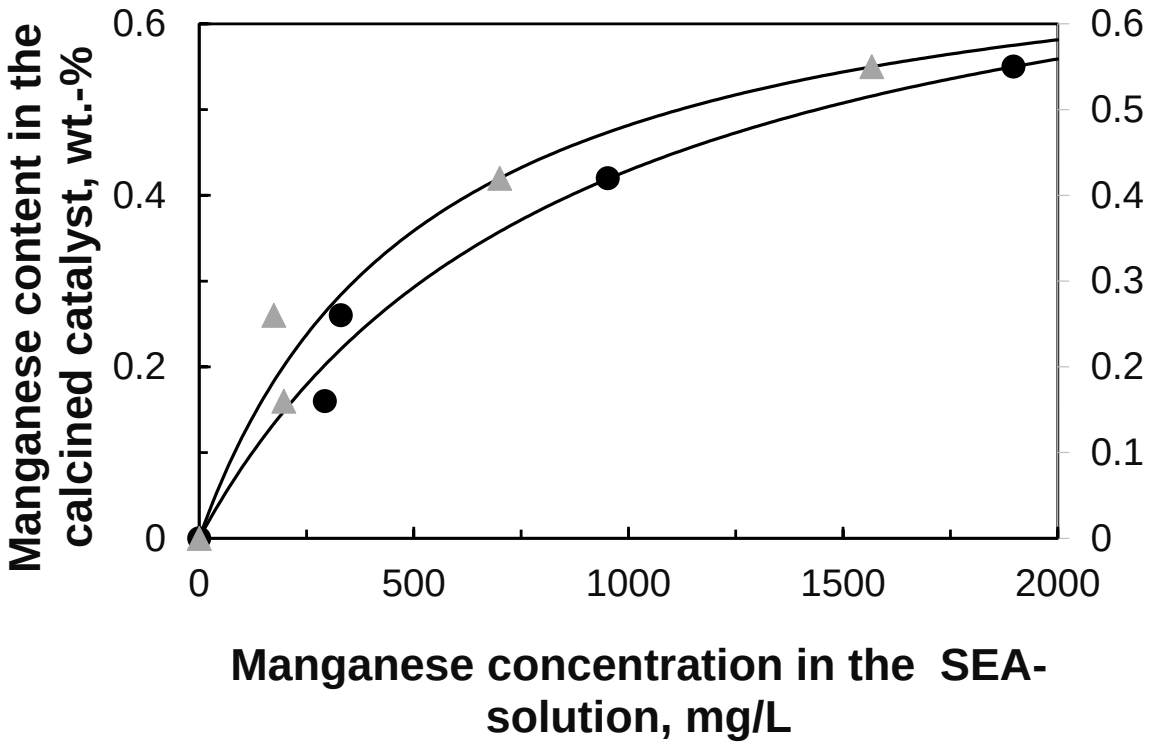

Figure 4.1: Manganese uptake by the catalyst precursor, Co_3O_4/SiO_2, exposed to SEA solution at pH = 1 containing different manganese concentrations for 1 hr, followed by washing and calcining at 230 °C in flowing air (●: initial manganese concentration in the SEA-solution; ▲: calculated manganese concentration in the final solution).

4.2 Powder X-ray diffraction (PXRD)

Powder X-ray diffraction patterns (PXRD) for the as-prepared and modified Co_3O_4/SiO_2-based catalysts are shown in Figure 4.2. All samples show diffraction lines located at 2θ = 22.2°, 36.1°, 42.5°, 45.1°, 52.1°, 64.9°, 70.3°, 77.9° and 93.4°, which were indexed to (111), (220), (311), (222), (400), (422), (511) and (440) planes of the spinel Co_3O_4 structure, respectively. Previous reports have shown that the promotion of Co/TiO_2 (Morales *et al.,* 2005; Morales *et al.,* 2007) and Co/SiO_2 (Dinse *et al.,* 2012) catalyst precursors with manganese resulted in peak shifts and decreased peak intensities with peak-width broadening in the samples containing a higher manganese loading. This was attributed to the formation of strained/mixed Mn-Co_3O_4 spinel structures and decreased cluster crystallinity. In this study, the addition of manganese to the catalyst precursor did not change the positions of the Co_3O_4 reflections or result in decrease in the peak intensity with increasing manganese concentrations. This may have been expected since the Co_3O_4 nanoclusters were doped with low manganese concentrations, which could have only resulted in minor shifts due to formation of a mixed spinel structure.

Furthermore, additional diffraction lines attributable to pure MnO_x were not detected. The average crystalline domain sizes of Co_3O_4 in the Mn^{SEA}-Co/SiO_2 catalysts were estimated using Debye-Scherrer equation from the most intense (311) diffraction line of the PXRD data. As shown in Table 4.2, the Mn^{SEA}-Co_3O_4/SiO_2 catalysts gave an average crystalline domain sizes of approximately 14 nm. This suggests that the adsorption of manganese on Co_3O_4/SiO_2 catalyst precursors did not induce any change in the crystalline domain size of Co_3O_4 particles.

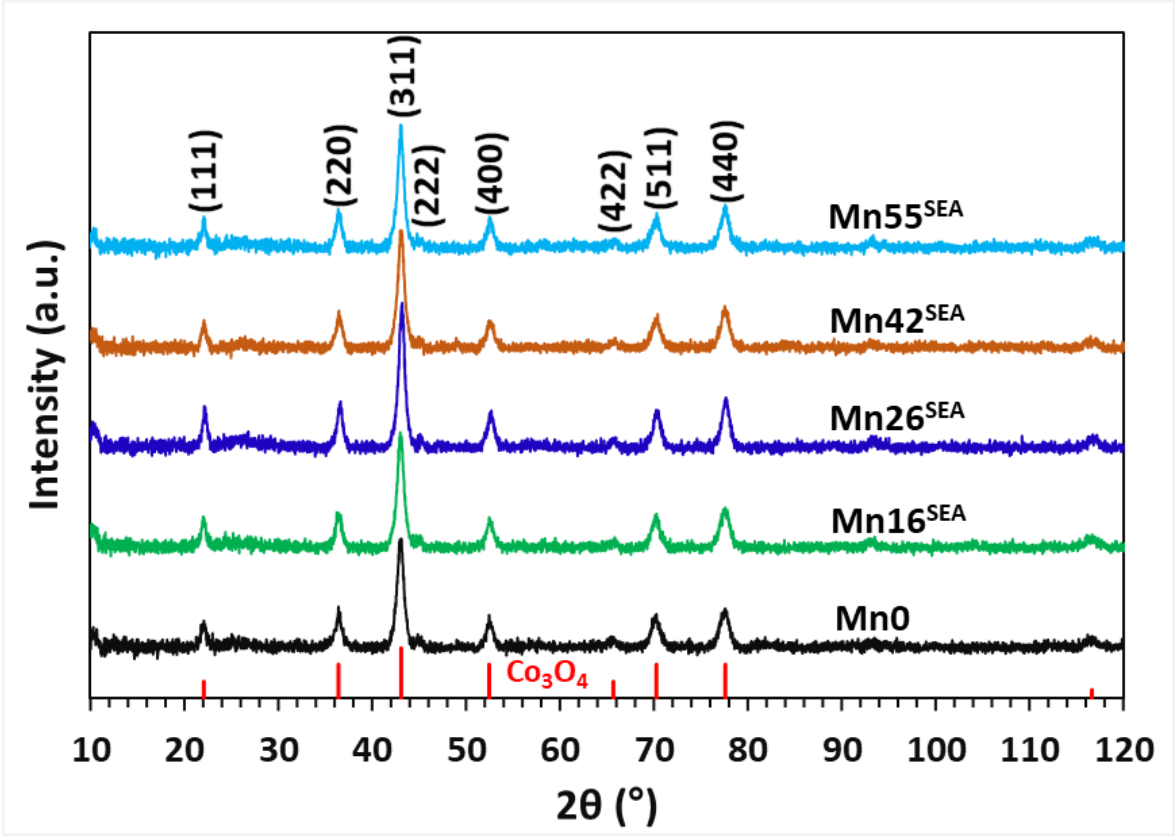

Figure 4.2: XRD patterns of Co_3O_4/SiO_2 with different manganese loadings prepared using strong electrostatic adsorption (SEA).

:

Table 4.2: Summary of the crystalline domain sizes of Co_3O_4 in the calcined Mn-Co/SiO_2 catalyst precursor prepared using strong electrostatic adsorption (SEA) from a $KMnO_4$ solution at pH = 1 (Co loading = 22 wt.%).

Catalyst	Co_3O_4 crystallite size (nm)
Mn0	14
Mn16^{SEA}	15
Mn26^{SEA}	14
Mn42^{SEA}	14
Mn55^{SEA}	14

4.3 Transmission electron microscopy (TEM)

The impregnation (IMPR) of cobalt(II) nitrate hexahydrate on SiO_2 support results in the formation of larger clusters due to the formation of cobalt nitrate droplets during the drying process (Feller *et al.,* 1999). The cluster size distributions of the unpromoted and manganese promoted Co_3O_4/SiO_2 nanostructures were analysed by transmission electron microscopy (TEM), as shown in Figure 4.3. The darker regions show representative unpromoted and manganese promoted Co_3O_4 nanostructures with good mono-dispersity on the support material (SiO_2). All these nanostructures are observed to display spherical shapes, as revealed by TEM bright field (BF) images. The inserts, shown at the right bottom corner of individual TEM images are enlarged TEM-BF images of these Co_3O_4-based nanostructures. A closer look at the magnified micrographs shows that these Co_3O_4-based structures are nanoclusters of single crystals with some degree of porosity, constructed in a controlled near-spherical manner.

Size distributions of the unpromoted and manganese promoted Co_3O_4 nanoclusters, calculated from TEM bright field images of 300 arbitrarily selected individual nanoparticles using ImageJ, are shown in Figure 4.4. The cluster-size distribution was modelled using a log-normal distribution. All these Co_3O_4-based nanoclusters supported on SiO_2 material display a rather narrow cluster size distribution as indicated by the standard deviation values (average size ± standard deviation) of Mn0 (262.1 ± 6.9 nm), Mn16^{SEA} (243.0 ± 5.5 nm), Mn26 ^{SEA} (308.4 ± 10.8 nm), Mn42^{SEA} (311.7 ± 6.0 nm) and Mn55^{SEA} (262.1 ± 6.6 nm) nanoclusters. Table 4.3 summarizes the measured average sizes of these supported Co_3O_4-based nanoclusters. The subtle differences

observed in average nanocluster sizes are associated with inhomogeneous cluster formation during calcination of a cobalt precursor on SiO_2 support material. Although these Co_3O_4 nanoclusters were doped with different manganese concentrations post calcination, insignificant nanocluster changes are expected. In addition, the $KMnO_4$ solution (pH = 1) used to selectively adsorb manganese onto the pre-formed Co_3O_4 nanoclusters did not appear to alter the initial sizes and shapes of pure Co_3O_4 catalyst precursor. Similar large particle size distributions of Co_3O_4/SiO_2 with a cobalt loading of 20 wt.% have been reported previously (Saib *et al.,* 2002; Feller *et al.,* 1999). These findings suggest that the inclusion of different manganese concentrations did not alter the morphology and size distribution of Co_3O_4 nanoclusters.

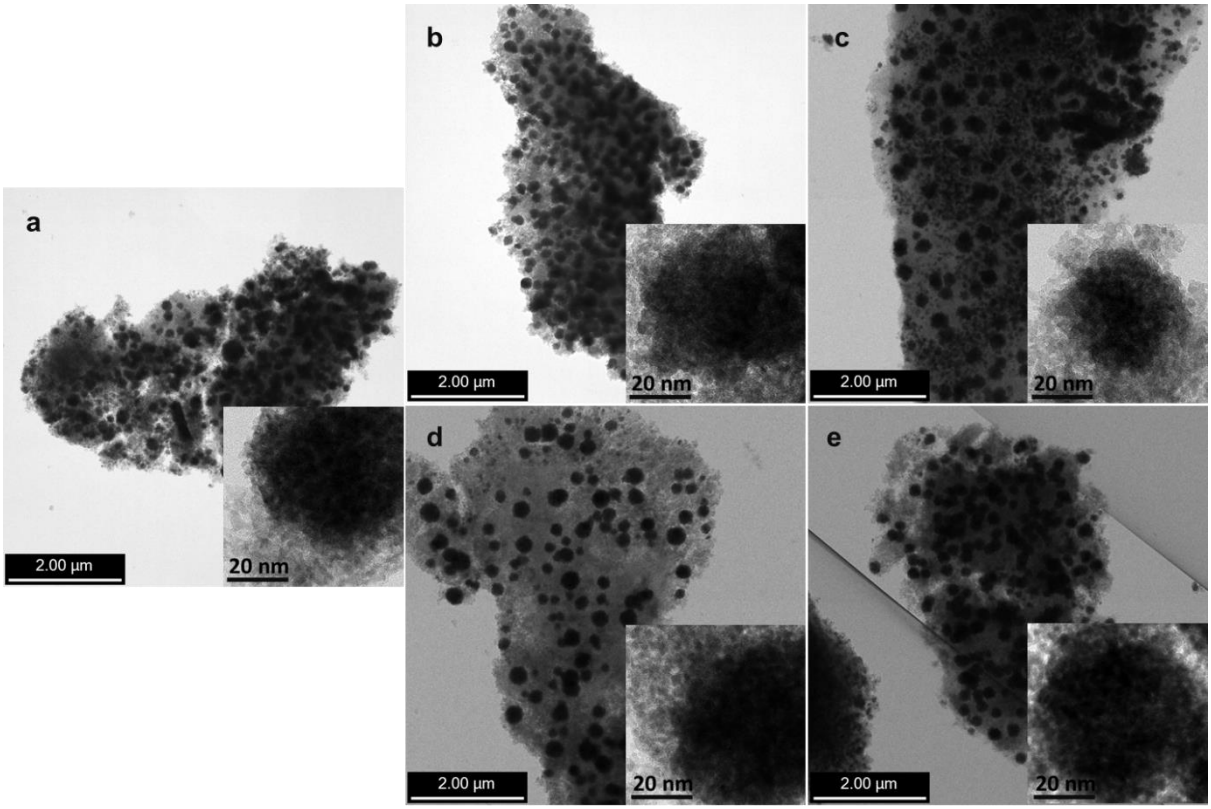

Figure 4.3: TEM bright field (TEM-BR) images of the calcined catalyst precursor before and after exposing to a $KMnO_4$ solution at pH = 1 for 1 hr, followed by washing and calcining at 230 ℃ in flowing air: (a) Mn0, (b) $Mn16^{SEA}$, (c) $Mn26^{SEA}$, (d) $Mn42^{SEA}$ and (e) $Mn55^{SEA}$ nanostructures. Inserts are enlarged TEM-BR micrographs of these Co_3O_4-based structures showing the spherical nanoclusters of single crystals.

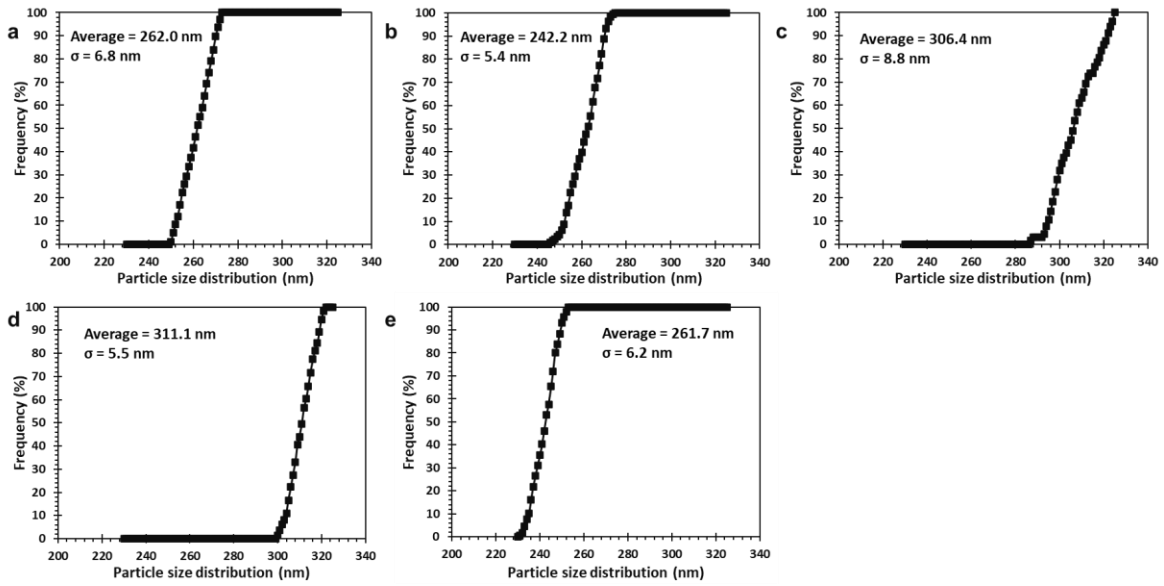

Figure 4.4: Log-normal distributions of the measured sizes of 300 nanoclusters: (a) Mn0, (b) Mn16^{SEA}, (c) Mn26^{SEA}, (d) Mn42^{SEA} and (e) Mn55^{SEA}.

Table 4.3: Mean sizes of Co_3O_4 nanoclusters in the calcined Mn-Co_3O_4/SiO_2 catalyst precursor prepared using strong electrostatic adsorption (SEA) from a $KMnO_4$ solution at pH = 1 (Co loading = 22 wt.%).

Catalyst	Average cluster size (nm)
Mn0	262.0 ± 6.8
Mn16^{SEA}	242.2 ± 5.4
Mn26^{SEA}	306.4 ± 8.8
Mn42^{SEA}	311.1 ± 5.5
Mn55^{SEA}	261.7 ± 6.2

4.4 Scanning transmission electron microscopy coupled with energy dispersive X-ray spectroscopy (STEM-EDS)

Scanning transmission electron microscopy (STEM) coupled with energy dispersive X-ray spectroscopy (EDS) was used to analyse the spatial distribution of cobalt and manganese on the support. Figure 4.5 (first column) shows high angular annular dark field (HAADFT) images of (a) Mn0, (b) $Mn42^{SEA}$ and (c) $Mn55^{SEA}$. Second column (blue) and the last column (green) show elemental distributions of cobalt and manganese, respectively. These observations suggest that manganese is associated with cobalt, which is consistent with previous reports by Bezemer *et al.* (2006). STEM EDS was also used to analyse for potassium as a way of validating the ICP-OES results and no potassium was detected.

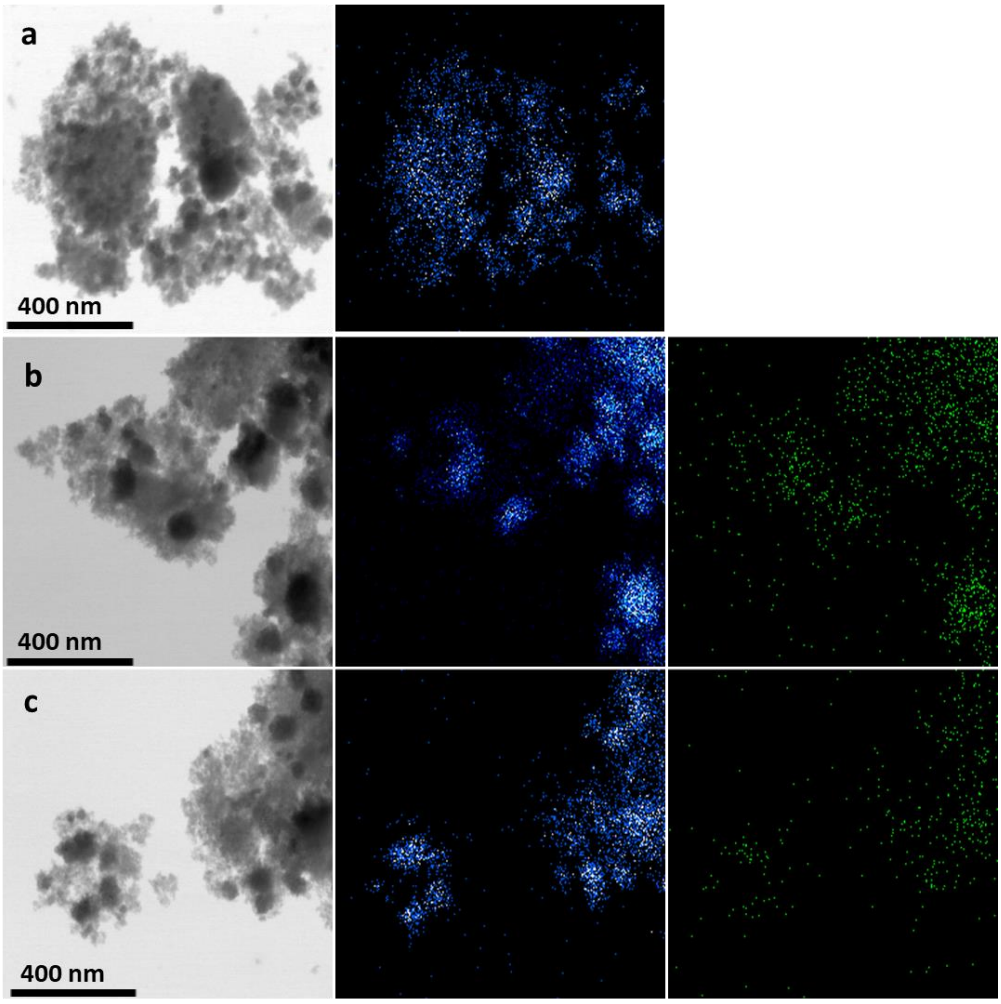

Figure 4.5: (a-c) HAADF images (first column), cobalt distribution (second column, blue), manganese distribution (the last column, green) in (a) Mn0, (b) $Mn42^{SEA}$ and (c) $Mn55^{SEA}$ showing homogeneous distributions on Co_3O_4/SiO_2 prepared using strong electrostatic adsorption (SEA).

4.5 Temperature programmed reduction (TPR)

Temperature programmed reduction in hydrogen (H_2-TPR) was carried out to investigate the reduction behaviour of Mn^{SEA}-Co/SiO_2 catalyst precursors. The samples were dried at 100 °C in an Ar flow and subsequently heated to 900 °C in 5% H_2/Ar using a heating rate of 10 °C/min. Figure 4.6 shows the H_2-TPR profiles for five Mn^{SEA}-Co/SiO_2 catalysts. Each profile has at least 2 maxima with the last maximum followed by a long tail. The dotted lines indicate the temperature at which the rate of reduction is the highest for each of the reduction steps.

The H_2-TPR profile of the unpromoted cobalt catalyst is similar to the ones obtained by amongst others van Steen *et al.* (1996), Sun *et al.* (2000) and de Beer *et al.* (2014). The H_2-TPR profile of the unpromoted Co_3O_4/SiO_2 catalyst consists of two low temperature peaks, one at ca. 150 °C and the other at ca. 260 °C. The first low temperature peak at ca. 150 °C is attributed to the thermal decomposition of the residual nitrates due to incomplete decomposition of the cobalt nitrate precursor (de Beer *et al.*, 2014). The addition of manganese to the unpromoted catalyst resulted in the disappearance of the first low temperature peak at ca. 150 °C. This may be attributed to nitrate leaching from the calcined Co_3O_4/SiO_2 catalyst precursors during its exposure to an aqueous solution of $KMnO_4$ at pH = 1 for 1 hr.

The second low temperature peak at ca. 260 °C is generally attributed to the first reduction step ($Co_3O_4 \rightarrow CoO$) (van Steen *et al.,* 1996) The peak maximum of the second low temperature reduction peak is shifted to a lower value than the value obtained by de Beer *et al.* (2014), Sun *et al.* (2000) and van Steen *et al.* (1996). Sun *et al.* (2002) obtained a low temperature peak at 310 °C whilst van Steen *et al.* (1996) and de Beer *et al.* (2014) obtained a low temperature peak at ca. 280 °C. This peak position is dependent on several operative parameters: H_2 concentration in the carrier gas, H_2 flowrate, the amount of sample used and heating rate (Marlet *et al.,* 1988; Pirola *et al.,* 2018). This may explain some of the discrepancies observed in peak positions. The addition of manganese to the unpromoted catalyst precursor did not change the position or magnitude of this reduction peak. This is expected due to low manganese concentrations used to modify the pre-formed Co_3O_4/SiO_2 catalyst precursors.

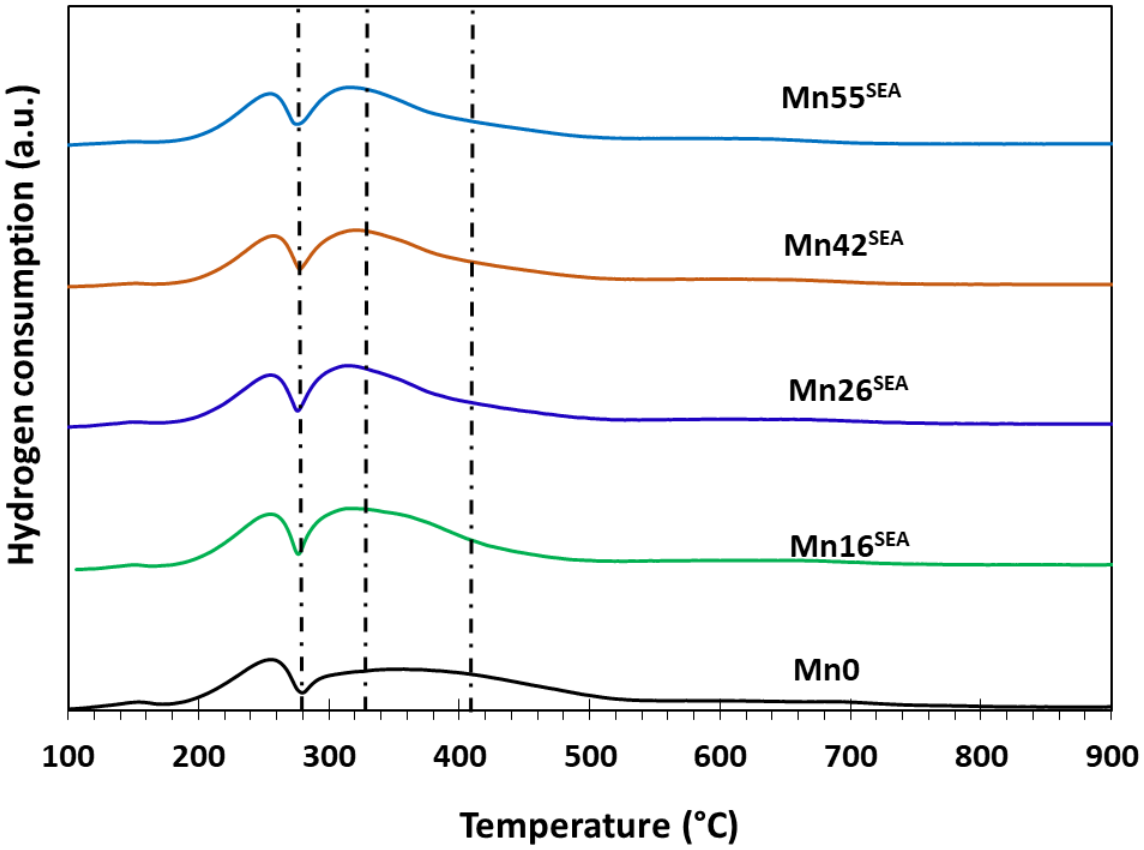

Figure 4.6: H_2-TPR profiles of calcined Mn-Co/SiO_2 catalysts with different Mn loadings prepared using strong electrostatic adsorption (SEA).

The H_2-TPR profile of the unpromoted Co_3O_4/SiO_2 also displays a broad high temperature peak between 280 °C and 540 °C. The broad peak indicates the existence of several species at the same reduction temperature (van Steen *et al.*, 1996). However, the broad high temperature region of the unpromoted catalyst seems to constitute of two convoluted peaks, one with a maximum at ca. 300 °C and one much broader peak with a maximum at ca. 370 °C. Upon the addition of manganese, the latter part of the high temperature peak seems to merge with the early part of the high temperature peak making the high temperature peak narrower and sharper. It may be speculated that the sharper peak is due to the reduction of manganese in the catalyst. The reduction of permanganate on the catalyst to MnO would result in maximum of about 8% higher H_2-consumption during H_2-TPR (see Table 4.4). The observed effect however seems stronger and must then be attributed to a combined effect of the reduction of the permanganate ion and a re-distribution of cobalt ions in the system, rendering them more facile to reduce.

Table 4.4: H_2 consumption during TPR experiments for Mn^{SEA}-Co/SiO_2 catalysts (m = 0.1 g, ramp rate 10 C/min in 5% H_2/Ar (50 ml (NTP)/min).

Catalyst	H_2 consumption (mmol/g catalyst)
Mn0	1.1
Mn16^{SEA}	1.2
Mn26^{SEA}	0.60
Mn42^{SEA}	0.41
Mn55^{SEA}	0.42

4.6 Thermogravimetric analysis (TGA)

The degree of reduction for unpromoted and manganese promoted cobalt catalysts was determined using thermal gravimetric analysis (TGA). The specimens were heated from room temperature to 50 °C in N_2. The mass of the samples was stabilised for 15 mins, and thereafter the gas was switched to 5% H_2/N_2. After 5 mins, the samples were heated to 350 °C (at a ramp rate of 10 °C/min) and were kept at this temperature for 4 hrs. The TGA curves of both unpromoted and manganese promoted Co_3O_4/SiO_2 catalysts are shown in Figure 4.7. The mass of the sample with respect to time was normalised with the initial weight of the sample. The TGA weight loss curve for the unpromoted and promoted catalysts shows 5 well separated events. The first event at t=0-15 mins shows a decrease in mass. This is attributed to the buoyancy effect. Before the start of the TGA experiment, the N_2 flow in the furnace pushes the sample pan up (buoyancy effect), resulting in a decrease in mass (Gabbott, 2008; Menczel & Prime, 2014). The second event at t=15 mins shows a sharp decrease in mass. This occurs as a result of changing the gases from N_2 to 5% H_2/N_2. Subsequently, an increase in mass is observed to take 5 mins. This is also attributed to the buoyancy effect due to change in gas density (as a result of temperature change). The third event at t=20-30 mins shows a decrease in mass. This is attributed to the drying of the sample. The fourth event at t=30-50 mins is due to reduction of Co_3O_4 to CoO. The final event at t=50-295 mins is due to reduction of divalent cobalt to metallic cobalt.

It is worth highlighting that the addition of manganese did not significantly change the first 4 events of the unpromoted cobalt catalyst, although the addition of manganese ($Mn16^{SEA}$) slightly shifted the curve at t=15-20 mins downwards. Similarly, the final event at t=50-295 mins shifted downwards with a steeper slope. This suggests that the rate of reduction of divalent cobalt to metallic cobalt is faster. Furthermore, it was observed that the addition of more manganese ($Mn26^{SEA}$ and $Mn42^{SEA}$) resulted in a

change of the steepness of the slope for the final event. Furthermore, the final mass was a slightly higher than the unpromoted catalyst (see Figure 4.7). The sample $Mn55^{SEA}$ shows a more pronounced step relative to mass of 0.964 g. This suggests that an increase in the manganese loading results in a slower rate of reduction of divalent cobalt to metallic cobalt. The heights of the steps appear to be independent of the manganese content. A peculiar step for sample $Mn55^{SEA}$ was observed at ca. 255 mins possibly due to an error in the TGA measurement.

The degree of reduction of the unpromoted and promoted cobalt catalysts was calculated as shown in Appendix D It was assumed that cobalt was originally present as Co_3O_4. Therefore, the degree of reduction was based on the loss of oxygen in Co_3O_4 (i.e. from t=30 mins to t=295 mins). This will result in an underestimation of the degree of reduction, since some cobalt may be present in the form of cobalt silicates (van Steen *et al.*, 1996).

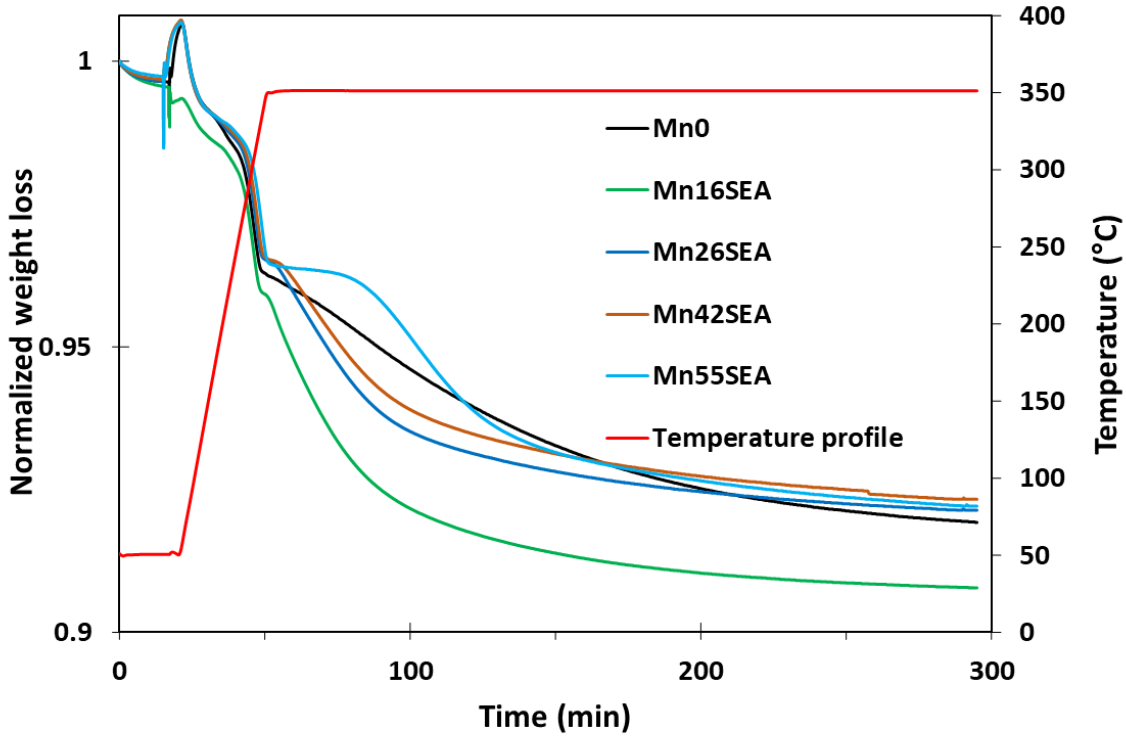

Figure 4.7: TGA weight loss curves for reduction of Co_3O_4/SiO_2 in 5% H_2/N_2 mixture for 4 hrs with different manganese loadings prepared using strong electrostatic adsorption (SEA).

Table 4.5 summarizes the degree of reduction for each sample. The degree of reduction of unpromoted cobalt catalysts was calculated to be 91%. The addition of a low amount of manganese to the sample ($Mn16^{SEA}$) increased the degree of reduction of unpromoted cobalt catalysts from 91% to 100%. A further increase in manganese decreased the degree of reduction of unpromoted catalyst from 91% to 88 %.

Table 4.5: Degree of reduction of Mn-Co/SiO_2 catalysts prepared using strong electrostatic adsorption (SEA) after reduction for 4 hrs in 5% H_2/N_2 at 350 °C.

Mn-Co/SiO_2 Catalysts	Degree of reduction
Mn0	91
$Mn16^{SEA}$	100
$Mn26^{SEA}$	89
$Mn42^{SEA}$	86
$Mn55^{SEA}$	88

4.7 Hydrogen chemisorption

Hydrogen (H_2) chemisorption analysis was carried out to determine the H_2 uptake, the metal surface area and the dispersion in unpromoted and manganese promoted Co/SiO_2 catalysts. The samples were degassed at 200 °C for 3 hrs. The unpromoted and promoted catalysts were reduced at 350 °C under a continuous flow of pure H_2 for 4 hrs after the system was flushed with He and evacuated. The H_2 adsorption isotherms were measured at 125 °C and collected in the pressure range of 0-600 mmHg (see Figure 4.8). The adsorption isotherms show a sharp increase in quantity of H_2 adsorbed with increase in pressure, followed by a gradual increase in the H_2 uptake. The origin of the latter is unclear, but it is speculated that this is due to either a small leak (despite passing the leak test) or H_2 spillover.

The adsorption isotherms were fit into a Langmuir adsorption model (see equation 4.1) accounting for the slow increase in the hydrogen uptake with increasing pressure:

$$V_{H_2-uptake} = V_{H_2-uptake,monolayer} \cdot \frac{K \cdot p_{H_2}^{0.5}}{1 + K \cdot p_{H_2}^{0.5}} + A \cdot p_{H_2}^{0.5} \qquad (4.1)$$

It was assumed that:

1. H_2 completely dissociates to two molecules of H when adsorbed.
2. All sites are equivalent.
3. Each cobalt surface can adsorb 1 atom of H.
4. No interaction between adsorbates on adjacent sites.

The observed data for all catalysts (blue dotted curve) fits the modified Langmuir adsorption model (solid black line) well.

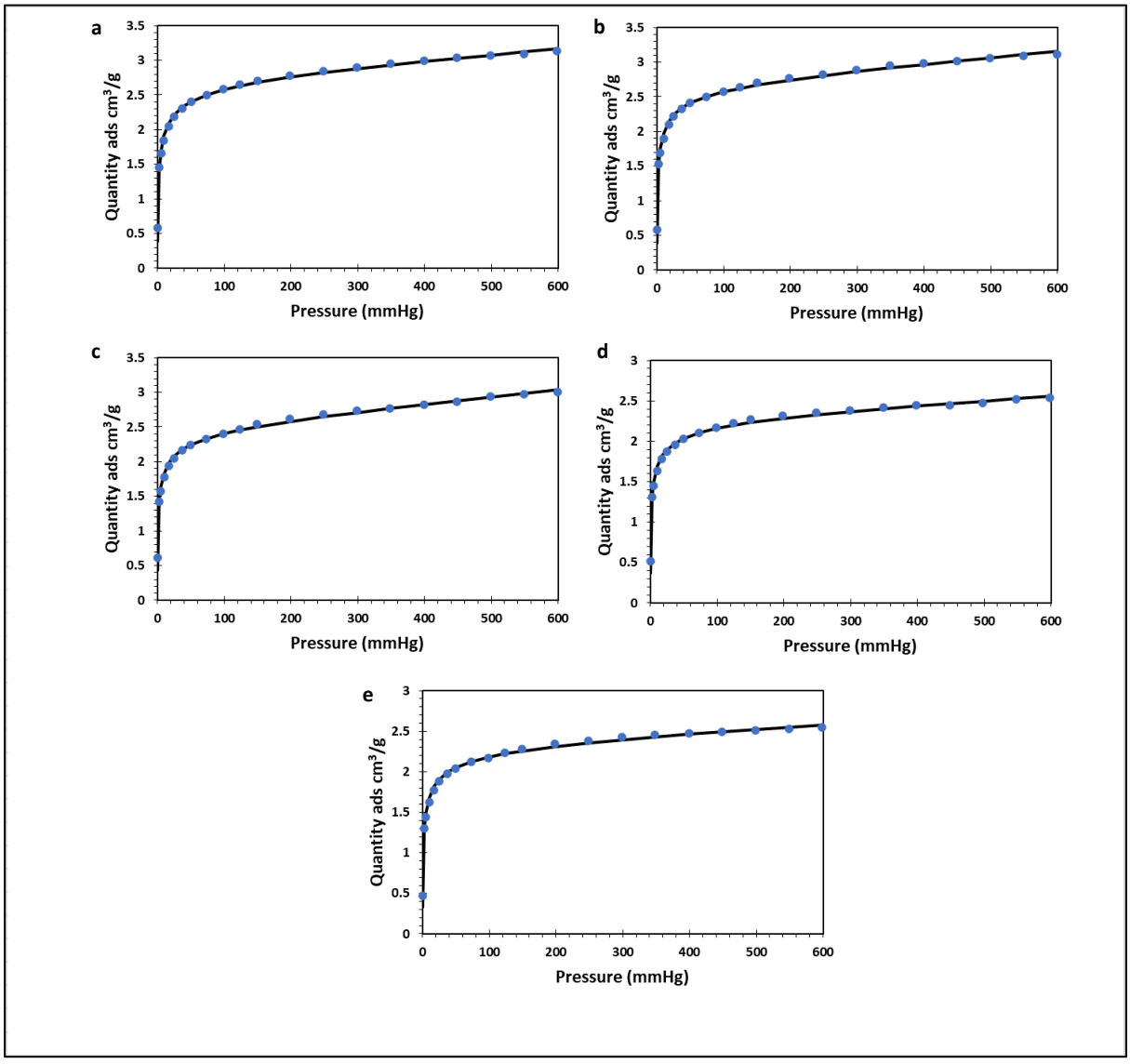

Figure 4.8: Adsorption isotherms (blue dots) and Langmuir adsorption fitted isotherms (solid black line) for manganese promoted cobalt catalysts prepared using strong electrostatic adsorption (SEA): (a) Mn0, (b) $Mn16^{SEA}$, (c) $Mn26^{SEA}$, (d) $Mn42^{SEA}$ and (e) $Mn55^{SEA}$.

The volume of the monolayer on the catalysts' surface (H_2 uptake) was calculated using equation 4.1. Table 4.6 summarizes the H_2 uptake, the metallic cobalt surface area, the cobalt dispersion and the average particle sizes. The metallic cobalt surface area decreases with increasing manganese concentration (see Table 4.6). The calculated mean particle size of the unpromoted catalyst (Mn0) determined from H_2 uptake was 12.5 nm. The obtained metal particle size is similar to the metal particle size obtained by Johnson *et al.* (2015) in their study on the effect of manganese on Co/SiO_2. The addition of manganese did not significantly change the mean particle size. This is expected because of the small amount of manganese added to the unpromoted catalysts. The H_2 uptake on the reduced unpromoted catalysts (Mn = 0 wt.%) is 0.130 mmol/g and thus the corrected dispersion was determined to be 7.0%. At the highest manganese loading ($Mn55^{SEA}$), the H_2 uptake decreased to 0.110 mmol/g. This may be associated with the blockage of active cobalt sites by manganese oxide species.

Table 4.6: H_2 chemisorption summary results for Mn^{SEA}-Co/SiO_2 reduced at 350 °C for 4 hrs in pure H_2.

Catalyst	H_2 uptake (mmol/g)	Co metal surface area (m^2/g of catalyst	Co Dispersion (%)	Corrected Co-dispersion	d_{Co} (nm)
Mn0	0.130	10.7	7.7	7.0	12.5
$Mn16^{SEA}$	0.127	10.5	7.1	7.1	13.5
$Mn26^{SEA}$	0.117	9.7	7.0	6.3	14.6
$Mn42^{SEA}$	0.108	8.9	7.0	6.0	13.6
$Mn55^{SEA}$	0.110	10.7	7.7	7.0	12.5

4.8 Temperature programmed desorption of CO (CO-TPD)

Prior to the measurement of the temperature programmed desorption of CO (CO-TPD), the Mn^{SEA}-Co/SiO_2 catalysts were dried at 100 °C for 1 hr under a continuous flow of N_2. The samples were cooled down to 40 °C and subsequently heated at 350 °C (ramp rate = 10 °C /min) in H_2 flow and kept at a reduction temperature of 350 °C for 4 hrs. After reduction, the samples were cooled down to 40 °C in He and pulse-fed with pure CO via a sample loop (V_{loop} = 0.31 ml) whilst flowing He as a carrier gas until the surface was saturated (ca. 6 doses). Surface saturation is achieved when least two peaks with constant area are detected, and this is followed by purging the samples with He. Subsequently, the catalyst was heated to 900 °C (ramp rate 10 °C/min) in He and CO desorption was monitored using an online thermal conductivity. Moreover, a

mass spectrometer was connected to the exhaust line of the Autochem II 2920 to detect the formation of CO_2 during CO-TPD.

Figure 4.9 shows the partial pressures of CO and CO_2 as a function of the desorption temperature measured by the mass spectrometer for sample $Mn16^{SEA}$. The amount of CO_2 released (e.g. by coupling of adsorbed CO with adsorbed O, the latter originating from dissociated CO) is very small (max. 1/3000 times the amount of CO), and its formation can thus be considered negligible. This suggests that adsorbed CO desorbs as molecular CO as the sample is heated to 900 °C and does not recombine yielding CO_2 to a significant extent.

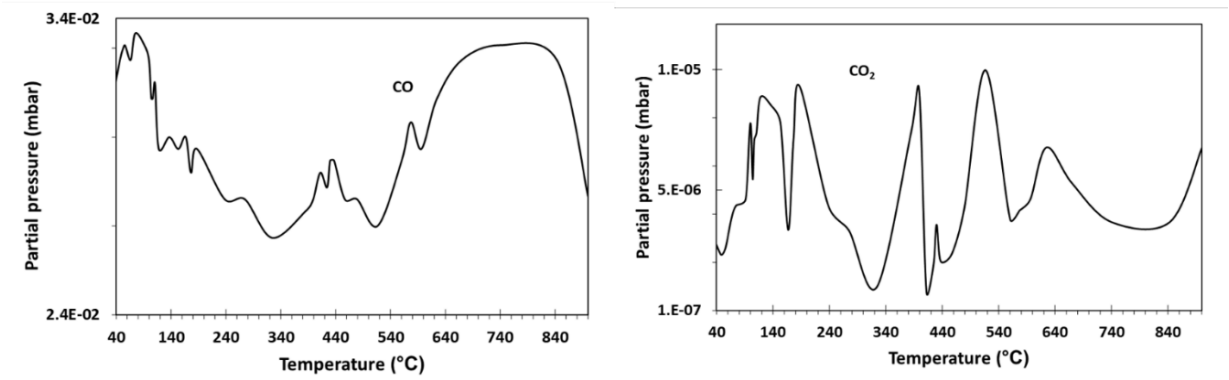

Figure 4.9: CO and CO_2 profiles of $Mn16^{SEA}$ as detected using a mass spectrometer.

The CO-TPD profiles for the five Mn^{SEA}-Co/SiO_2 catalysts are shown in Figure 4.10. Each profile contains two distinct desorption ranges, a low temperature range (40-370 °C) and high temperature range (370-800 °C). These temperatures may be attributed to associatively adsorbed and dissociatively adsorbed CO, respectively (Erley & Wagner, 1978; Hu & Ruckenstein, 1996; Viswanathan *et al.*,1981). The low temperature range shows two distinctly different peaks whilst the high temperature range displays a single peak. A new desorption feature at about 278 °C appears to develop for samples with manganese loadings higher than 0.26 wt.%. In addition to the new feature, it seems that with increasing manganese content, the area of the first peak relative to the area of the second peak in the low temperature range increases. This indicates that a greater pool of associated CO was bound in more weakly interacting sites when manganese was incorporated. The sample $Mn16^{SEA}$ shows a prominent first peak relative to the second peak, in the low temperature region. All these CO-TPD profiles are slightly different from the ones obtained by Johnson *et al.* (2015). Johnson *et al.* (2015) obtained 3 peaks: the first peak at -8 °C, second peak at 177 °C and the third peak in the high temperature desorption region of 327 °C and 427

°C. These peak discrepancies are due to different adsorption temperatures used. Johnson *et al.* (2015) pulse fed CO at -60 °C.

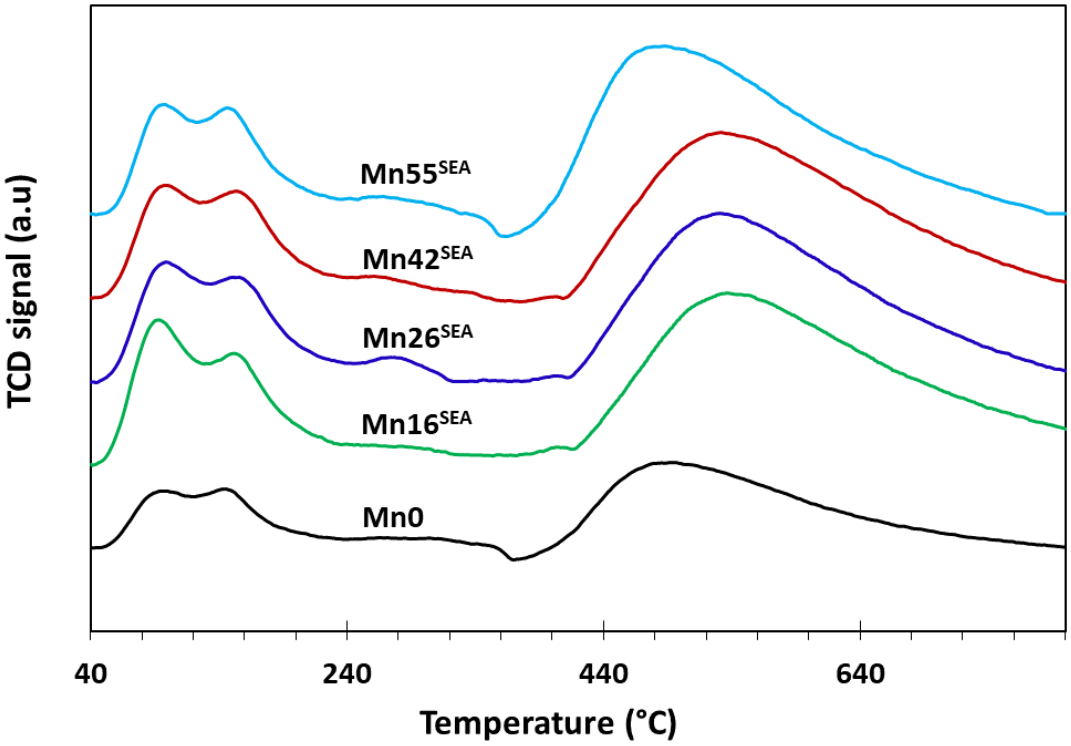

Figure 4.10: CO-TPD profile of Mn-Co/SiO_2 samples prepared using strong electrostatic adsorption (SEA) with different manganese loadings.

To quantify the amount of CO bound on the catalyst surface, the peak areas from the pulse chemisorption of CO were evaluated and normalized by the amount of sample used in carrying out CO-TPD experiment. Figure 4.11 shows the total amount of CO adsorbed as a function of the manganese content in the catalyst. The total amount of CO adsorbed from an unpromoted cobalt catalyst decreased from 0.0722 mmol CO/g to 0.0537 mmol CO/g with increase in manganese loading. This is ascribed to the decrease in cobalt metallic surface area.

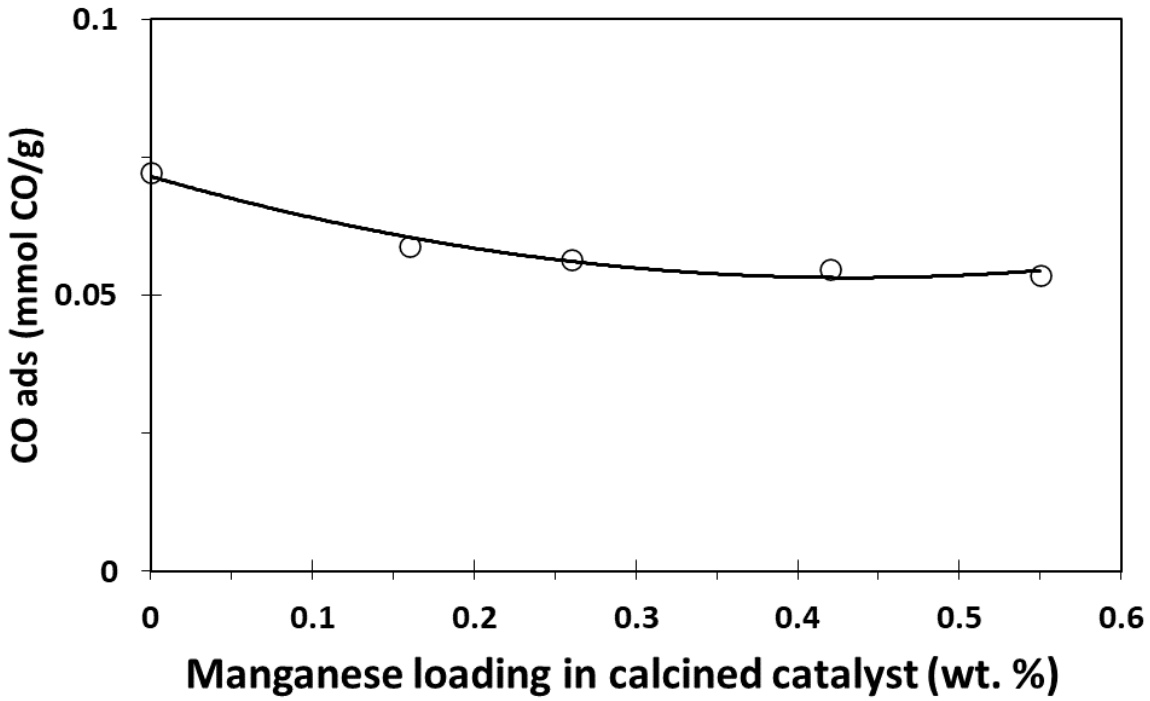

Figure 4.11: Total amount of CO adsorbed as a function of manganese loading in catalysts prepared using strong electrostatic adsorption (SEA).

Figure 4.12 shows the maximum temperature for each peak in a CO-TPD profile of Mn^{SEA}-Co/SiO_2 catalysts. Low temperature peaks (peak 1, peak 2 and peak 3, being the shoulder peak) show insignificant shifts in the maximum temperature. This suggests that the addition of manganese showed insignificant change on the strength of CO bound on weakly interacting sites. Johnson *et al.* (2015) observed a 5-20 °C increase in temperature of the low temperature peaks and attributed this to an increase in the CO adsorption strength.

The maximum temperature of the high temperature of the unpromoted cobalt catalyst was 488 °C. The addition of Mn = 0.16 wt.% increased the maximum temperature of the high temperature peak by ca. 56 °C. Using the Redhead analysis (appendix I), the activation energy for CO desorption from the reduced, unprompted catalyst is estimated to be 243 kJ/mol. An increase of the maximum temperature of the high temperature peak by ca. 56 °C results in an increase in the activation energy for the desorption of CO desorption by 7%. However, the addition of Mn = 0.26 wt.% and Mn = 0.42 wt.% increased the maximum temperature of the high temperature peak of the unpromoted cobalt catalysts by ca. 42 °C. The high temperature peak position obtained with the reduced catalyst containing Mn = 0.55 wt.% was similar to the unpromoted catalyst.. With the use of 95% confidence level, regression analysis was performed to understand the relationship between the manganese content and the shift

in high temperature peak positions. The R^2 value (0.019) is a measure of how much of the change in the maximum temperature of the high temperature peak is affected by the manganese content. This indicates that there is 2% variation in the maximum temperature of the peaks. The p-value for the slope of 0.82 is greater than the significance level of 0.05. This indicates that the slope is not significantly different from zero, thus there is no relationship between the manganese content and the maximum temperature of the high temperature peak and the manganese content. However, Johnson *et al.* (2015) only observed a change in maximum peak temperature in the low temperature peaks.

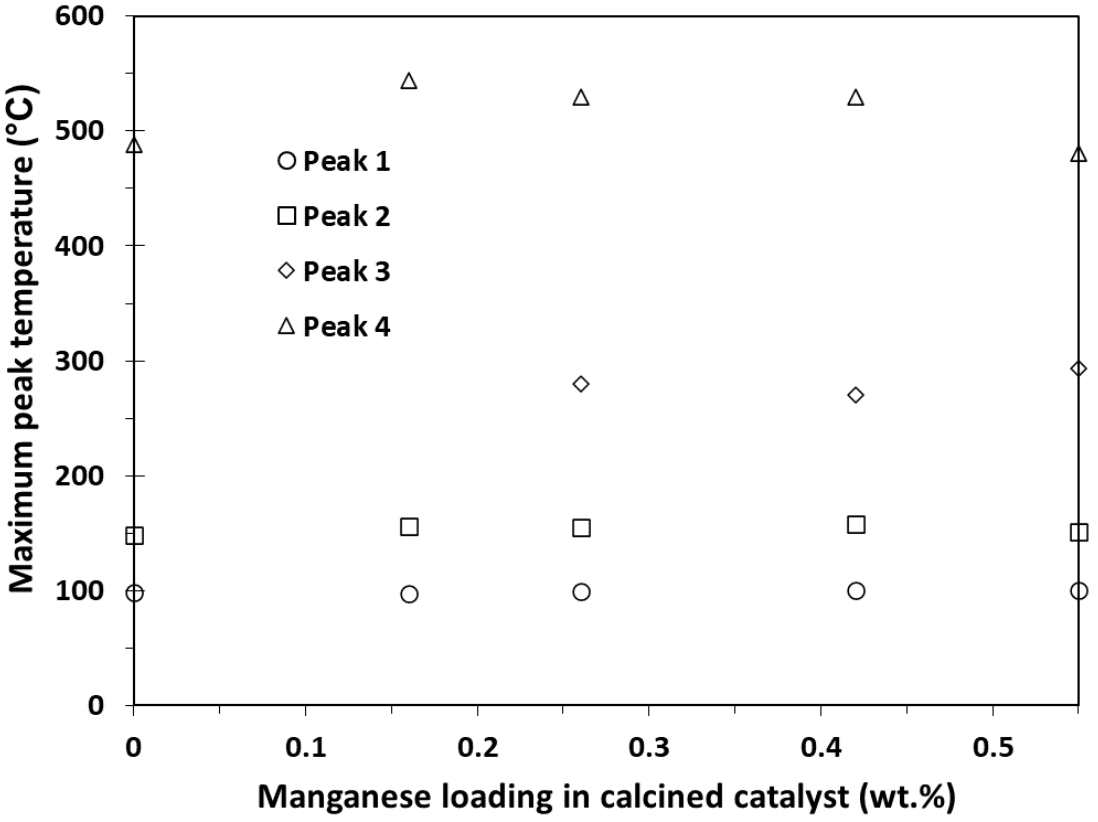

Figure 4.12: Maximum peak temperature for each peak in the CO-TPD profile for Mn-Co/SiO_2 catalysts prepared using strong electrostatic adsorption (SEA).

The area ratio of the high temperature peak to total area for each CO-TPD profile was calculated to check if the addition of manganese facilitated CO dissociation in the CO-TPD, assuming there is no CO loss in the adsorption/desorption process. Figure 4.13 shows the effect of manganese on the area ratios. The area ratio of the catalysts ranges from 0.69 to 0.75. The addition of Mn = 0.16 wt.% increased the area ratio of the unpromoted cobalt catalyst from 0.69 to 0.75 whereas the ratio obtained with the sample $Mn26^{SEA}$ was reduced to about 0.72. Slightly higher values (0.74) were

observed with higher manganese loadings. Regression analysis was performed to understand the relationship between the manganese content and the area ratio. The confidence level was chosen to be 95%. The R^2 value (0.26) is a measure of how much of the change in area ratio is influenced by the manganese content. This indicates that there is 26% variation in area ratio. The slope of 0.05 implies that there is no strong relationship between the manganese content and area ratio. In addition, the p-value for the slope of 0.38 is greater than the significance level of 0.05. This indicates that the slope is not significantly different from zero, thus there is no relationship between the manganese content and the area ratio.

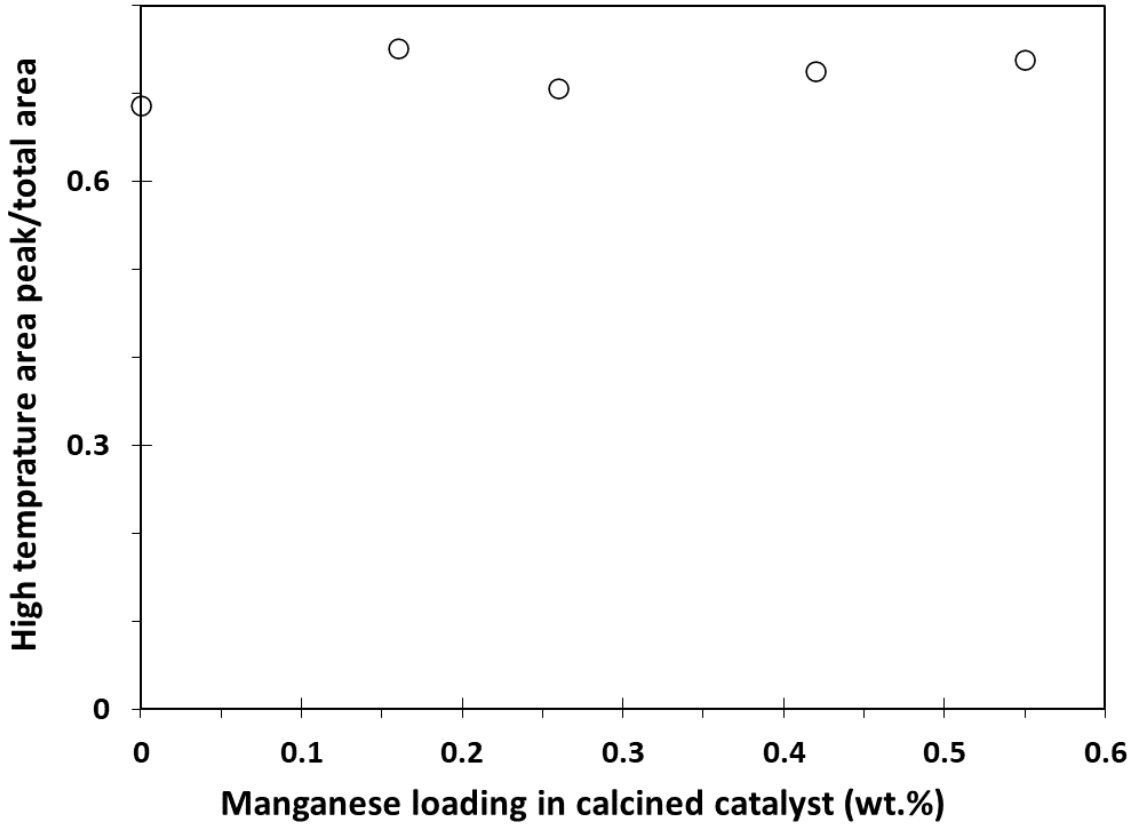

Figure 4.13: Area ratio of the high temperature peak in the CO-TPD relative to the total area as a function of the manganese loading in the calcined catalysts prepared using strong electrostatic adsorption (SEA).

4.9 Fischer-Tropsch synthesis

Five reactions were carried out at T = 220 °C, P = 20 barg with 0.5 g of each Mn^{SEA}-Co/SiO_2 catalysts loaded in a fixed bed reactor. Reactions 1 (R1) and 2 (R1) were

conducted using 0.5 g of Co_3O_4/SiO_2 to check for reproducibility. The graphs below show CO and H_2 flowrates for each reaction with respect to time.

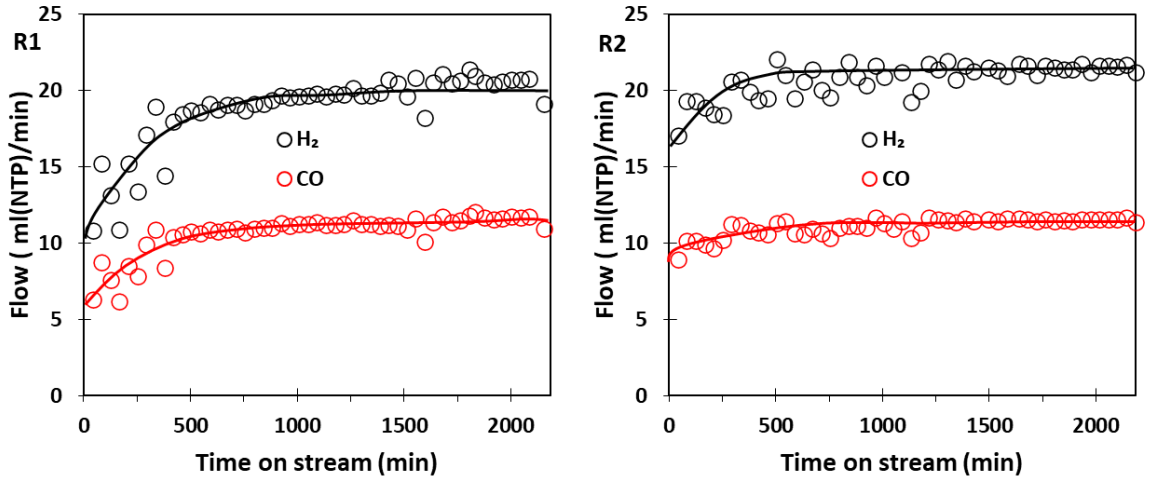

Figure 4.14: H_2 and CO outlet flowrate with respect to time for unpromoted cobalt supported on silica catalyst at 220 °C, 20 barg, an H_2/CO ratio of 2, and syngas flowrate of 60 ml (NTP)/min. R1 is the first reaction and R2 is the repeated reaction.

Table 4.7: Summary of H_2 and CO outlet flowrate for unpromoted cobalt catalyst at pseudo steady state.

Catalyst	H_2 flowrate (ml (NTP)/min)	CO flowrate (ml (NTP)/min)
R1-Co/SiO_2	20±0.7	11±0.4
R2-Co/SiO_2	21±0.7	11 ±0.3

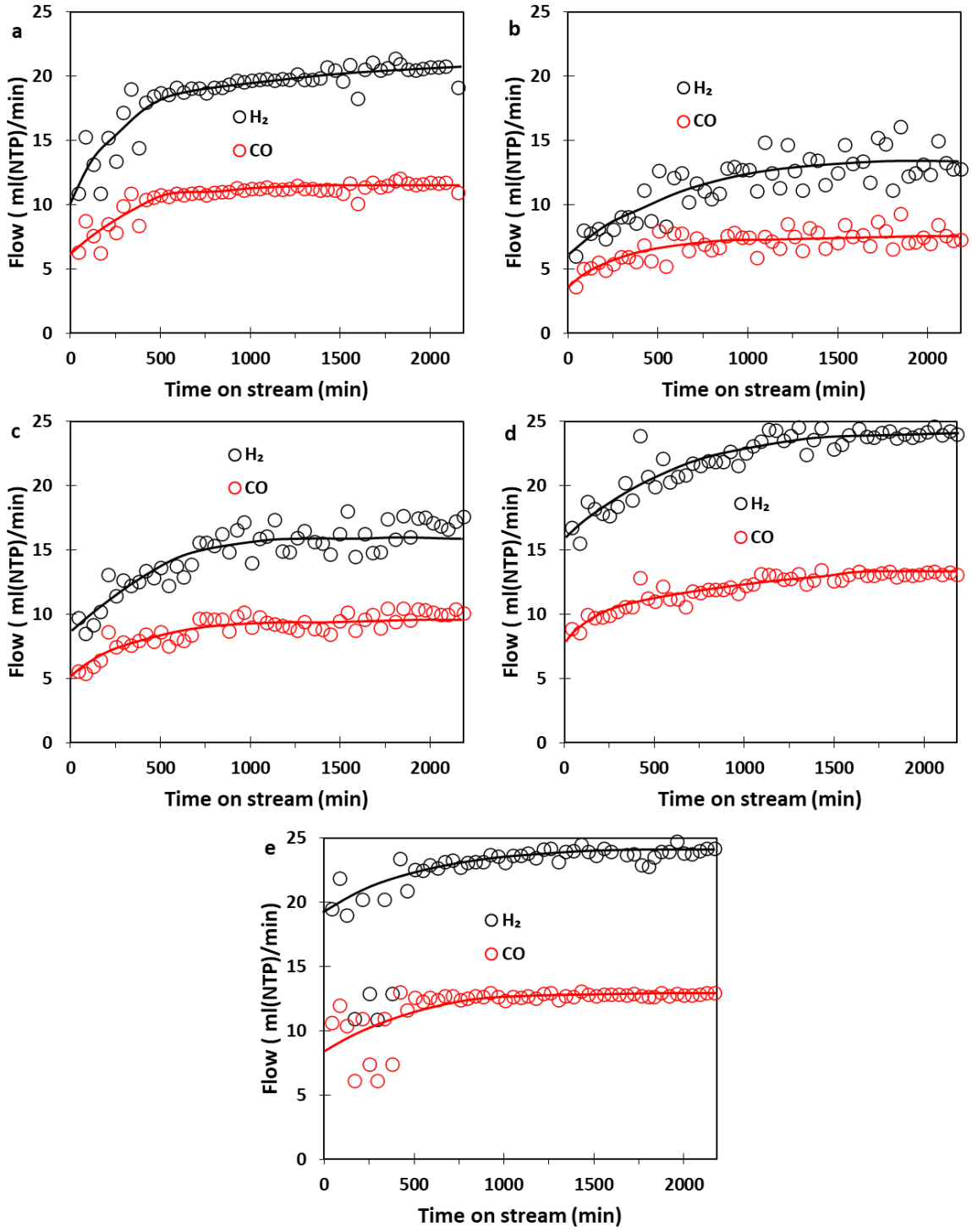

Figure 4.15: H_2 and CO flowrate with respect to time for Mn^{SEA}-Co/SiO_2 catalysts with different manganese concentrations in 50 ml of potassium permanganate solution: (a) Mn0 , (b) $Mn16^{SEA}$, (c) $Mn26^{SEA}$, (d) $Mn42^{SEA}$ and (e) $Mn55^{SEA}$ at 220 °C, 20 barg, an H_2/CO ratio of 2, and syngas flowrate of 60 ml(NTP)/min.

Table 4.8: Reactions carried out at T = 220 °C, P = 20 barg and H_2/CO = 2 with 0.5 g of each Mn^{SEA}-Co/SiO_2 catalyst loaded in a fixed bed reactor.

Catalyst	H_2 flowrate (ml (NTP)/min)	CO flowrate (ml (NTP)/min)
Mn0	20±0.67	11 ±0.36
$Mn16^{SEA}$	13 ±1.3	7.5 ±0.74
$Mn26^{SEA}$	16 ±1.2	9.6 ± 0.61
$Mn42^{SEA}$	24 ± 0.53	13 ± 0.28
$Mn55^{SEA}$	24 ± 0.59	13 ± 0.18

4.9.1.1 Reproducibility

The unpromoted Co_3O_4/SiO_2 catalyst (mass = 0.5 g) was loaded in a fixed bed reactor. Prior to catalyst reduction and catalyst testing, the reactor was pressurized with Ar to 20 barg. The reactor was left for 24 hrs and no pressure losses were observed. The reactor was then depressurized to 1 barg and the catalyst was heated from room temperature to 350 °C at a heating rate of 10 °C/min in H_2 flow. The catalyst was then kept at this temperature for 4 hrs. After reduction was complete, the reactor was cooled down to 200 °C and flushed with Ar. The reactor was then pressurized to 20 barg, whilst flowing Ar through the reactor. Synthesis gas with H_2/CO = 2 was directed through the reactor bypass by individually controlling the mass flow rate of H_2 and CO. After the expansion valve, N_2 was added to the reactor effluent. The total reactor effluent was directed to the online GC-TCD for analysis to verify the feed gas composition. Subsequently, the syngas flow was directed to the reactor, whilst the Ar flow was directed to the bypass to start the reaction. The reactor was slowly heated up to 220 °C at a heating rate of 0.8 °C/min. As soon as it reached the reactor temperature, the reactor effluent was sent to the GC-TCD for product analysis. The reaction was performed for a total reaction time of 48 hrs. To check for reproducibility, the experiment described above was repeated.

Figure 4.16 shows the CO-conversion as a function of time on stream for both experiments. Experiment 1 (R1) and repeated experiment (R2) show a decrease in CO-conversion from the start of the reaction (t = 0 to t = 210 mins). Both experiments show a bit of scatter in the data in this time period. This may be attributed to the variations in settling down of the catalyst at the beginning of the catalyst. The CO-conversion profiles show a gradual decrease of conversion with time, but it seems to reach a pseudo steady state after ca. 1500 mins online with a conversion 46 ± 2%. Since both catalysts gave the same activity, the product spectrum was analysed.

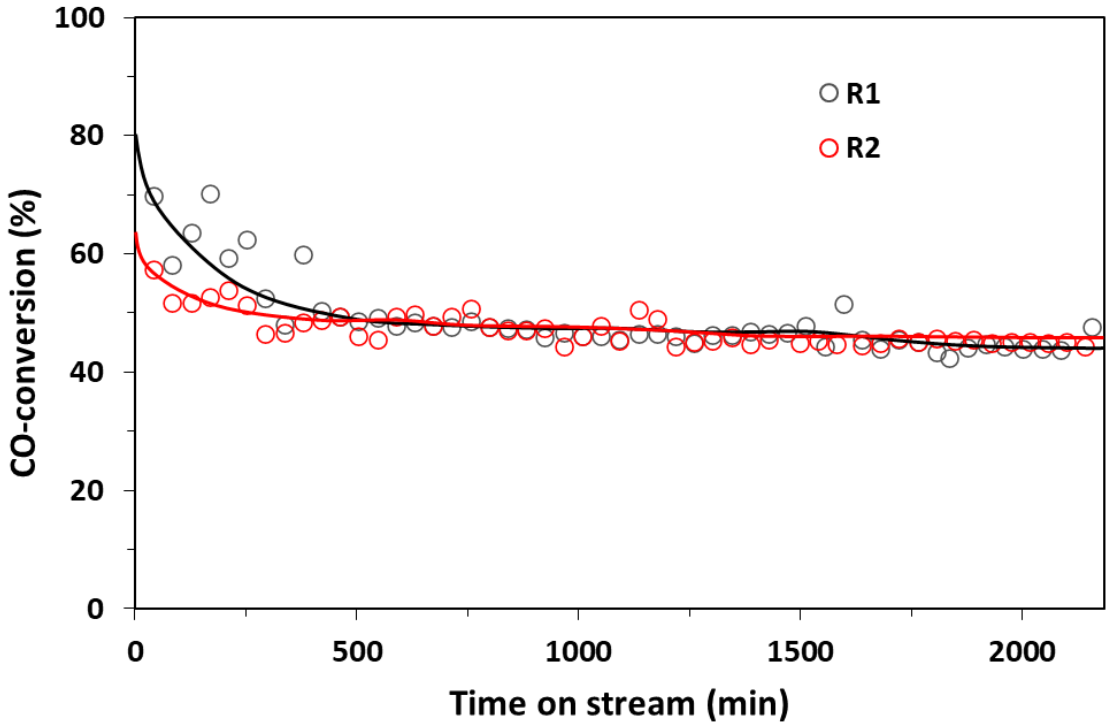

Figure 4.16: CO-conversion of the unpromoted cobalt supported on silica (Mn0; 0.5 g) at 220 °C, 20 barg, syngas flowrate of 60 ml (NTP)/min, and H_2/CO of 2: R1 (first reaction) and R2 (repeated reaction).

Methane selectivity

Methane (CH_4) is the first product that can be formed in the Fischer-Tropsch synthesis. It is an undesirable product hence a low methane selectivity is desired. Figure 4.17 shows CH_4 selectivity as a function of time for experiment 1 (R1) and repeated experiment (R2). CH_4 selectivity for R1 shows an insignificant change in the first 300 mins. However, with increase in time online, CH_4 selectivity increases until it reaches a pseudo steady state CH_4 selectivity of 7 $\pm$ 0.4 C-%. CH_4 selectivity in the repeated experiment (R2) shows a gradual increase with time from t = 0 until it reaches a pseudo steady state of 5 $\pm$ 0.1 C-%. This suggests that CH_4 selectivity of Co/SiO_2 catalysts ranges from 5-7 C-%.

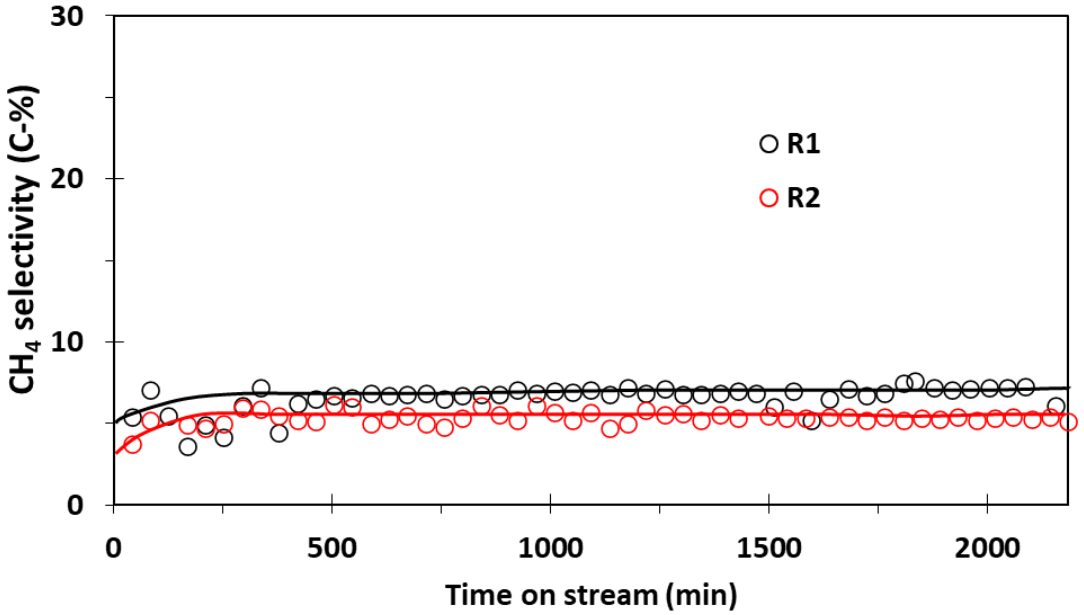

Figure 4.17: CH_4 selectivity of the unpromoted cobalt supported on silica (Mn0; 0.5 g) at 220 °C, 20 barg, syngas flowrate of 60 ml (NTP)/min, and H_2/CO of 2: R1 (experiment 1) and R2 (repeated experiment).

CO_2 selectivity

The CO_2 formed on the unpromoted catalyst is as a result of CO disproportionation reaction which leads to the formation of C surface species and CO_2. It can also be formed by dissociation of CO on the cobalt catalyst surface, followed by recombination of surface C and O species. Figure 4.18 shows the CO_2 selectivity as a function of time for experiment 1 (R1) and repeated experiment (R2). It should be noted that the two curves approach each other from different directions. This may be ascribed to variations in settling down of the catalyst at the beginning of the experiment. The CO_2 selectivity is low in both experiments. In experiment R1, the CO_2 selectivity shows a decrease in the first 400 mins. The CO_2 selectivity reaches a pseudo steady state of 0.43 ± 0.04 C-%. R2 only shows a gradual increase in the CO_2 selectivity reaching a pseudo steady state of 0.30 ± 0.05 C-%.

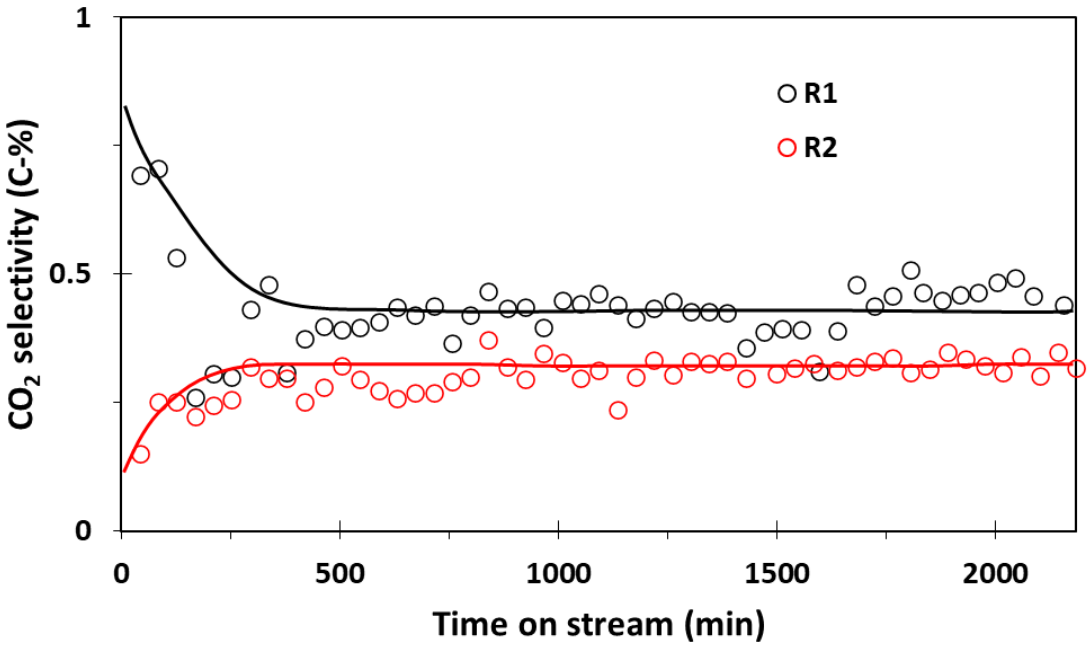

Figure 4.18: CO_2 selectivity of the unpromoted cobalt supported on silica (Mn0; 0.5 g) at 220 °C, 20 barg, syngas flowrate of 60 ml (NTP)/min, and H_2/CO of 2: R1 (experiment 1) and R2 (repeated experiment).

Fischer-Tropsch selectivity

The C_1 to C_n hydrocarbons produced in R1 and R2 were analysed using an offline GC-FID. Table 4.9 shows the Fischer-Tropsch product spectrum for both experiments. Despite the similar activities obtained in experiment R1 and R2, the hydrocarbon distribution shows a larger variation. This suggests that CH_4, C_{2-4} and C_{5+} selectivities for unpromoted catalysts ranges from 5-7 C-%, 5-8 C-% and 84-89 C-%, respectively.

Table 4.9: Performance of unpromoted cobalt catalyst: Mn0 at steady state under Fischer-Tropsch conditions.

Experiment	Selectivity (C-%)			
	CH_4	C_{2-4}	C_{5+}	CO_2
R1	7	8	84	0.43 ± 0.04
R2	5	5	89	0.30 ± 0.05

Statistical analysis

A statistical t-test was performed at pseudo steady state to check if there is any significant differences in the data presented. The sample t-stat value for the CO-conversion as a function of time was found to be 0.62. This value is less than the t-critical two tail value of 2.0, which suggests that there is insignificant differences between the two sets of data. This resulted in a p-value (0.27) that is more than the significance level of 0.05, which validates the fact that there is no significant difference between the two sets of data.

CH_4 selectivity in the two runs are statistically different. The sample t-stat value (17) at pseudo steady state was greater than the t-critical two tail value (2.0). This resulted in a p-value that is less than the significance level of 0.05, suggesting that the two runs are significantly different. CH_4 selectivity obtained with cobalt-based catalysts is strongly dependent on the reaction temperature and the H_2/CO ratio (Claeys & van Steen, 2004). Small variations in either of these parameters may affect CH_4 selectivity strongly. The difference in CH_4 selectivity implies that a variation in the CH_4 selectivity of less than 2 C-% cannot be attributed to the variations in the catalyst composition as it may also be a consequence of slight variations in either the reactor temperature or the H_2/CO ratio.

The selectivity of CO_2 in the two runs are also statistically different. The sample t-stat value (16) at pseudo steady state was greater than the t-critical two tail value (2.0). This resulted in a p-value that is less than the significance level of 0.05, indicating that the two runs are substantially different. The selectivity of CO_2 produced by cobalt-based catalysts is strongly influenced by the reaction temperature and the H_2/CO ratio (Claeys & van Steen, 2004) and even minor changes in either of these parameters can have a significant impact on CO_2 selectivity. The disparity in the CO_2 selectivity means that a variance in the CO_2 selectivity of less than 0.1 C-% cannot be due to catalyst composition changes because it may also be a result of small changes in reactor temperature or H_2/CO ratio.

4.9.1.2 Activity

CO-conversion as a function of time on stream for the five Mn^{SEA}-Co/SiO_2 is shown in Figure 4.19. There is some scatter in the data, but the effect of the manganese loading on the catalyst activity can be clearly seen and is summarized in Table 4.10. The scatter in the data is more pronounced when operating at higher conversion (especially with the catalysts $Mn16^{SEA}$ and $Mn26^{SEA}$). The scatter is thought to originate from a fluctuation in the flow rate of reactor effluent, which would be aggravated by some wax deposits on the needle valve (BV-09). A fluctuating reactor effluent flow rate to which

a constant reference gas stream is added, would result in fluctuating determination of CO-conversion. Hence, more severe fluctuations might be expected upon increasing the yield of liquid hydrocarbons (e.g. by achieving a higher conversion).

The CO-conversion of the unpromoted catalyst has been described above (see section 4.9.1.1). For sample $Mn16^{SEA}$, there is a gradual decrease in CO-conversion up to a time online of ca. 900 mins, after which it starts to stabilize to a CO-conversion of 65 $\pm$ 3%. The CO-conversion obtained with sample $Mn26^{SEA}$ also shows a gradual decrease with time on stream and it starts to stabilize after ca. 700 mins at a CO-conversion of 54 $\pm$ 3%. The CO-conversion obtained with sample $Mn42^{SEA}$ stabilizes at a conversion of 38 $\pm$ 1% after also showing an initial decline in the activity for the first 1000 mins. Finally, sample $Mn55^{SEA}$ shows a similar trend, however, the CO-conversion decreases with time up to ca. 500 mins where it starts to stabilize at a CO-conversion of 39 $\pm$ 1%.

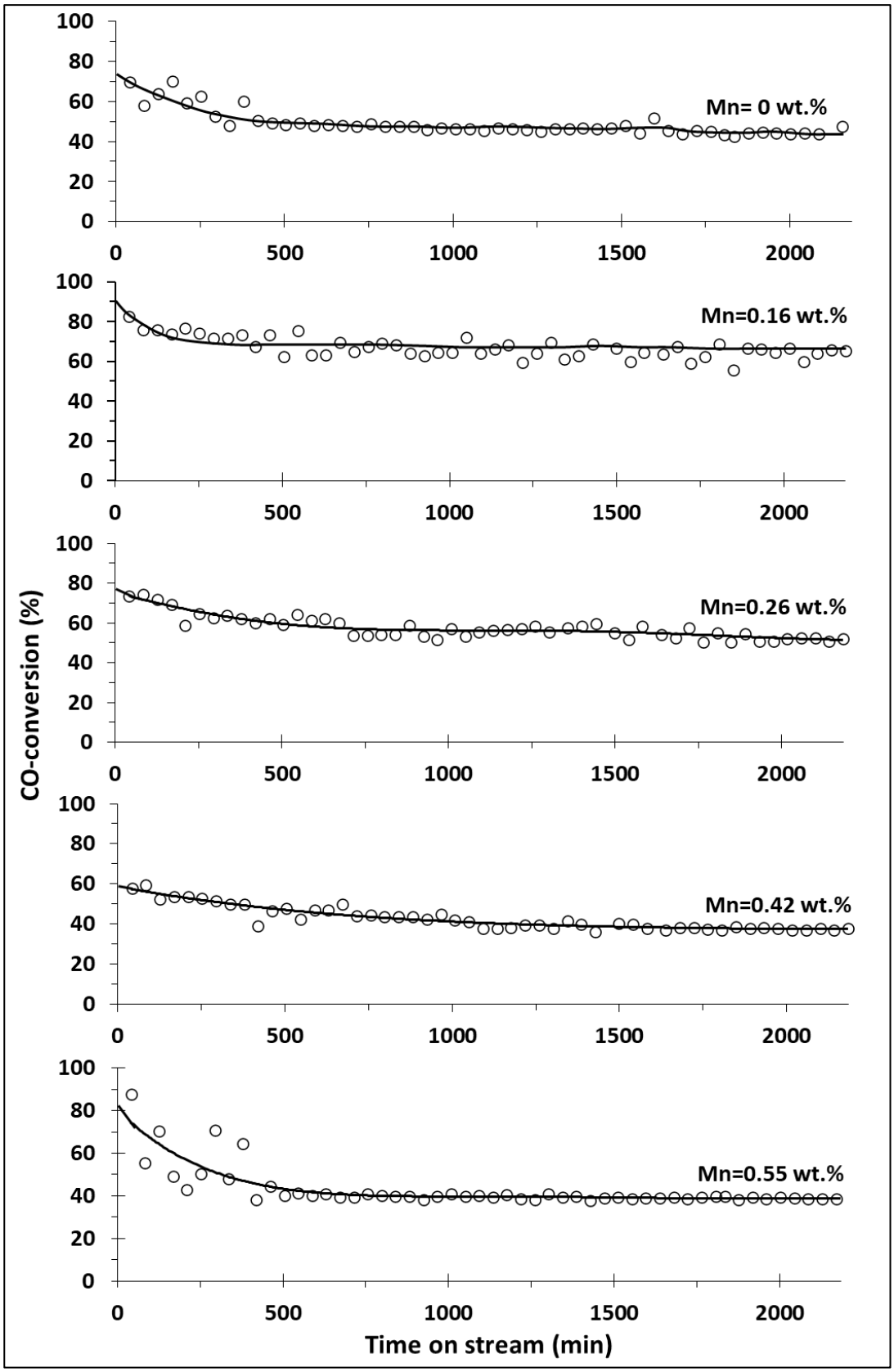

Figure 4.19: Time-dependency of CO-conversion obtained over Mn-Co/SiO_2 at 220 °C, 20 barg, syngas flowrate of 60 ml (NTP)/min, and H_2/CO of 2. (a) Mn0, (b) $Mn16^{SEA}$, (c) $Mn26^{SEA}$, (d) $Mn42^{SEA}$ and (e) $Mn55^{SEA}$.

4.9.1.3 Selectivity in the Fischer-Tropsch synthesis

Methane selectivity

Methane (CH_4) is the first product that can be formed in Fischer-Tropsch, but it is considered an undesirable product hence it is imperative to determine CH_4 selectivity. CH_4 selectivity as a function of time on stream for the five Mn^{SEA}-Co/SiO_2 catalysts is shown in Figure 4.20. CH_4 selectivity of the unpromoted catalyst has been described above (see section 4.9.1.1). CH_4 selectivity as a function of time online obtained with sample $Mn16^{SEA}$ passes a maximum after ca. 500 mins, after which it gradually decreases with time until it reaches a pseudo-stable state of 4 $\pm$ 0.5 C-%. The decrease of CH_4 methane selectivity observed after 750 mins is ascribed to a possibility of small variation in either H_2/CO ratio or reaction temperature which may affect CH_4 selectivity strongly (Claeys & van Steen, 2004). CH_4 selectivity obtained with sample $Mn26^{SEA}$ increases with time online and reaches pseudo steady state of 6 $\pm$ 0.6 C-%. CH_4 selectivity as a function of time online with sample $Mn42^{SEA}$ shows a similar behaviour reaching a pseudo steady state of 5 $\pm$ 0.5 C-%. The same trend is observed with sample $Mn55^{SEA}$, but it reaches a pseudo steady state of 8 $\pm$ 0.3 C-%. Generally, CH_4 selectivity of the samples ranges from 4-8 C-%. From section 4.4, CH_4 selectivities of the unpromoted and promoted cobalt catalysts fall within the same range of 4 C-% and 8 C-%. This suggests that the incorporation of manganese did not significantly alter CH_4 selectivity. A summary of the obtained CH_4 selectivity for the unpromoted and Mn-Co/SiO_2 catalysts prepared using strong electrostatic adsorption (SEA) is shown in Table 4.10.

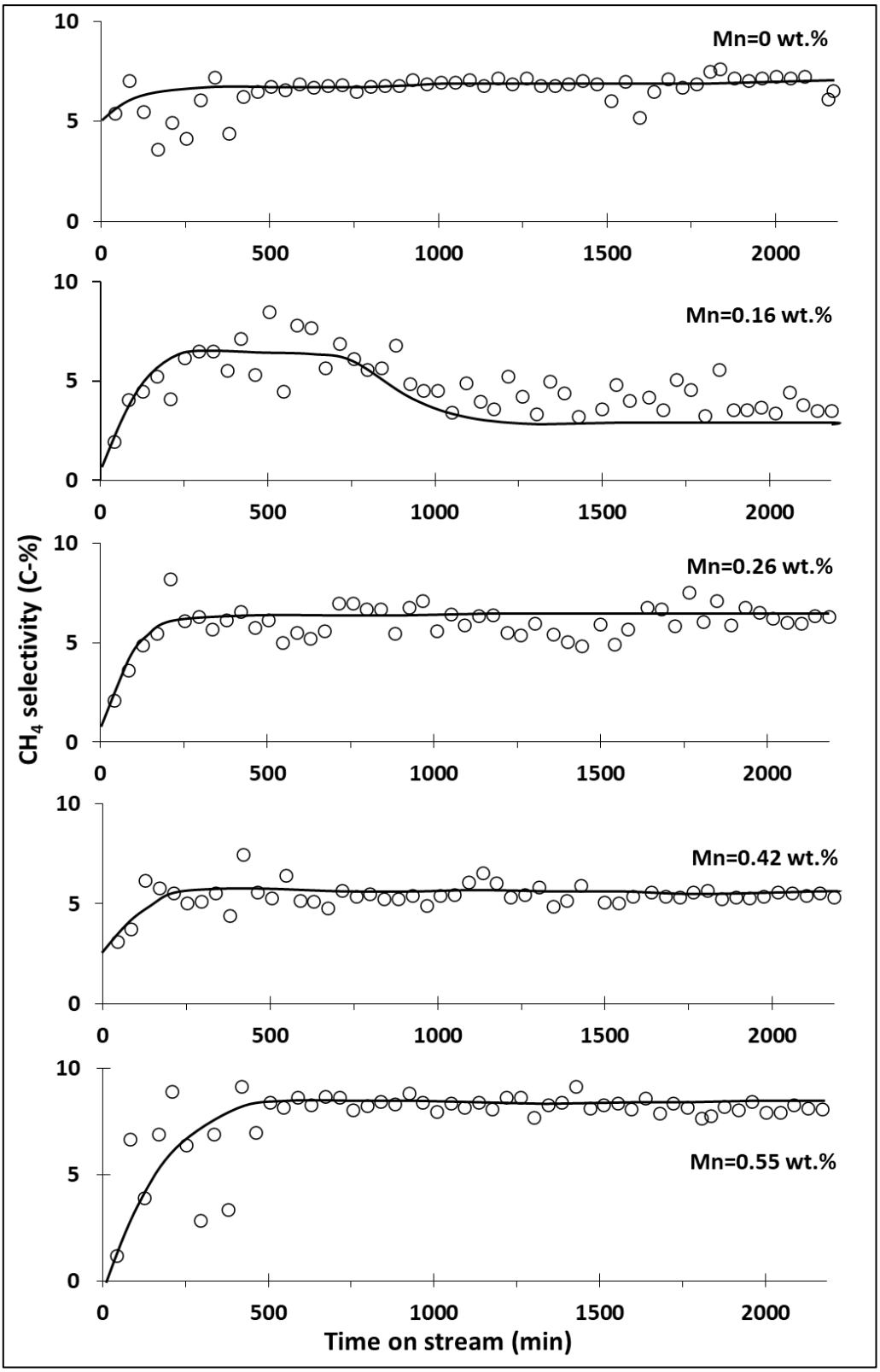

Figure 4.20: Time-dependency of CH_4 selectivity obtained over Mn^{SEA}-Co/SiO_2 catalysts ((a) Mn0, (b) $Mn16^{SEA}$, (c) $Mn26^{SEA}$, (d) $Mn42^{SEA}$ and (e) $Mn55^{SEA}$) at 220 °C, 20 barg, syngas flowrate of 60 ml (NTP)/min, and H_2/CO of 2.

Carbon dioxide selectivity

CO_2 can be formed from CO disproportionation resulting in the formation of C surface species and CO_2. It can also be formed by dissociation of CO on the cobalt catalyst surface followed by recombination of C and O species. The CO_2 selectivity of the unpromoted catalyst has been described above (see section 4.9.1.1). CO_2 selectivity as a function of time on stream for the five Mn^{SEA}-Co/SiO_2 catalysts is shown in Figure 4.21. It is evident that the Mn^{SEA}-Co/SiO_2 catalysts did not produce a lot of CO_2 and the highest CO_2 selectivity was less than 1 C-%. Overall, the CO_2 selectivity decreased with time for all the samples. CO_2 selectivity obtained over Mn0 at steady state is 0.43 $\pm$ 0.04 C-%. The addition of 0.16 wt.% Mn (sample $Mn16^{SEA}$) increased CO_2 selectivity to 0.6 $\pm$ 0.1 C-% relative to the unpromoted catalyst. This may be attributed to the increase in activity as seen from section 4.9.1.2. A further increase in manganese content decreased CO_2 selectivity to 0 C-%. A summary of the pseudo steady state CO_2 selectivity obtained over the various Mn^{SEA}-Co/SiO_2 catalysts is shown in Table 4.10.

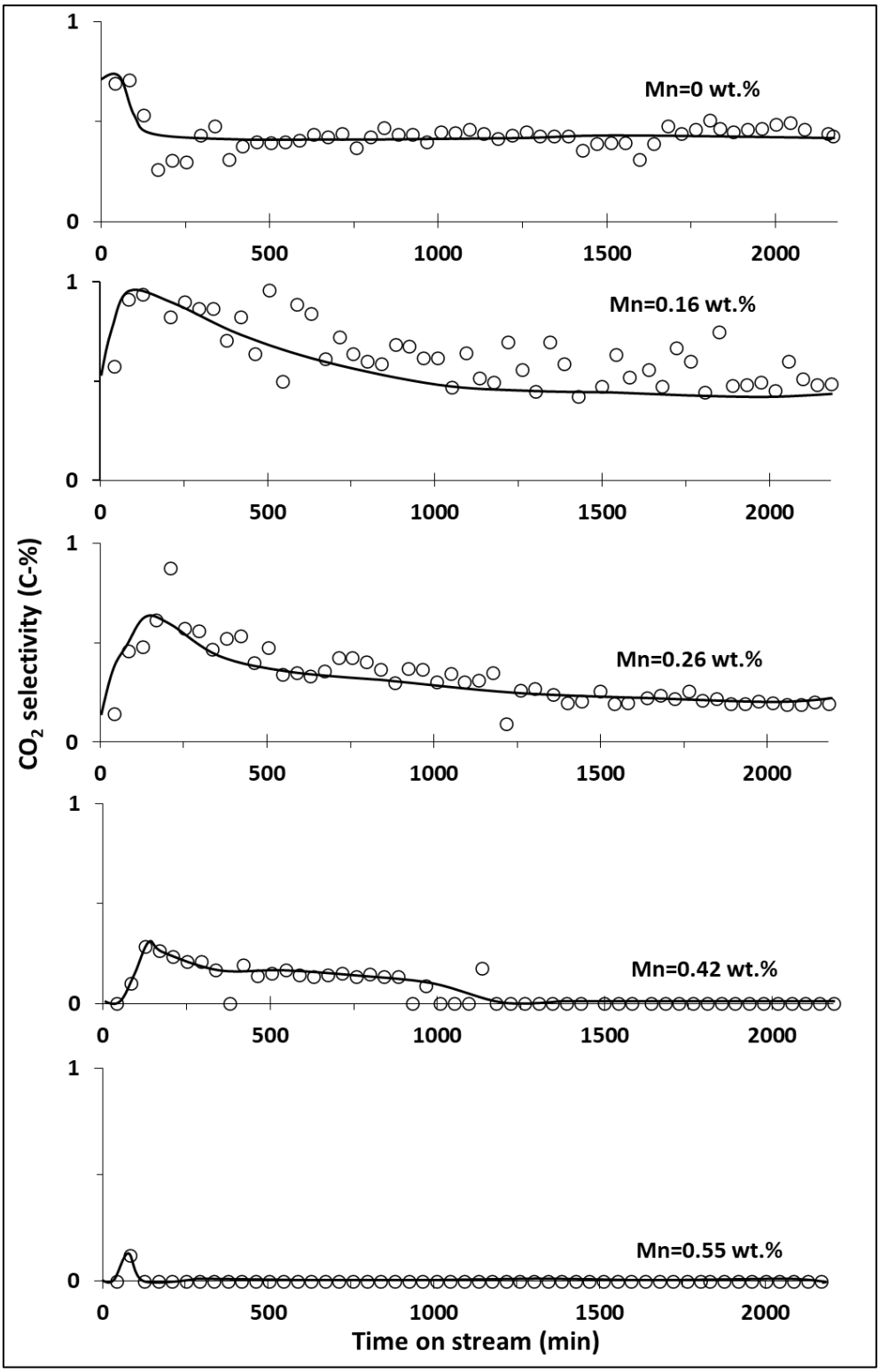

Figure 4.21: Time-dependency of CO_2 selectivity obtained over Mn^{SEA}-Co/SiO_2 ((a) Mn0, (b) $Mn16^{SEA}$, (c) $Mn26^{SEA}$, (d) $Mn42^{SEA}$ and (e) $Mn55^{SEA}$) catalysts prepared using strong electrostatic adsorption (SEA) in the Fischer-Tropsch synthesis at 220 °C, 20 barg, syngas flowrate of 60 ml (NTP)/min, and H_2/CO of 2.

4.9.1.4 Formation of hydrocarbons in the Fischer-Tropsch synthesis

Good catalyst selectivity is imperative. The selectivity of unpromoted and manganese promoted cobalt catalysts towards hydrocarbons was determined using an offline GC-FID. The chain growth probability (α value) is one of the most significant parameters in Fischer-Tropsch synthesis. It is a measure of the probability in which a molecule would react to form longer chains. To investigate the chain growth probability, the Anderson-Schulz-Flory (ASF) distribution was plotted for each catalyst.

The ASF distribution for Mn^{SEA}-Co/SiO_2 catalysts are shown in Figure 4.22. Generally, the ASF plot gives a straight line (Puskas, 1993; Schulz *et al.,* 1999; Puskas & Hurlbut, 2003), however, the ASF plots in Figure 4.22 show deviations from the ideal ASF. All ASF plots have relatively high CH_4 content. The high CH_4 content has been explained by an increased surface mobility of the CH_4 precursor and by the different reaction mechanisms for methanation and chain growth (Ponec,1978). The low C_2 content is due to an increased re-adsorption rate of chain initiation and growth (Schulz *et al.*,1999). From C_3 to C_7, the ASF plot shows an expected linear behaviour in a semi-logarithmic plot. It should be noted that the slope in this region is often not constant and may increase with increasing carbon number e.g. as a consequence of re-incorporation of reactive product compounds (e.g. olefins; Schulz et al., 1999). From C_8 onwards, a drop in molar content is observed due to the solubility and retainment of the products in the liquid wax phase. The chain growth probability was determined from the molar content in the fraction C_5 to C_7. The chain growth probability for each sample is shown in Table 4.10. The limit chain growth probability, obtained at high carbon numbers, could however not be obtained and the reported values can thus only be taken as an indication of the chain growth probability obtained.

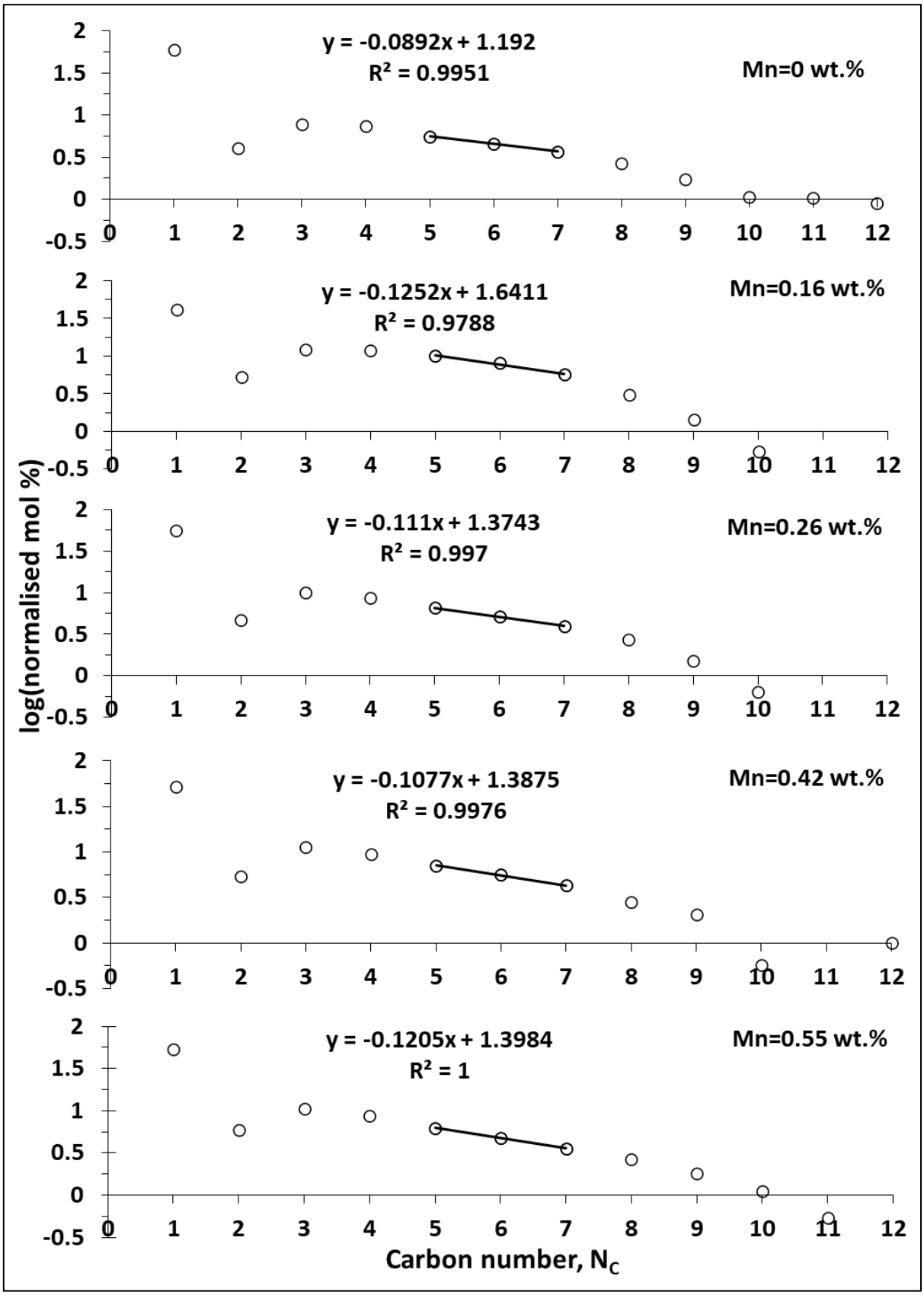

Figure 4.22: The ASF plots obtained over Mn-Co/SiO_2 catalysts: (a) Mn0, (b) $Mn16^{SEA}$, (c) $Mn26^{SEA}$, (d) $Mn42^{SEA}$ and (e) $Mn55^{SEA}$.

Table 4.10: Summary of CO-conversion and selectivities of Mn^{SEA}-Co/SiO_2 catalysts at steady state under Fischer-Tropsch conditions.

Catalyst	CO-conversion(%)	CH_4 selectivity (C-%)	C_{5+} selectivity (C-%)	CO_2 selectivity (C-%)	α (C_{5-7})
Mn0	46 ± 2	7 ± 0.4	84	0.43 ± 0.04	0.81
$Mn16^{SEA}$	65 ± 3	4 ± 0.5	87	0.6 ± 0.1	0.75
$Mn26^{SEA}$	54 ± 3	6 ± 0.6	86	0.3 ± 0.1	0.77
$Mn42^{SEA}$	38 ± 1	5 ± 0.5	86	0	0.78
$Mn55^{SEA}$	39 ± 1	8 ± 0.3	80	0	0.76

Total Olefin content

The effect of manganese on total olefin content in the fraction of linear hydrocarbons was investigated, as shown in Figure 4.23. The graph shows total olefin content from C_2 to C_9. The total olefin content decreases with increasing carbon number from C_3 onwards. There is an anomaly in the C_2 content; the lower total olefin content in the fraction of C_2-hydrocarbons has been ascribed to the fast re-incorporation of ethene into the growing chains (Claeys & van Steen, 2004).

The total olefin content in the fraction of linear hydrocarbons is the lowest with sample $Mn16^{SEA}$, compared to the unpromoted catalyst. This suggests that more paraffins were formed. This may be a result of the effect of manganese or a consequence of the differences in CO-conversion. However, a further increase of manganese content increased the total olefin, suggesting that more olefins were formed relative to paraffins. Similar results were obtained by Morales *et al.* (2007) and Bezemer *et al.* (2006) where the selectivities of the catalysts were obtained at the same CO-conversion, and this was achieved by modifying the space velocity. Thus, the change in olefin content was as a result of manganese promotion.

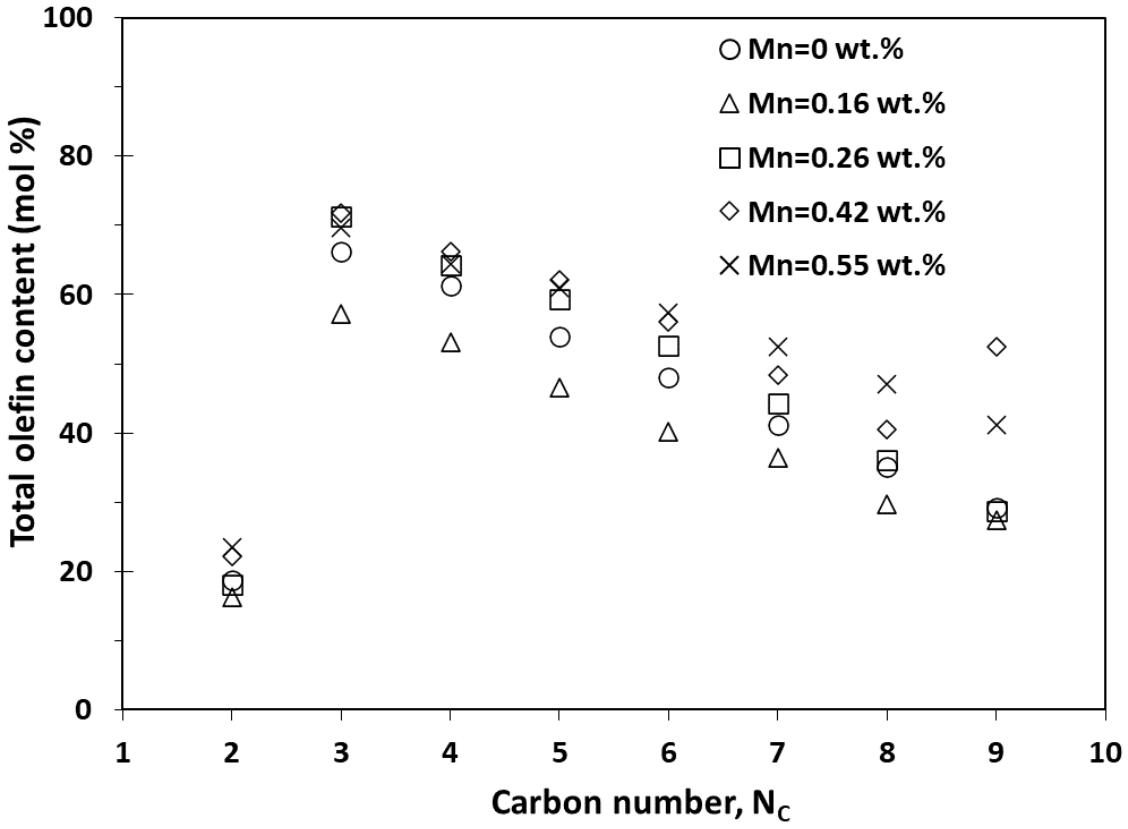

Figure 4.23: Total olefin content in the fraction of linear hydrocarbons as a function of carbon number for Mn-Co/SiO_2 catalysts prepared using strong electrostatic adsorption (SEA).

1-olefin content

The 1-olefin content in the fraction of linear olefins obtained over the Mn^{SEA}-Co/SiO_2 catalysts was also investigated. The 1-olefin content as a function of carbon number is shown in Figure 4.24. It should be noted that the 1-olefin content was analysed from C_4 because that is the first carbon number at which trans-2-olefins and cis-2-olefins can exist. The analysis was done up to C_9. This is because at this carbon number the trans-2-olefins start to co-elute with the n-paraffin of the same carbon number, thus making it difficult to accurately determine the n-olefin content and the 1-olefin content. The 1-olefin content decreased with increasing carbon number for all Mn^{SEA}-Co/SiO_2 catalysts prepared using SEA. A similar trend was observed by Claeys & van Steen, (2004) and it was ascribed to secondary double bond isomerisation, which is favoured due to the increased concentration of the 1-olefins in the wax surrounding the catalyst particles. The 1-olefin content was the lowest with sample $Mn16^{SEA}$, when compared to the unpromoted catalyst. This may be associated with the differences in CO-

conversion and/or the effect of manganese. However, a further increase in manganese concentration resulted in increased 1-olefin content.

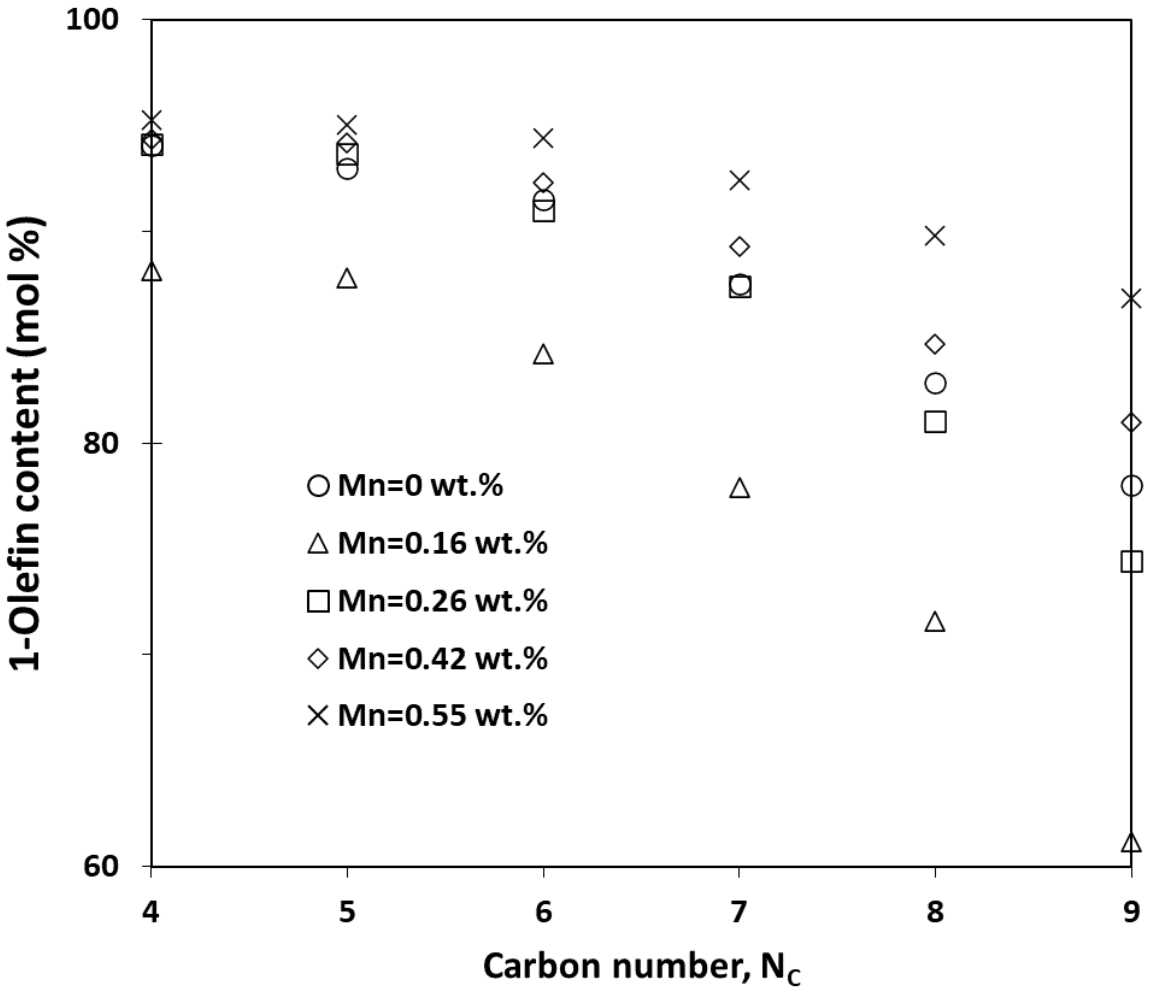

Figure 4.24: 1-olefin content in the fraction of linear olefins as a function of carbon number for Mn-Co/SiO_2 catalysts prepared using strong electrostatic adsorption (SEA).

4.10 Performance of Mn-promoted Co/SiO_2 prepared by impregnation

The precursor used for the adsorption of manganese on Co_3O_4/SiO_2 using strong electrostatic adsorption (SEA) in this study is $KMnO_4$. The second batch of $Mn\text{-}Co/SiO_2$ was prepared by wet impregnation (IMPR) of manganese(II) acetate tetrahydrate on Co_3O_4/SiO_2 (without pH adjustments). This resulted in manganese weight loadings of 0.16 wt.% and 0.26 wt.%. This allowed comparisons of the two preparation methods on the performance of the catalysts.

The two catalysts were subjected to H_2 chemisorption measurements. As it will be seen in the discussion section (section 5), the aim was to quantify the amount of H_2 uptake in order to determine the turnover frequency of the manganese promoted Co/SiO_2 catalysts prepared by IMPR. Using equation 4.1, the H_2 uptake of the catalysts is shown in Table 4.11.

Table 4.11: H_2 uptake from H_2 chemisorption measurements for $Mn\text{-}Co/SiO_2$ catalysts prepared by IMPR (catalysts reduced at 350 °C for 4 hrs in pure H_2).

Catalyst	H_2-uptake (mmol/g)
$Mn16^{IMPR}$	0.127
$Mn26^{IMPR}$	0.123

Fischer-Tropsch synthesis for the two catalysts was carried out at T = 220 °C, P = 20 barg and an H_2/CO ratio of 2. Figure 4.25 shows CO and H_2 flowrate for each reaction with respect to time.

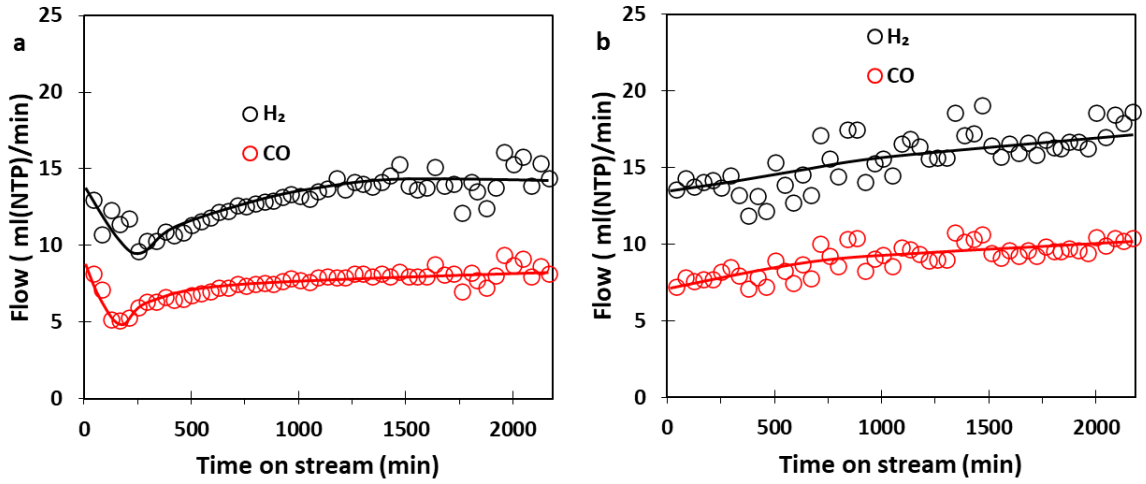

Figure 4.25: H_2 and CO flowrate with respect to time for Mn^{IMPR}-Co/SiO_2 catalysts prepared by impregnating manganese(II) acetate tetrahydrate on pre-formed Co_3O_4/SiO_2 with no pH adjustments: (a) $Mn16^{IMPR}$ and (b) $Mn26^{IMPR}$ at 220 °C, 20 barg and an H_2/CO ratio of 2 and syngas flowrate of 60 ml (NTP)/min.

Table 4.12: Reactions carried out at T = 220 °C, P = 20 barg and H_2/CO = 2 with 0.5 g of each Mn^{IMPR}-Co/SiO_2 catalyst loaded in a fixed bed reactor.

Catalyst	H_2 flowrate (ml (NTP)/min)	CO flowrate (ml (NTP)/min)
$Mn16^{IMPR}$	14 ±1.1	8.2 ±0.59
$Mn26^{IMPR}$	17 ±1.1	9.7 ±0.56

4.10.1.1 Activity

The conversion of CO as a function of time on stream obtained with the catalysts $Mn16^{SEA}$ and $Mn26^{IMPR}$ (each with a Mn loading of 0.16 wt.% and 0.26 wt.%), is shown in Figure 4.26. CO-conversion obtained with $Mn16^{SEA}$ and $Mn26^{SEA}$ catalysts has been described in section 4.9.1.2.

The conversion of CO as a function of time online obtained over $Mn16^{IMPR}$ increases gradually in the first 200 mins (see Figure 4.26). It then decreases gradually with time until it reaches a pseudo steady state of 62 ± 1%. The pseudo steady state CO-conversion obtained over $Mn16^{IMPR}$ is slightly lower than the pseudo steady state CO-conversion obtained over $Mn16^{SEA}$ (65 ± 3%).

The conversion of CO for $Mn26^{IMPR}$ gradually decreases in the first 700 mins (see Figure 4.26). Thereafter, the CO-conversion reaches a pseudo steady state level of 54

± 3%, which is consistent with the CO-conversion obtained over $Mn26^{SEA}$ (CO-conversion = 54 ± 3 %).

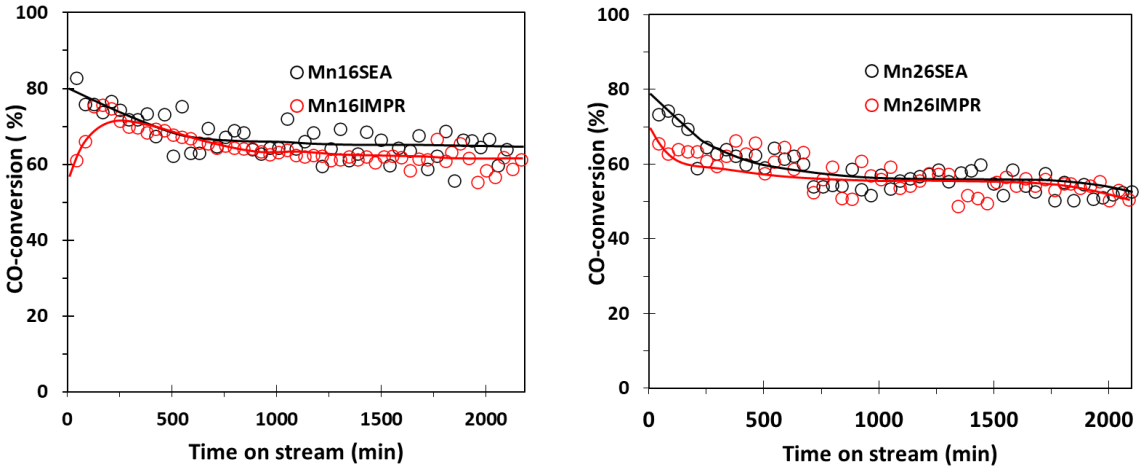

Figure 4.26: Time-dependency of CO-conversion obtained over $Mn16^{SEA}$ and $Mn26^{SEA}$ compared with $Mn16^{IMPR}$ and $Mn26^{IMPR}$ with manganese loading of 0.16 wt.% and 0.26 wt.% respectively at 220 °C, 20 barg, syngas flowrate of 60 ml (NTP)/min and an H_2/CO of 2.

4.10.1.2 Product selectivity in the Fischer-Tropsch synthesis

Methane selectivity

Figure 4.27 shows the CH_4 selectivity in the Fischer-Tropsch synthesis obtained over $Mn16^{IMPR}$ and $Mn26^{IMPR}$ as a function of time on stream. CH_4 selectivity obtained with $Mn16^{IMPR}$ increases up to ca. 400 mins online and gradually stabilizes at a value of 5 ± 0.4 C-%. CH_4 selectivity obtained with $Mn26^{IMPR}$ increases up to ca. 400 mins, and gradually stabilizes with time until it reaches a pseudo steady state of 6 ± 0.1 C-%.

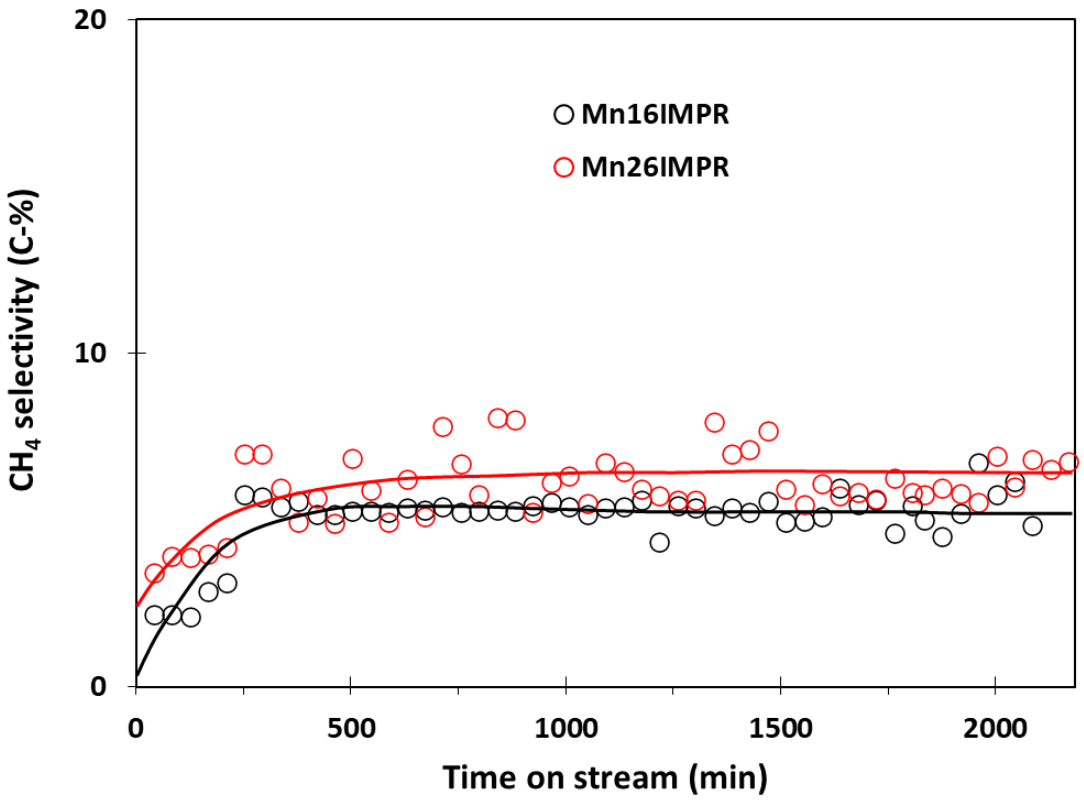

Figure 4.27: Time-dependency of CH_4 selectivity obtained over $Mn16^{IMPR}$ and $Mn26^{IMPR}$ at 220 °C, 20 barg, syngas flowrate of 60 ml (NTP)/min and H_2/CO of 2.

Carbon dioxide selectivity

CO_2 selectivities obtained in the Fischer-Tropsch synthesis over $Mn16^{IMPR}$ and $Mn26^{IMPR}$ are presented in Figure 4.28. The initial CO_2 selectivity obtained with $Mn16^{IMPR}$ shows a bit of scattered data. CO_2 selectivity then decreases gradually with time until it reaches a pseudo steady state of 0.27 $\pm$ 0.03 C-%, which is less than the CO_2 selectivity of $Mn16^{SEA}$ (CO_2 selectivity = 0.6 $\pm$ 0.1 C-%). CO_2 selectivity of $Mn26^{IMPR}$ decreases with time until it reaches a pseudo steady state of 0.4 $\pm$ 0.1 C-%, which is slightly more than CO_2 selectivity of $Mn26^{SEA}$ (0.3 $\pm$ 0.1 C-%).

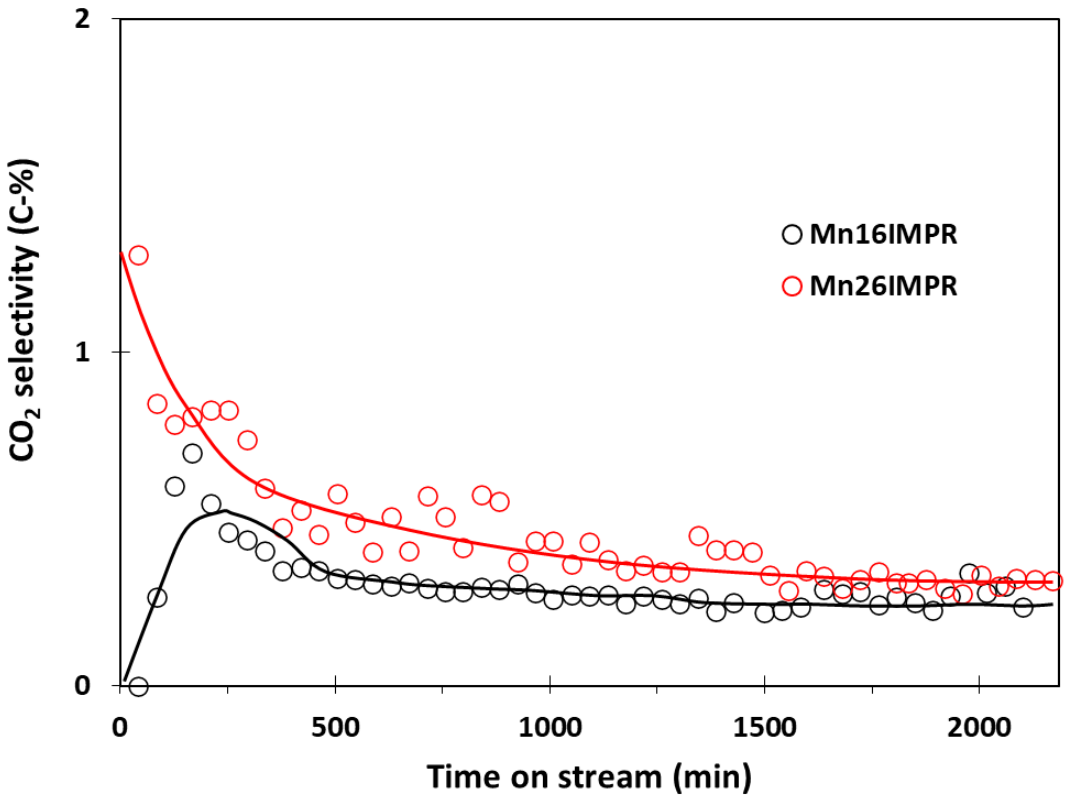

Figure 4.28: Time-dependency of CO_2 selectivity over $Mn16^{IMPR}$ and $Mn26^{IMPR}$ in the Fischer-Tropsch synthesis at 220 °C, 20 barg, syngas flowrate of 60 ml (NTP)/min, and an H_2/CO of 2.

ASF plots for the catalysts prepared using IMPR with manganese loadings of 0.16 wt.% and 0.26 wt.% are shown in Figure 4.29. From these plots, the chain growth probability was determined and is summarized in Table 4.13 below.

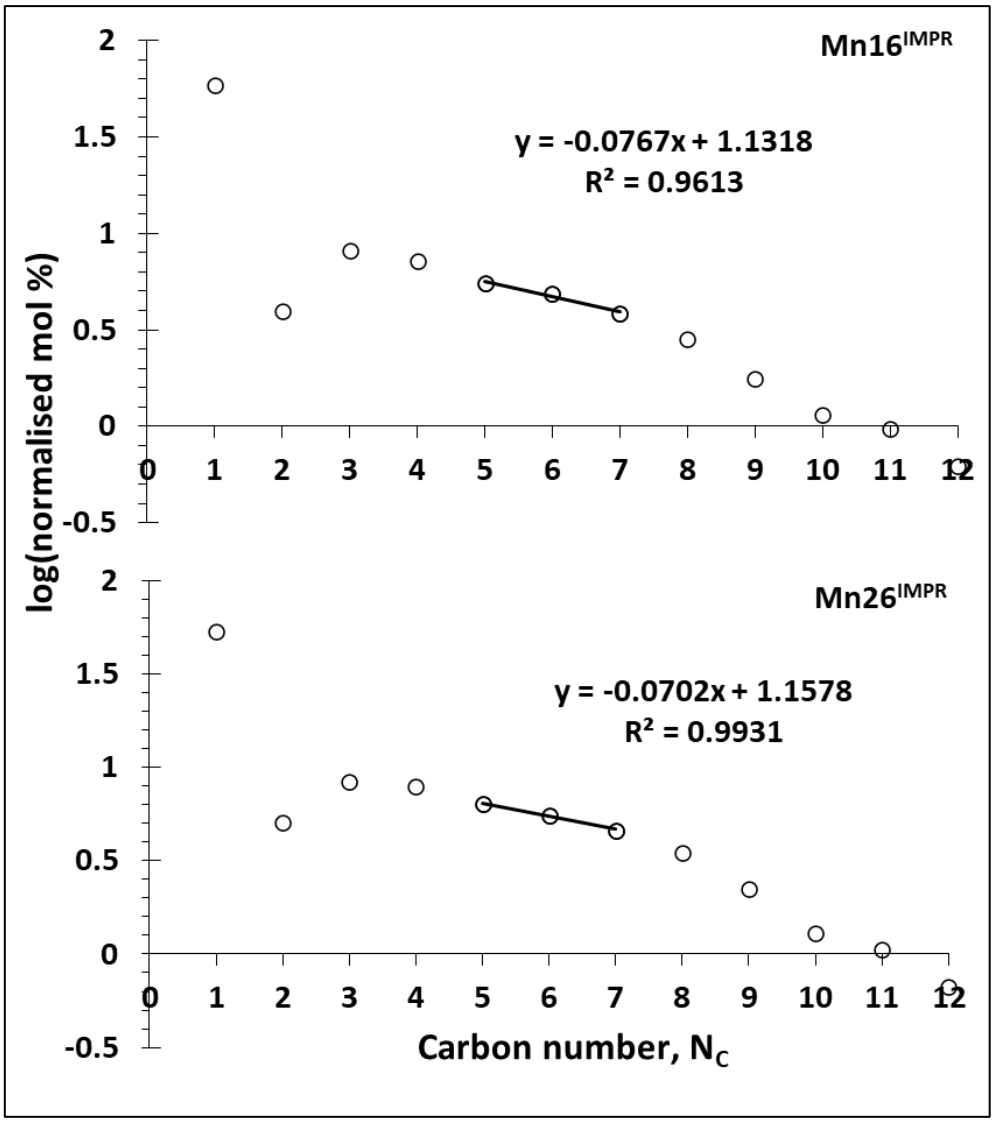

Figure 4.29: ASF plots obtained with $Mn16^{IMPR}$ and $Mn26^{IMPR}$.

Table 4.13: Comparison of the pseudo steady state catalytic activity obtained with manganese promoted cobalt-based Fischer-Tropsch catalysts prepared via IMPR.

Catalyst	CO-conversion (%)	CH_4 selectivity (C-%)	C_{5+} Selectivity (C-%)	CO_2 selectivity (C-%)	α (C_{5-7})
$Mn16^{IMPR}$	62 ± 1%.	5.0 ± 0.4 C-%.	89	0.27 ± 0.031	0.84
$Mn26^{IMPR}$	54 ± 3%.	6.0 ± 0.1 C-%.	85	0.4 ± 0.1 .	0.85

5 DISCUSSION

Manganese is known to have both structural and electronic effects on cobalt-based Fischer-Tropsch catalysts (Morales *et al.,* 2005; Morales *et al.,* 2007). The effects of manganese promotion on cobalt-based Fischer-Tropsch catalysts have been well documented (Bezemer *et al.,* 2006; Dinse *et al.,* 2012; Tang *et al.,* 2013; Johnson *et al.,* 2015). However, the way in which the activity and selectivity are influenced is not well understood. It has been hypothesized that the enhanced activity and selectivity in manganese promoted cobalt-based catalysts are due to the manganese in its oxide state serving as a Lewis acid that weakens the C-O bond and thus facilitating CO dissociation. It is then assumed that O formed upon CO dissociation is easily removed in the form of H_2O or CO_2 (van Santen *et al.,* 2013). Raub *et al.* (2021) observed a delay in the formation of oxygenated species in their steady state isotopic transient kinetic analysis (SSITKA) experiments over manganese promoted cobalt-based catalysts. This suggested that the O removal, generated upon CO dissociation, is the limiting step.

Feltes *et al.* (2010) speculated that the preparation of Mn-Co/TiO_2 catalysts via strong electrostatic adsorption (SEA) of potassium permanganate in a solution of pH = 1 for 1 hr resulted in placing manganese in close proximity to cobalt with increased adsorption strength that is not possible with impregnation (IMPR, without pH adjustments), resulting in more active catalyst. The question that arose was whether or not the potassium in potassium permanganate source interacts with the cobalt/silica catalyst precursor and contributes towards enhanced activity.

The aim of this study was to investigate the effect of manganese selectively adsorbed on cobalt catalyst via SEA (using potassium permanganate as a source of manganese) on activity and selectivity of Co/SiO_2, with a focus on its role in CO adsorption. In addition, IMPR of manganese(II) acetate tetrahydrate on pre-formed Co/SiO_2, without pH adjustments was also examined. This was done to compare the catalytic performances of the two batches of catalysts prepared using two different manganese precursors, with the assumption that potassium in the potassium permanganate precursor could play a role in the catalytic activity.

5.1 Effect of Mn promotion on Co particle size distribution

The average cluster sizes measured from TEM images (Figure 4.3) show that the addition of manganese of different concentrations to the unpromoted cobalt catalysts does not significantly affect the cluster sizes or shapes of pre-formed cobalt particles. The mean particle sizes of cobalt, obtained from H_2 chemisorption measurements, for all Mn^{SEA}-Co/SiO_2 samples were approximately 13 nm, in close agreement with the

Co_3O_4 crystallite domain size obtained from PXRD of approximately 14 nm implying some particle growth during the reduction process. This suggests that the incorporation of manganese into pre-formed cobalt particles, dispersed on silica support, did not induce any significant changes in particle size or shape. It is thus unlikely that the changes in activities (as it will be seen later) are due to the particle size distribution or shape effects. It has been reported that cobalt particles with average sizes greater than 8 nm display insignificant effects on the turnover frequency of the cobalt catalysts (Bezemer *et al.,* 2006).

5.2 Effect of Mn on reducibility of Co

The observed manganese effect on the H_2-TPR profiles of Mn^{SEA}-Co/SiO_2, i.e narrowing effect of the broad peak in the second stage of reduction, could possibly be ascribed to the reduction of the permanganate anion (MnO_4^-) to MnO and re-distribution of cobalt atoms, making it easier to reduce them. This is in line with TGA findings, which indicate that manganese promotion makes it easier to reduce cobalt. As it will be seen later, this may be the explanation for the enhanced activity.

5.3 Effect of Mn promotion on CO and H_2 adsorption

H_2 chemisorption measurements show a decrease in H_2 uptake upon addition of manganese to the unpromoted cobalt catalyst. This was also observed in the pulse chemisorption of CO prior to CO-TPD. The decrease in CO adsorbed follows this trend: Co/SiO_2 >$Mn16^{SEA}$ >$Mn26^{SEA}$ >$Mn42^{SEA}$ >$Mn55^{SEA}$. This is attributed to the surface blockage of cobalt active sites.

There is no evidence in this study of enhanced CO dissociation on the cobalt surface upon addition of manganese. Previous studies have indicated an enhancement of CO dissociation (Johnson *et al.,* 2015). Moreover, Johnson *et al.* (2015) observed an improved strength of CO adsorption on manganese promoted Co/SiO_2 catalysts, with a low temperature peak shifting to higher temperatures. However, the temperature peak shift they observed was in the range of 5-20 °C, which is a rather small shift in the strength of CO adsorption. In this study, there was no evidence of enhanced strength of CO adsorption due to the insignificant shifts in peak positions. This may be ascribed to small amounts of manganese incorporated (<1%) as Johnson *et al.* (2015) carried out a study with higher manganese content (>1%).

The stoichiometry of H_2 and CO adsorption on cobalt was also evaluated. This has been studied previously and H_2 adsorption stoichiometry is 1 H atom per surface cobalt atom. CO adsorption stoichiometry varies from 0.4 to 2.3 moles of CO per surface cobalt atom due to reversible and non-activated CO adsorption (Reuel & Bartholomew,

1984). Table 5.1 summarizes the H_2/CO adsorption stoichiometries for the unpromoted and manganese promoted cobalt-based catalysts. In the absence of lateral interactions, a ratio of 0.5 was expected. However, the samples show a H_2/CO ratio of 2 ± 0.12, which may be ascribed to lateral interactions affecting the adsorption of CO.

Table 5.1: Stoichiometric ratio for the adsorption of H_2 and CO on Mn-Co/SiO_2 catalysts prepared using strong electrostatic adsorption (SEA).

Catalyst	H_2/CO
Mn0	1.80
$Mn16^{SEA}$	2.16
$Mn26^{SEA}$	2.07
$Mn42^{SEA}$	1.98
$Mn55^{SEA}$	2.05

5.4 Effect of manganese on activity

The catalytic performances of Mn^{SEA}-Co/SiO_2 samples at pseudo steady state are summarized in Table 5.2. The addition of manganese via strong electrostatic adsorption (SEA) on cobalt catalyst resulted in improved catalytic performance. Similar findings in enhanced catalytic behaviour have been reported previously by Feltes *et al.* (2010). The cobalt-time-yields of the unpromoted and Mn^{SEA}-promoted Co/SiO_2 catalysts fall within a range of 0.056-0.093 mmol CO/g_{Co}·s. The cobalt-time-yield of unpromoted cobalt catalyst increased from 0.065 ± 0.002 mmol CO/g_{Co}·s to 0.093 ± 0.001 mmol CO/g_{Co}·s when 0.16 wt.% manganese ($Mn16^{SEA}$) was added. A further increase in the manganese content to 0.26 wt.% resulted in a decrease in cobalt-time-yield, from 0.093 ± 0.002 mmol CO/g_{Co}·s to 0.079 ± 0.003 mmol CO/g_{Co}·s. A higher manganese loading resulted in a further decrease in cobalt-time-yield, down to 0.054 ± 0.002 mmol CO/g_{Co}·s. This suggests that a very small amount of manganese enhanced the cobalt-time-yield of the cobalt catalyst.

The turnover frequency can be viewed as a direct measure of the average activity of the available cobalt sites on the surface accounting for the variation in the metal surface area upon manganese addition to the catalyst. Again, it can be seen that the addition of a small amount of manganese increases the turnover frequency from 0.11 s^{-1} to 0.16 s^{-1}. This implies that manganese affects not only the physical properties, but also the intrinsic activity of the cobalt sites.

Table 5.2: Catalytic performances of Mn^{SEA}-Co/SiO_2 catalysts at pseudo steady state obtained with manganese promoted cobalt-based Fischer-Tropsch catalysts.

Catalyst	CO-conversion (%)	Cobalt-time-yield* (mmol CO/g_{Co}. s)	TOF (s^{-1}) **
Mn0	46 ± 2	0.065 ± 0.002	0.11
$Mn16^{SEA}$	65 ± 3	0.093 ± 0.001	0.16
$Mn26^{SEA}$	54 ± 3	0.079 ± 0.003	0.14
$Mn42^{SEA}$	38 ± 1	0.054 ± 0.002	0.11
$Mn55^{SEA}$	39 ± 1	0.056 ± 0.001	0.11

Cobalt-time-yield*=moles of CO converted/g_{Co}/s

TOF**=CO moles converted/moles of H_2 uptake/s

5.5 Effect of manganese on chain growth probability

Table 5.3 summarizes the influence of manganese on Fischer-Tropsch product distribution of the Mn^{SEA}-Co/SiO_2 catalysts. The ultimate parameter of interest is the C_{5+} selectivity. This should correlate with the Anderson-Schulz-Flory (ASF) distribution and thus the change in chain growth probability is expected to increase with increasing C_{5+} selectivity. The chain growth probability, α, ranges from 0.75-0.81 with no trend attributed to the C_{5+} selectivity. A product with an ideal ASF product distribution should yield a semi-logarithmic plot of the molar content as a function of the carbon number, from which the chain growth probability can be estimated from the slope ($\log \alpha$). However, the experimental product distribution for cobalt catalysts deviates from the ideal ASF plot in three various ways: a) the molar selectivity of C_1 is higher than that predicted by the ideal ASF distribution, b) the C_2 selectivity is significantly lower, and c) the chain growth probability increases with increasing carbon number asymptotically reaching a limiting α^{lim} (Claeys & van Steen, 2004). ASF plots in this study display similar deviations as the real ASF plot. However, there is a drop in C_{8+} molar content and this is attributed to the retention of compounds in the liquid wax phase. Thus, the chain growth probability was measured from C_5 to C_7. The chain growth probability determined in the range C_5-C_7 does not correlate with the C_{5+} selectivity. This is because the chain growth probability was determined in a very limited carbon number range.

5.6 Effect of manganese on product selectivity

Methane (CH_4) selectivity of all the catalysts ranges from 4 C-% to 8 C-%. The $Mn16^{SEA}$ catalyst resulted in a decrease in CH_4 selectivity, from 7 C-% to 4 C-%. However, the use of $Mn55^{SEA}$ resulted in higher CH_4 selectivity, up to 8 C-%. The C_{5+} selectivity of the unpromoted cobalt catalyst increased from 84 C-% to 87 C-% with the addition of $Mn16^{SEA}$. The $Mn26^{SEA}$-$Mn55^{SEA}$ catalysts showed decreased C_{5+} selectivity, up to 80 C-%. The effect of manganese on C_{2-4} selectivity was also investigated. The catalysts with small amounts of manganese ($Mn16^{SEA}$-$Mn42^{SEA}$) did not change the C_{2-4} selectivity. However, higher manganese content ($Mn55^{SEA}$) changed the C_{2-4} selectivity of the unpromoted cobalt catalyst from 8 C-% to 12 C-%.

As summarized in Table 5.3, the CH_4 and C_{5+} selectivities of the unpromoted catalyst are 5-7 C-% and 84-89 C-% respectively. The CH_4 and C_{5+} selectivities of the unpromoted cobalt catalyst fall within these ranges (see Table 4.7). This suggests that the changes observed in CH_4 and C_{5+} selectivities are insignificant and this is consistent with the results obtained by Bukur *et al.* (2012). It was observed that there were insignificant changes in Fischer-Tropsch product selectivity in a fixed bed reactor with a CO-conversion of 40-60 %. Previous studies have reported a decrease in CH_4 selectivity and an increase in C_{5+} selectivity on manganese promoted cobalt catalysts (Morales *et al.,* 2005; Morales *et al.,* 2007; Bezemer *et al.,* 2006; Dinse *et al.,* 2012; Johnson *et al.,* 2015).

Table 5.3: Fischer-Tropsch synthesis catalytic performance of Mn^{SEA}-Co/SiO_2 catalysts at 220 °C, 20 barg, syngas flowrate of 60 ml (NTP)/min and H_2/CO ratio of 2, at pseudo steady state.

			Selectivity (C-%)			
Catalyst	X_{CO} (%)	α (C_{5-7})	CH_4	C_{2-4}	C_{5+}	CO_2 (%)
Mn0	46 ± 2	0.81	7 ± 0.4	8	84	0.43 ± 0.04
$Mn16^{SEA}$	65 ± 3	0.75	4 ± 0.5	8	87	0.6 ± 0.1
$Mn26^{SEA}$	54 ± 3	0.77	6 ± 0.6	8	86	0
$Mn42^{SEA}$	38 ± 1	0.78	5 ± 0.5	9	86	0
$Mn55^{SEA}$	39 ± 1	0.76	8 ± 0.3	12	80	0

5.7 Effect of preparation method on activity

Figure 4.26 shows that the pseudo steady state CO-conversion obtained over $Mn16^{IMPR}$ is slightly lower than the pseudo steady state CO-conversion obtained over $Mn16^{SEA}$ ($65 \pm 3\%$). A t-test was performed at pseudo steady state to check if the two data sets are significantly different. The sample t-stat value (0.22) was found to be less than the t-critical two tail value (2.2) which indicates that the data is not statistically different. This resulted in a p-value of (0.83) which is more that the significance level of 0.05 and validates the fact that the data is not significantly different. Similar pseudo steady state catalytic activity trends were obtained from $Mn26^{SEA}$-Co/SiO_2 and $Mn26^{IMPR}$-Co/SiO_2 catalysts. A t-test was performed at pseudo steady state to check if the two CO-conversion data sets are significantly different. The sample t-stat value (1.1) was found to be less than the t-critical two tail value (2.0), indicating that the data is not statistically different. The sample t-test resulted in a p-value (0.25) that is more than the significance level of 0.05; this validates the statement that the data sets are not significantly different. A summary of activity and turnover frequency for Mn^{SEA}-Co/SiO_2 and Mn^{IMPR}-Co/SiO_2 catalysts are shown in Table 5.4. $Mn16^{SEA}$-Co/SiO_2 and $Mn16^{IMPR}$-Co/SiO_2 catalysts showed similar CO-conversion, catalytic activity and turnover frequency values. $Mn26^{SEA}$-Co/SiO_2 and $Mn26^{IMPR}$-Co/SiO_2 exhibit the same pattern. Based on the t-tests performed at pseudo steady state, CO-conversions of Mn^{SEA}-Co/SiO_2 and Mn^{IMPR}-Co/SiO_2 catalysts were similar. This suggests that the change in the method of catalyst preparation from SEA to IMPR did not alter the performance of the catalysts. In addition, similar activities obtained from the two types of catalysts prepared using SEA and IMPR methods may suggest the absence of potassium, which is consistent with the results obtained from elemental quantifications using ICP-OES and STEM-EDS.

Table 5.4: Comparison of the pseudo steady state catalytic activity obtained with manganese promoted cobalt-based Fischer-Tropsch catalysts at different manganese loadings, prepared using SEA and IMPR approaches.

Catalyst	CO-conversion (%)	Cobalt-time-yield* (mmol CO/g_{Co}. s)	TOF (s^{-1})**
$Mn16^{SEA}$	65 ± 3	0.092 ± 0.005	0.16
$Mn16^{IMPR}$	62 ± 1	0.090 ± 0.003	0.15
$Mn26^{SEA}$	54 ± 3	0.079 ± 0.003	0.14
$Mn26^{IMPR}$	54 ± 3	0.077 ± 0.004	0.14

Cobalt-time-yield* (mmol CO/g_{Co}. s)=moles of CO converted/ g of Co/s

TOF**=CO moles converted/moles of H_2 uptake/s

5.8 Effect of preparation method on Fischer-Tropsch product selectivity

The catalytic performances of Mn^{SEA}-Co/SiO_2 and Mn^{IMPR}-Co/SiO_2 catalysts are summarized in Table 5.5. CH_4 selectivity of $Mn16^{SEA}$ is 1 C-% less than that of $Mn16^{IMPR}$. This suggests that a variance in CH_4 selectivity of about 1 C-% may be as a result of small changes in reactor temperature, H_2/CO ratio or both. CH_4 selectivity of $Mn26^{SEA}$ and $Mn26^{IMPR}$ is similar with slight differences in standard deviation. A t-test was performed at pseudo steady state to check if there is any significant differences in CH_4 selectivity data collected online for $Mn26^{SEA}$ and $Mn26^{IMPR}$ (presented in section 4). The sample t-stat value (0.13) was found to be less than the t-critical two tail value (2.0), suggesting that the data is not statistically different. This resulted in a p-value (0.89) that is more than the significance level of 0.05, validating the fact that the data is not significantly different.

CO_2 selectivity of $Mn16^{SEA}$ is approximately 1 C-% and this value is more than that obtained for $Mn16^{IMPR}$ (close to 0). A t-test was performed at pseudo steady state to check if there is any significant differences in the CO_2 selectivity data collected online for $Mn16^{SEA}$ and $Mn16^{IMPR}$ (presented in section 4). The sample t-stat value (19) at pseudo steady state was greater than the t-critical two tail value (2.0). This resulted in a p-value that is less than the significance level of 0.05, suggesting that the online data collected is significantly different. This may arise due to minor temperature or H_2/CO ratio fluctuations in the reactor. CO_2 selectivity of $Mn26^{SEA}$ and $Mn26^{IMPR}$ is similar as it can be seen in Table 5.5. Furthermore, the C_{5+} selectivities for Mn^{SEA}-Co/SiO_2 and Mn^{IMPR}-Co/SiO_2 catalysts are similar. The slight differences may be attributed to the minor changes of reactor temperature, H_2/CO ratio or both.

Table 5.5: Comparison of selectivities of Mn-Co/SiO_2 catalysts towards hydrocarbons at pseudo steady state obtained using different manganese loadings, prepared using SEA and IMPR approaches.

		Selectivity (mol C-%)				
Catalyst	X_{CO} (%)	CH_4	C_{2-4}	C_{5+}	CO_2 (%)	α (C_{5-7})
Mn0	46 ± 2	7.0 ± 0.4	8	84	0.43 ± 0.04	0.81
$Mn16^{SEA}$	65 ± 3	4.0 ± 0.4	8	87	0.6 ± 0.1	0.75
$Mn16^{IMPR}$	62 ± 1	5.0 ± 0.4	6	89	0	0.84
$Mn26^{SEA}$	54 ± 3	6.0 ± 0.6	8	86	0	0.77
$Mn26^{IMPR}$	54 ± 3	6.0 ± 0.1	9	85	0	0.85

6 CONCLUSIONS AND RECOMMENDATIONS

This study aimed at: a) investigating the effect of selectively adsorbed manganese onto Co/SiO_2 catalyst on the CO adsorption and dissociation in addition to the activity and selectivity and b) examining the method of catalyst doping (SEA and IMPR) on activity and selectivity.

Co/SiO_2 catalyst was prepared via wet IMPR method and manganese was successfully selectively adsorbed on the cobalt catalyst. Many studies have speculated that manganese enhances activity of cobalt-based catalysts due to the enhancement of CO adsorption and dissociation. In this study, however, there was no evidence of enhanced CO adsorption and dissociation. The presence of selectively adsorbed manganese on Co/SiO_2 catalyst resulted in the enhancement of cobalt reducibility, which possibly resulted in more active catalysts with very small amount of manganese. Higher manganese contents led to a decrease in activity due to surface blockage of cobalt active sites. Furthermore, the addition of manganese insignificantly changed the selectivity of CH_4, C_{2-4} and C_{5+}. The olefin content was the lowest with very small amount of manganese when compared to unpromoted cobalt catalyst, however, a further increase in manganese concentration resulted in an increased olefin content. This may be ascribed to differences in CO conversion and/or manganese effect. The selectivities and activities obtained from the manganese promoted Co/SiO_2 catalysts (using SEA and IMPR approaches) are similar. There was no traces of potassium adsorbed on the cobalt/silica catalyst during SEA of $[MnO_4]^{-1}$ anion from the potassium permanganate solution of pH = 1, as revealed by both ICP-OES and STEM EDS examinations. Thus, potassium did not contribute to influencing the catalytic performance of Mn^{SEA}-Co/SiO_2 catalysts. Changing the method of preparation from SEA to IMPR did not significantly alter the activity and selectivities of Mn-Co/SiO_2 catalysts. These similar activities and selectivities may suggest that the initial structural properties (size and shape) of the pre-formed Co/SiO_2 catalyst precursors remained unaltered upon the inclusion of small manganese concentrations into the cobalt-based catalyst systems and hence the obtained catalytic performances are indifferent.

The calcination of cobalt nitrate (as a precursor) to prepare silica supported cobalt catalysts resulted in the formation of cobalt clusters. Previous reports have shown that a homogeneous mixture of cobalt(II) nitrate hexahydrate and cobalt(II) acetate tetrahydrate precursors produces highly monodispersed smaller Co_3O_4 crystallites on silica support (de Beer *et al.,* 2014). **It is therefore recommended to use a mixture of cobalt nitrate and cobalt acetate sources for the preparation of smaller cobalt-based crystallites as heterogeneous catalysts**.

In this study, two catalyst preparation methods were explored, strong electrostatic adsorption of $[MnO_4]^{-1}$ and sequential impregnation of cobalt and manganese on to the support. It is therefore recommended to investigate the **co-impregnation of cobalt and manganese precursors in order to evaluate the co-genesis of these two different metals during calcination as they may result in different Fischer-Tropsch selectivity products.**

STEM-EDS examination using SEM technique showed homogeneous distribution of manganese on cobalt catalysts. However, detailed analyses on single cobalt clusters is lacking in this current study. **It is therefore highly recommended to perform detailed structural investigations on single cobalt-based clusters using high resolution scanning transmission electron microscopy coupled with energy dispersive X-ray spectroscopy (STEM-EDS).**

7 REFERENCES

Aasberg-Petersen, K., Christensen, T.S., Stub Nielsen, C. & Dybkjær, I. 2003. Recent developments in autothermal reforming for synthesis gas production in GTL applications. *Fuel Processing Technology* **83**(1-3):253-261.

Arsalanfar, M., Mirzaei, A. & Bozorgazadeh, H. 2013. Effect of preparation method on catalytic performance, structure and surface reaction rates of MgO supported Fe–Co–Mn catalyst for CO hydrogenation. *Journal of Industrial and Engineering Chemistry* **19**:478-487.

Balonek, C.M., Lillebø, A.H., Rytter, E., Schmidt, L.D. & Holmen, A. 2010. Effect of Alkali Metal Impurities on Co-Re Catalysts for Fischer-Tropsch Synthesis from Biomass-Derived Syngas. *Catalysis Letters* **138**(1-2):8-13.

Barrault, J. 1982. Selective hydrogenation of carbon monoxide on supported Iron or cobalt catalysts. Effects of manganese oxide and (or) chlorine. *Studies in Surface Science and Catalysis* **11**:225-231.

Bezemer, G., Radstake, P., Falke, U., Oosterbeek, H., Kuipers, H., van Dillen, A. & de Jong, K. 2006. Investigation of promoter effects of manganese oxide on carbon nanofiber-supported cobalt catalysts for Fischer–Tropsch synthesis. *Journal of Catalysis* **237**:152-161.

Bianchi, C., Pirola, C. & Ragaini, V. 2006. Choosing the best diluent for a fixed catalytic bed: The case of CO hydrogenation. *Catalysis Communications* **7**:669-672.

Boerrigter, H. 2006. Economy of biomass-to-liquids (BTL) plants: An engineering assessment. *ECN-report* ECN-C--06-019*, Petten, The Netherlands.(*www.ecn.nl/biomass*).*

Borg, Ø., Hammer, N., Enger, B.C., Myrstad, R., Lindvåg, O.A., Eri, S., Skagseth, T.H. & Rytter, E. 2011. Effect of biomass-derived synthesis gas impurity elements on cobalt Fischer–Tropsch catalyst performance including in situ sulphur and nitrogen addition. *Journal of Catalysis* **279**(1):163-173.

Bukur, D.B., Pan, Z., Ma, W., Jacobs, G. & Davis, B.H. 2012. Effect of CO conversion on the product distribution of $Co/Al_2/O_3$ Fischer-Tropsch synthesis catalyst using a fixed bed reactor. *Catalysis Letters* **142**:1382-1387.

Bunaciu, A., Udri, S. & Aboul-EneIn, H. 2015. X-Ray Diffraction: Instrumentation and Applications. *Critical Reviews in Analytical Chemistry* **45**:289-299.

Castner, D., Watson, P. & Chan, I. Y. 1990. X-ray absorption spectroscopy, X-ray photoelectron spectroscopy, and analytical electron microscopy studies of cobalt catalysts. 2. Hydrogen reduction properties. *The Journal of Physical Chemistry* **94**(2): 819-828.

Chan, C. & Weinberg, W. 1978. An analysis of thermal desorption mass spectra. II. *Applications of Surface Science.* **1**(3):377-387.

Claeys, M. & van Steen, E. 2004. Fischer-Tropsch sythesis: Basic studies. *Studies in Surface and Catalysis* **152**:601-680.

Cvetanović, R. & Amenomiya, Y. 1967. Application of a Temperature Programmed desoprtion Technique to Catalyst studies. *Applied Chemistry* **17**:104-149.

de Beer, M., Claeys, M. & van Steen, E. 2014. Preparation of Pt-promoted Co/SiO_2 catalysts for CO hydrogenation by strong electrostatic adsorption (SEA). *Advanced Materials Research* **1019**:357-364.

de Beer, M., Kunene, A., Nabaho, D., Claeys, M. & van Steen, E. 2014. Technical and economic aspects of promotion of cobalt-based Fischer-Tropsch catalysts by noble metals-a review. *Journal of the Southern African Institute of Mining and Metallurgy.* **114**(2):157-165.

Deraz, N. 2018. The comparative jurisprudence of catalysts preparation methods: I. precipitation and impregnation methods. *Journal of Industrial and Environmental Chemistry* **2**(1):19-21.

Dimitriou, I., Goldingay, H. & Bridgwater, A. V. 2018. Techno-economic and uncertainty analysis of Biomass to Liquid (BTL) systems for transport fuel production. *Renewable and Sustainable Energy Reviews* **88**:160-175.

Dinse, A., Aigner, M., Ulbrich, M., Johnson, G.R. & Bell, A. 2012. Effects of Mn promotion on the activity and selectivity of Co/SiO_2 for Fischer–Tropsch synthesis. *Journal of Catalysis* **288**:104-114.

Dry, M. E. 2002. The Fischer-Tropsch process: 1950-2000. *Catalysis Today* **71**:227-241.

Eliseev, O. L., Tsapkina, M.V., Dement'eva, O.S., Davydov, P.E., Kazakov, A.V. & Lapidus, A.L. 2013. Promotion of cobalt catalysts for the Fischer-Tropsch synthesis with alkali metals. *Kinetics and Catalysis* **54**(2):207-212.

Elmer, T.H. & Nordberg, M.E. 1958. Solubility of silica in nitric acid solutions. *Journal of the American Ceramic Society* **41**(12):517-520.

Energy database. 2014. *Enerdata intelligence+consulting.* [Online]. Available at: http://www.enerdata.net/publications/executive-briefing/future-gas-liquid-qtl-industry.html. [Accessed 07 April 2021].

Erley, W. & Wagner, H. 1978. Thermal decomposition of CO on a stepped Ni surface. *Surface Science* **74**:333-341.

Ernst, B., Bensaddik, A., Hilaire, L., Chaumette, P. & Kiennemann, A. 1998. Study on a cobalt silica catalyst during reduction and Fischer–Tropsch reaction: In situ EXAFS compared to XPS and XRD. *Catalysis Today* **39**(4):329-341.

Espinoza, R. L., Visagie, J. L., Van Berge, P. J. & Bolder, F. H. 1998. Catalysts. Johannesburg, South Africa, Patent No. 5,733,839.

Feller, A., Claeys, M. & van Steen, E. 1999. Cobalt cluster effects in zirconium promoted Co/SiO_2 Fischer-Tropsch catalysts. *Journal of Catalysis* **185**:120-130.

Feltes, T.E., Espinosa-Alonso, L., de Smit, E., D'Souza, L., Meyer, R.J., Weckhuysen, B.M. & Regalbuto, J.R. 2010. Selective adsorption of manganese onto cobalt for optimized Mn/Co/TiO_2 Fischer-Tropsch catalysts. *Journal of Catalysis* **270**: 95-102.

Fischer, F. & Tropsch, H. 1925. Process for production of paraffin hydrocarbons from carbon monoxide and hydrogen by catalytic paths. *German, Patent* No. 484,337.

Gabbott, P. 2008. Principles and applications of thermal analysis. *John Wiley & Sons.*

Gaube, J. & Klein, H. 2008. The promoter effect of alkali in Fischer-Tropsch iron and cobalt catalysts. *Applied Catalysis A: General* **350**: 126–132.

Gholami, Z., Tišler, Z. & Rubáš, V. 2020. Recent advances in Fischer-Tropsch synthesis using cobalt-based catalysts: a review on supports, promoters, and reactors. *Catalysis Reviews* (in press): DOI: 10.1080/01614940.2020.1762367.

Gholami, Z., Zabidi, N.A.M., Gholami, F., Ayodele, O.B. & Vakili, M. 2017. The influence of catalyst factors for sustainable production of hydrocarbons via Fischer-Tropsch synthesis. *Reviews in Chemical Engineering* **33**(4):337-358.

Ghosh, I.K., Iqbal, Z., van Heerden, T., van Steen, E. & Bordoloi, A. 2020. Insights into the unusual role of chlorine in product selectivity for direct hydrogenation of CO/CO_2 to short-chain olefins. *Chemical Engineering Journal.* **413**:127424.

Han, F., Zhang, Z., Niu, N. & Li, J. 2018. Preparation and characterization of SiO_2/Co and C/Co nanocomposites as Fischer-Tropsch catalysts for CO_2 hydrogenation. *Chemical Research in Chinese Universities* **130**(1):72-78.

Hashemzehi, H., Mirzaei, A., Atashi, H. & Rezaeian, F. 2017. The study of catalytic performance of silica supported three metallic Fe–Co–Ce catalyst prepared using impregnation procedure for Fischer–Tropsch synthesis. *Petroleum Science and Technology* **35**(24):2229-2234.

Hu, Y. & Ruckenstein, E. 1996. Temperature-programmed desorption of CO adsorbed on NiO/MgO. *Journal of Catalysis* **163**:306-311.

Iglesia, E. 1992. Fischer-Tropsch synthesis on cobalt and ruthenium. Metal dispersion and support effects on reaction rate and selectivity. *Journal of Catalysis* **137**(1):212-224.

Iglesia, E. 1997. Design, sythesis, and use of cobalt-based Fischer-Tropsch sythesis catalysts. *Applied Catalysis A* **161**(1-2):59-78.

Jalama, K., Kabuba, J., Xiong, H. & Jewell, L.L. 2002. Co/TiO_2 Fischer-Tropsch catalyst activation by synthesis gas. *Catalysis Communications.* **17**:154-159.

Jiang, F., Zhang, M., Liu, B., Xu, Y. & Liu, X. 2017. Insights into the influence of support and potassium or sulfur promoter on iron-based Fischer–Tropsch synthesis: Understanding the control of catalytic activity, selectivity to lower olefins, and catalyst deactivation. *Catalysis Science and Technology* **7**(5):1245-1265.

Johnson, G.R., Werner, S. & Bell, A. 2015. An investigation into the effects of Mn promotion on the activity and selectivity of Co/SiO_2 for Fischer-Tropsch synthesis: Evidence for enhanced CO adsorption and dissociation. *ACS Catalysis* **5**:5888-5903.

Johnson, G. & Bell, A. 2016. Role of ZrO_2 in promoting the activity and selectivity of Co-based Fischer−Tropsch synthesis catalysts. *ACS Catalysis* **6**:100-114.

Jung, J. S., Kim, S. W. & Moon, D. J. 2012. Fischer–Tropsch synthesis over cobalt based catalyst supported on different mesoporous silica. *Catalysis Today* **185**(1):168-174.

Khodakov, A. Y., Chu, W. & Fongarland, P. 2007. Advances in the development of novel cobalt Fischer−Tropsch catalysts for synthesis of long-chain hydrocarbons and clean fuels. *Chemical Reviews* **107:**1692-1744.

Kiskinova, M. 1991. Poisoning and Promotion in Catalysis based on Surface Science Concepts and Experiments*. Studies in Surface Science and Catalysis*Vol. 70, Elsevier. United States of America.

Lee, R.A. & Lavoie, J.M. 2013. From first- to third-generation biofuels: Challenges of producing a commodity from a biomass of increasing complexity. *Animal Frontiers.* **3**(2):6-11.

Li, J., Cheng, X., Zhang, C., Yang, Y. & Li, Y. 2015. Effects of alkali on iron-based catalysts for Fischer-Tropsch synthesis: CO chemisorptions study. *Journal of Molecular Catalysis A* **396**:74-180.

Lillebø, A.H., Patanou, E., Yang, J., Blekkan, E.A. & Holmen, A. 2013. The effect of alkali and alkaline earth elements on cobalt-based Fischer-Tropsch catalysts. *Catalysis today* **215**:60-66.

Liu, G., Larson, E.D., Williams, R.H., Kreutz, T.G. & Guo, X. 2011. Making Fischer-Tropsch fuels and electricity from coal and biomass: Performance and cost analysis. *Energy & Fuels* **25**(1):415-437.

Macheli, L., Carleschi, E., Doyle, B.P., Leteba, G. & van Steen, E. 2021. Tuning catalytic performance in Fischer-Tropsch synthesis by metal-support interactions. *Journal of Catalysis.* **395**:70-79.

Macheli, L., Roy, A., Carleschi, E., Doyle, B.P. & van Steen, E. 2020. Surface modification of Co_3O_4 nanocubes with TEOS for an improved performance in the Fischer-Tropsch synthesis. *Catalysis Today.* **343**:176-182.

Maji, I., Sulaiman, C. & Abdul-Rahim, A. 2019. Renewable energy consumption and economic growth nexus: A fresh evidence from West Africa. *Energy Reports* **5**:384-392.

Makhura, E., Rakereng, J., Rapoo, O. & Danha, G. 2019. Effect of the operation parameters on the Fischer-Tropsch synthesis process using different reactors. *Procedia Manufacturing.* **35**:349-355.

Malet, P. & Caballero, A. 1988. The selection of experimental conditions in temperature-programmed reduction experiments. *Journal of the Chemical Society, Faraday Transactions 1: Physical Chemistry in Condensed Phases* **84**(7):2369.

Marin, R. P., Kondrat, S.A., Davies, T.E., Morgan, D.J., Enache, D.I., Combes, G.B., Taylor, S.H., Bartley, J.K. & Hutchings, G.J. 2014. Novel cobalt zinc oxide Fischer–Tropsch catalysts synthesised using supercritical anti-solvent precipitation. *Catalysis Science & Technology* **4**(7):1970-1978.

Menczel, J. D. & Prime, R. B. 2014. Thermal analysis of polymers: fundamentals and applications. *John Wiley & Sons.*

Morales, F., de Smit, E., de Groot, F.M., Visser, T. & Weckhuysen, B.M. 2007. Effects of manganese oxide promoter on the CO and H_2 adsorption properties of titania-supported cobalt Fischer–Tropsch catalysts. *Journal of Catalysis* **246**:91-99.

Morales, F., Weckhuysen, B.M., Spivey, J.J. & Dooley K.M. 2006. Promotion effects in Co-based Fischer-Tropsch catalysis. *Catalysis* **19**:1-40.

Munirathinam, R., Pham Minh, D. & Nzihou, A. 2018. Effect of the support and its surface modifications in cobalt-based Fischer-Tropsch synthesis. *Industrial & Engineering Chemistry Research* **57**(48):16137-16161.

Munnik, P., de Jongh, P. & de Jong, K. P. 2015. Recent Developments in the Synthesis of Supported Catalysts. *Chemical Reviews* **115**:6687-6718.

Naboho, D., Niemantsverdriet, J.H., Claeys, M. & van Steen, E. 2016. Hydrogen spillover in the Fischer-Tropsch synthesis: An analysis of platinum as a promoter for cobalt-alumina catalysts. *Catalysis Today.* **261**:17-27.

Naik, S.N., Goud, V.V., Rout, P.K. & Dalai, A.K. 2010. Production of first and second generation biofuels: A comprehensive review. *Renewable and Sustainable Energy Reviews* **14**:578–597.

Nieskens, D., van Bavel, A. & Niemantsverdriet, J. 2003. The analysis of temperature programmed desorption experiments of systems with lateral interactions; implications of the compensation effect. *Surface Science.* **546**:159-169.

Oukaci, R., Singleton, A.H. & Goodwin, J.G. 1999. Comparison of patented Co F-T catalysts using fixed-bed and slurry bubble column reactors. *Applied Catalysis A: General* **186**(1-2):129-144.

Owusu, P. & Asumadu-Sarkodie, S. 2016. A review of renewable energy sources, sustainability issues and climate change mitigation. *Cogent Engineering,* **3**: 1167990.

Pan, Z. & Bukur, D. B. 2011. Fischer–Tropsch synthesis on Co/ZnO catalyst - Effect of pretreatment procedure. *Applied Catalysis A: General* **404**(1-2):74-80.

Pedersen, O.E., Svenum, I.H. & Blekkan, E. A. 2018. Mn promoted Co catalysts for Fischer-Tropsch production of light olefins-An experimental and theoretical study. *Journal of Catalysis* **361**:23-32.

Petersen, M.A., Cariem, M.J., Claeys, M. & van Steen, E. 2015. A DFT perspective of potassium promotion of X-Fe5C2(1 0 0). *Applied Catalysis A: General.* **496**:64-72.

Pirola, C., Galli, F. & Patience, G.S. 2018. Experimental methods in chemical engineering: Temperature programmed reduction-TPR. *The Canadian Journal of Chemical Engineering* **96**(11):2317-2320.

Ponec, V. 1978. Some aspects of the mechanism of methanation and Fischer-Tropsch synthesis. *Catalysis Reviews* **18**(1):151-171.

Puskas, I. & Hurlbut, R. 2003. Comments about the causes of deviations from the Anderson-Schulz-Flory distribution of the Fischer-Tropsch reaction products. *Catalysis Today* **84**(1-2):99-109.

Puskas, I. 1993. Telomerization model for cobalt-catalysed Fischer-Tropsch products. *Journal of Catalysis* **139**(2):591-601.

Raub, Andrew., Karroum, Hafsa., Athariboroujeny, M. & Kruse, N. 2021. Chemical transient kinetics in studies of the Fischer-Tropsch reaction and beyond. *Catalysis Letters* **151**:613-626.

Redhead, P.A. 1962. Thermal desorption of gases. *Vacuum.* **12**(4):203-211.

Reuel, R.C. & Bartholomew, C.H. 1984. The stoichiometries of H_2 and CO adsorptions on cobalt: Effects of support and preparation. *Journal of Catalysis* **85**:63-77.

Reuel, R. & Bartholomew, C. H. 1984. Effects of support and dispersion on the CO hydrogenation activity/selectivity properties of cobalt. *Journal of Catalysis* **85**(1):78-88.

Riedel, T., Claeys, M., Schulz, H., Schaub, G., Nam, S.S., Jun, K.W., Choi, M.J., Kishan, G. & Lee, K.W. 1999. Comparative study of Fischer-Tropsch synthesis with H_2/CO and H_2/CO_2 syngas using Fe-and Co-based catalysts. *Applied Catalysis A: General* **186**(1-2):201-213.

Roddy, D. 2012. Biomass in the petrochemical world. *Interface Focus.* **3**(1): 20120038.

Rostrup-Nielsen, J.R. 2002. Syngas in perspective. *Catalysis Today* **17**(3-4):243-247.

Rytter, E. & Holmen, A. 2015. Deactivation and regeneration of commercial type Fischer-Tropsch Co-catalysts-A mini-review. *Catalysts* **5**(2):478-499.

Rytter, E., Borg, Ø., Tsakoumis, N. E. & Holmen, A. 2018. Water as key to activity and selectivity in Co Fischer-Tropsch synthesis: γ-alumina based structure-performance relationships. *Journal of Catalysis* **365**:334-343.

Saib, A., Claeys, M. & van Steen, E. 2002. Silica supported cobalt Fischer–Tropsch catalysts: effect of pore diameter of support. *Catalysis Today* **71**:395-402.

Schroeder, S. L. & Gottfried, M. 2002. Temperature-Programmed Desorption (TPD) Thermal Desorption Spectroscopy (TDS). *Advanced Physical Chemistry.* **18**:1-22.

Schulz, H., Schaub, G., Claeys, M. & Riedel, T. 1999. Transient initial kinetic regimes of Fischer-Tropsch synthesis. *Applied Catalysis A: General* **186**:215-227.

Schulz, H., B¨ohringer, W., Kohl, C., Rahman, N. & Will, A. 1984. Development and application of the capillary GC total sampling technique for gas/vapor multicomponent mixtures. *DGMK Forschungsbericht* **3**:320-329.

Schwarz, J., Contescu, C. & Contescu, A. 1995. Methods for preparation of catalytic materials. *Chemical Reviews* **95**(3):477-510.

Shi, Z., Yang, H., Gao, P., Chen, X., Liu, H., Zhong,L., Wang, H., Wei, W. & Sun, Y. 2018. Effect of alkali metals on the performance of $CoCu/TiO_2$ catalysts for CO_2 hydrogenation to long-chain hydrocarbons. *Chinese Journal of Catalysis* **39**(8):1294-1302.

Shimura, K., Miyazawa, T., Hanaoka, T. & Hirata, S. 2015. Fischer–Tropsch synthesis over alumina supported cobalt catalyst: Effect of promoter addition. *Applied Catalysis A: General* **494**:1-11.

Sneddon, J. & Vincent, M.D. 2008. ICP-OES and ICP-MS for the determination of metals: application to oysters. *Analytical Letters* **41**(8):1291-1303.

Storsæter, S., Tøtdal, B., Walmsley, J.C., Tanem, B.S. & Holmen, A. 2005. Characterisation of alumina, silica, and titania supported cobalt Fischer-Tropsch catalysts. *Journal of Catalysis* **236**(1):139-152.

Sun, S., Tsubaki, N. & Fujimoto, K. 2000. The reaction perfomances and characterisation of Fischer-Tropsch sythesis Co/SiO_2 catalysts prepared from mixed cobalt catalysts. *Applied Catalysis A: General* **202**:121-131.

Thiessen, J., Rose, A., Meyer, J., Jess, A. & Currulla-Ferré, D. 2012. Effects of manganese and reduction promoters on carbon nanotube supported cobalt catalysts in Fischer-Tropsch synthesis. *Microporous and Mesoporous Materials* **164**:199-206.

Tian, Z., Wang, C., Yue, J., Zhang, X. & Ma, L. 2019. Effect of a potassium promoter on the Fischer Tropsch synthesis of light olefins over iron carbide catalysts encapsulated in graphene like carbon. *Catalysis Science and Technology* **9**(11):2728-2741.

Tijmensen, M.J.A., Faaij, A.P.C., Hamelinck, C.N. & van Hardeveld, M.R.M. 2002. Exploration of the possibilities for production of Fischer-Tropsch liquids and power via biomass gasification. *Biomass & Bioenergy* **23**:129-152.

Tucker, C.L. & van Steen, E. 2020. Activity and selectivity of cobalt-based Fischer-Tropsch catalyst operating at high conversion for once-through biomass operation. *Catalysis Today* **342**:115-123.

Uner, D.O. 1998. A sensible mechanism of alkali promotion in Fischer-Tropsch synthesis: adsorbate mobilities. *Industrial & Engineering Chemistry Research* **37**(6):2239-2245.

van de Loosdrecht, J., Botes, F.G., Ciobica, I.M., Ferreira, A.C., Gibson, P., Moodley, D.J., Saib, A.M., Visagie, J.L., Weststrate, C.J. & Niemantsverdriet, J.W. 2013. Fischer-Tropsch synthesis: Catalysts and Chemistry. *Compreshensive Inorganic Chemistry II: from elements for applications* **7**:525-557. Elsevier.

van Santen, R.A., Markvoort A.J, Ghouri M.M., Hilbers, P.A.J. & Hensen, E.J.M. 2013. Monomer formation model versus chain growth model of the Fischer-Tropsch reaction. *Journal of Physical Chemistry C* **117**(9):4488-4504.

van Steen, E., Sewell, G.S., Makhothe, R.A., Micklethwaite, C., Manstein, H., de Lange, M. & O'Connor, C.T. 1996. TPR study on the preparation of impregnated Co/SiO_2 catalysts. *Journal of Catalysis* **162**(2):220-229.

van Steen, E., Claeys, M., Möller, K.P. & Nabaho, D. 2018. Comparing a cobalt-based catalyst with iron-based catalysts for the Fischer-Tropsch XTL-process operating at high conversion. *Applied Catalysis A: General* **549**:51-59.

Vannice, M. 1975. The catalytic synthesis of hydrocarbons from H_2/CO mixtures over the group VIII metals. *Journal of Catalysis* **37**:449-461.

Viswanathan, B., Gopalakrishnan, R. & Vetrivel, R. 1981. Temperature programmed desoprtion (TPD) of carbon monoxide from cobalt surfaces. *Reaction Kinetics and Catalysis Letters* **18**(1):209-212.

Wang, T., Ding, Y., Xiong, J., Yan, L., Zhu, H., Lu, Y. & Lin, L. 2005. Effect of vanadium promotion on activated carbon-supported cobalt catalysts in Fischer-Tropsch synthesis. *Catalysis Letters* **107**(1):47-52.

Wang, T., Wang, J. & Jin, Y. 2007. Slurry reactors for gas-to-liquid processes: a review. *Industrial & Engineering chemistry research.* **46**(18):5824-5847.

Wesner, D., Linden, G. & Bonzel, H. 1986. Alkali promotion on cobalt: Surface analysis of the effetc of potassium on carbon monoxide adsorption and Fischer-Tropsch reaction. *Applied Surface Science* **26**(3):335-356.

Xiong, H., Motchelaho, M.A., Moyo, M., Jewel, L.L. & Coville, N.J. 2015. Effect of group I alkali metal promoters on Fe/CNT catalysts in Fischer–Tropsch synthesis. *Fuel* **150**:687-696.

Xu, R., Hou, C., Xia, G., Sun, X., Li, m., Nie, H. & Li, D. 2020. Effects of Ag promotion for Co/Al_2O_3 catalyst in Fischer-Tropsch synthesis. *Catalysis Today* **342**:111-114.

Zhou, L. 2005. Progress and problems in hydrogen storage methods. *Renewable and Sustainable Energy Reviews* **9**:395-408.

Zhao, Y., Feltes, T.E., Regalbuto, J.R., Meyer, R.J. & Klie, R.F. 2011. Analytical scanning transmission electron microscopy study of the support effects on Mn-promoted Co Fischer-Tropsch catalysts. *Catalysis Science & Technology* **1**:1483-1489.

Zowtiak, J. & Bartholomew, C. 1983. The kinetics of H_2 adsorption on and desorption from cobalt and the effects of support thereon. *Journal of Catalysis* **83**(1):107-120.

.

8 APPENDICES

Appendix A: Reactor temperature profile

The reactor was heated using three heating coils, one at the top, one in the middle, and one at the bottom. Each zone is coupled with a thermo-couple located on the outside of the reactor. Due to 3 different heating zones, there is an uneven distribution of heat across the reactor tube. As such, a temperature profile across the reactor tube was determined to obtain the isothermal zone.

The reactor tube was filled with SiC and the temperature profile was measured starting 4 cm from the outlet of the reactor tube. The reactor temperature profile was obtained by moving a thermocouple through the thermowell along the reactor length. Prior to this, the reactor temperature was set to 220 °C. The temperature and position of the thermocouple were recorded. A similar experiment was repeated to check for reproducibility. Figure 8.1 shows the temperature profile along the reactor tube. The temperature of the reactor bed increases with length from 4 cm to 7 cm. From 7 cm to 11 cm, the temperature of the bed is 220 $\pm$ 1 °C. This is where the isothermal zone is. The temperature of the bed then drops with further increase in reactor tube length.

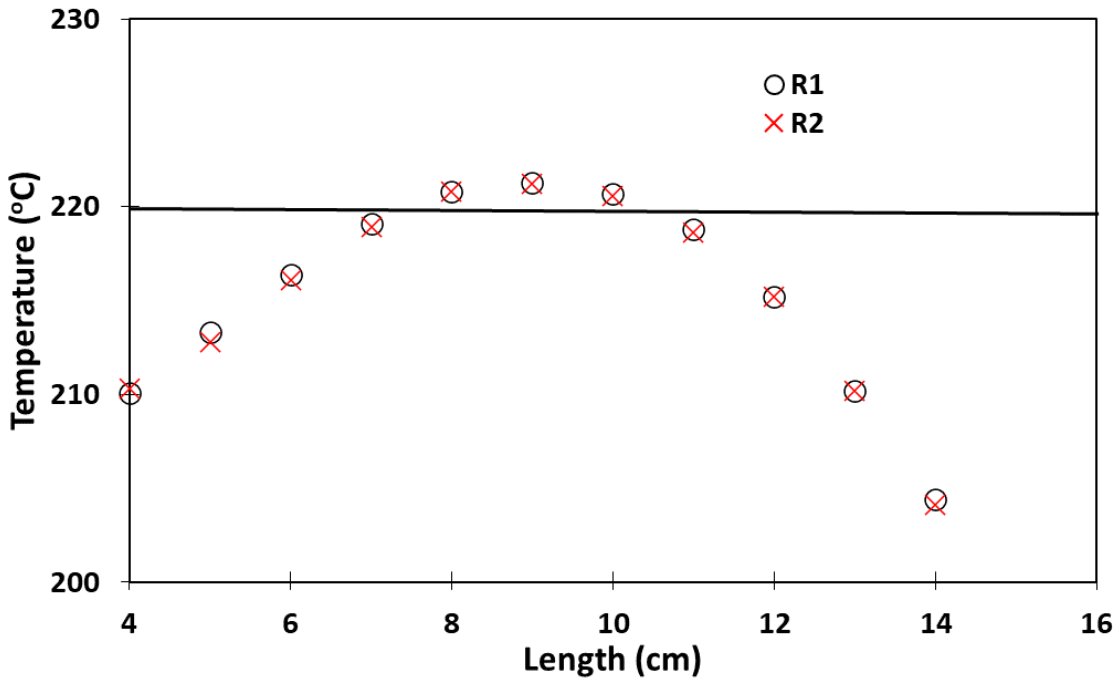

Figure 8.1: Fixed bed reactor temperature profile with R1 = the first experiment and R2 = the repeated experiment.

Appendix B: Calibration of the mass flow controllers (MFC)

The flowrates of Ar, H_2, N_2 and CO are regulated and monitored as percentages using mass flow controllers. To determine the flowrates of each gas in ml (NTP)/min, a glass bubble flow meter connected to the outlet reactor was used. The teat dropper at the end of the calibrated bubble meter was filled with soapy water. To wet the inner walls of the graduated tube, the teat was squeezed a couple of times, allowing the bubbles to reach the top. The teat was then squeezed once, to create a single bubble ring. The time taken by the bubble ring to travel within a volume space of 20 ml was recorded for each set point.

H_2 mass flow calibration

Table 8.1: H_2 mass flow calibration measurements at different set points.

	Time (s)					
Set point (%)	Run 1	Run 2	Run 3	Run 4	Average Time (s)	Flowrate (ml (NTP)/min)
30	36.44	35.84	36.87	38.45	36.90	135.2
40	19.51	20.21	20.53	20.74	20.25	108.8
50	13.46	13.64	13.55	13.55	13.55	89.35
60	10.47	10.63	10.46	10.42	10.50	61.15
70	8.74	8.57	8.46	8.57	8.59	32.33

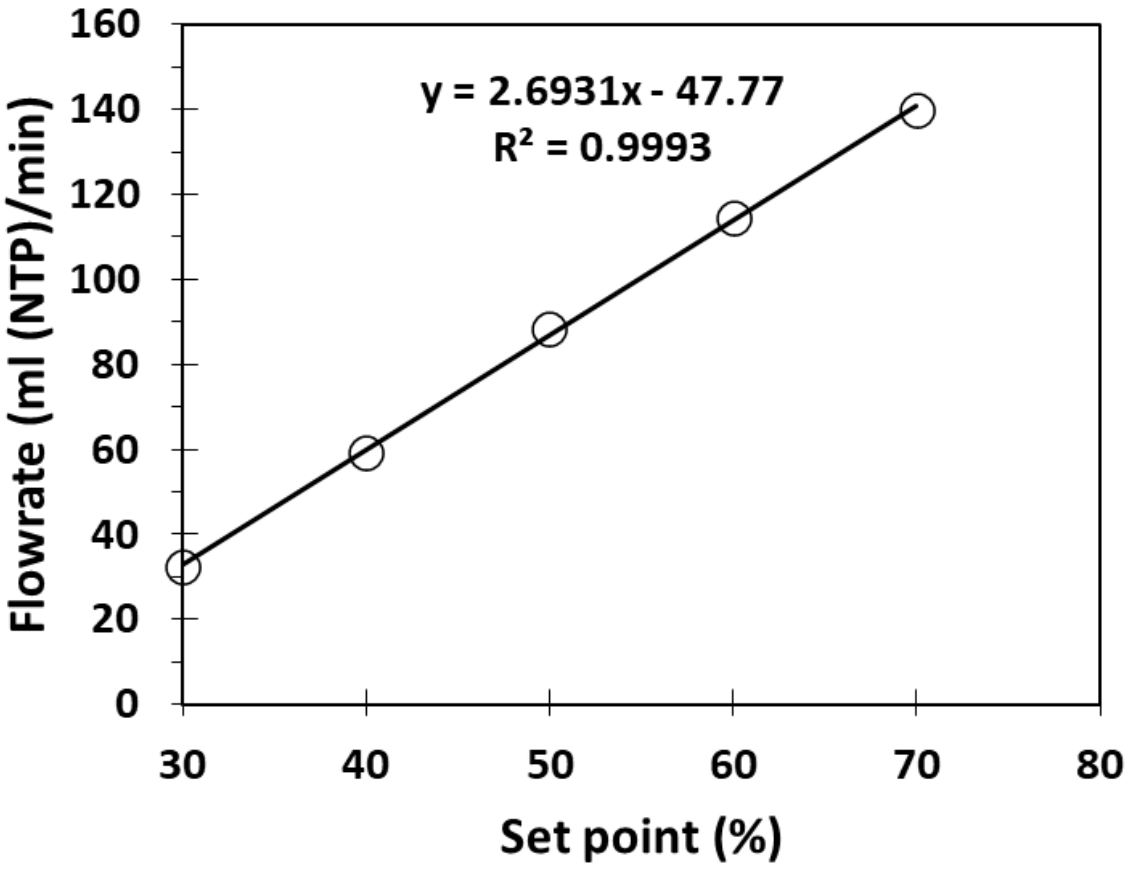

Figure 8.2: H_2 mass flow calibration curve.

CO mass flow calibration

Table 8.2: CO mass flow calibration measurements at different set points.

	Time (s)					
Set point (%)	Run 1	Run 2	Run 3	Run 4	Average Time (s)	Flowrate (ml (NTP)/min)
30	74.30	74.30	74.30	74.30	74.30	16.15
45	32.13	32.35	33.87	33.37	32.93	36.46
60	20.44	20.96	22.47	22.12	21.50	55.90
75	14.89	14.89	14.97	14.87	14.91	80.51
85	12.86	12.39	12.70	12.86	12.70	94.50
98	10.49	10.69	10.56	10.87	10.65	112.7

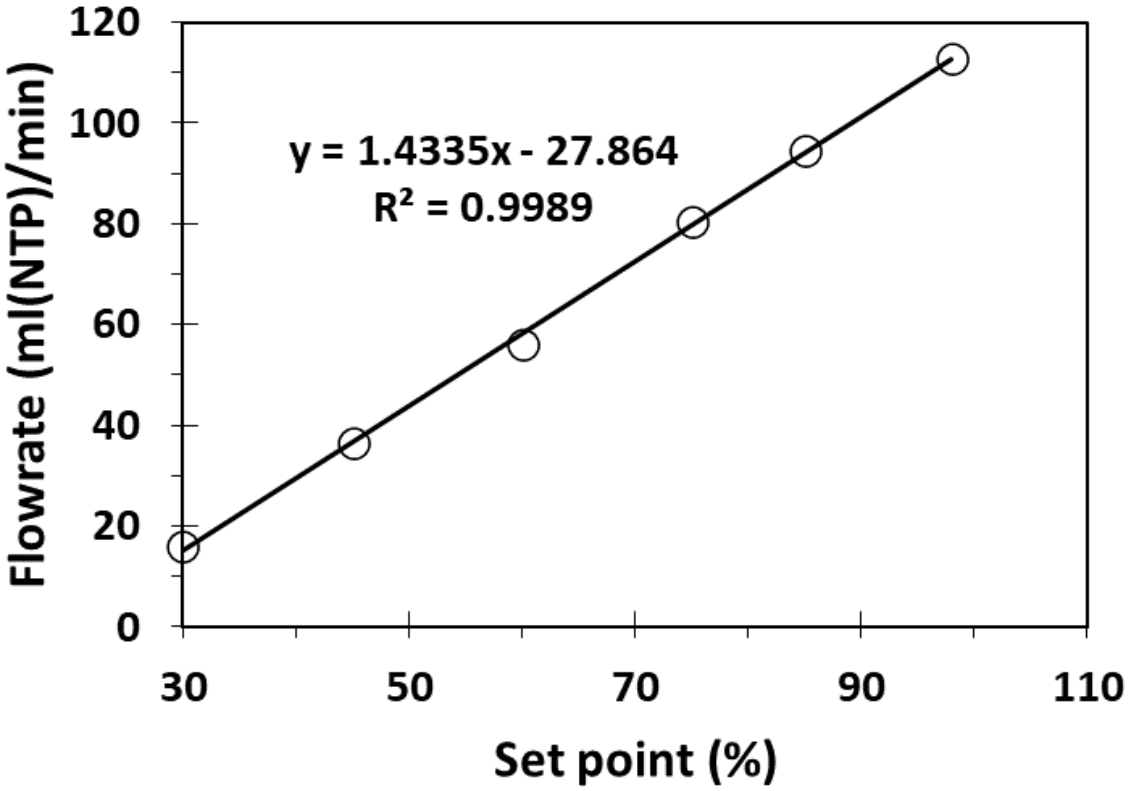

Figure 8.3: CO mass flow calibration curve.

N_2 mass flow calibration

Table 8.3: N_2 mass flow calibration measurements at different set points.

	Time (s)					
Set point (%)	Run 1	Run 2	Run 3	Run 4	Average Time (s)	Flowrate (ml (NTP)/min)
45	60.90	60.14	60.12	60.13	60.32	19.90
60	43.22	43.94	44.09	42.85	43.53	27.57
75	34.34	30.98	31.03	33.77	32.53	36.97
90	25.73	26.08	24.97	26.66	25.86	46.43
98	23.16	22.41	22.01	24.01	23.13	51.92

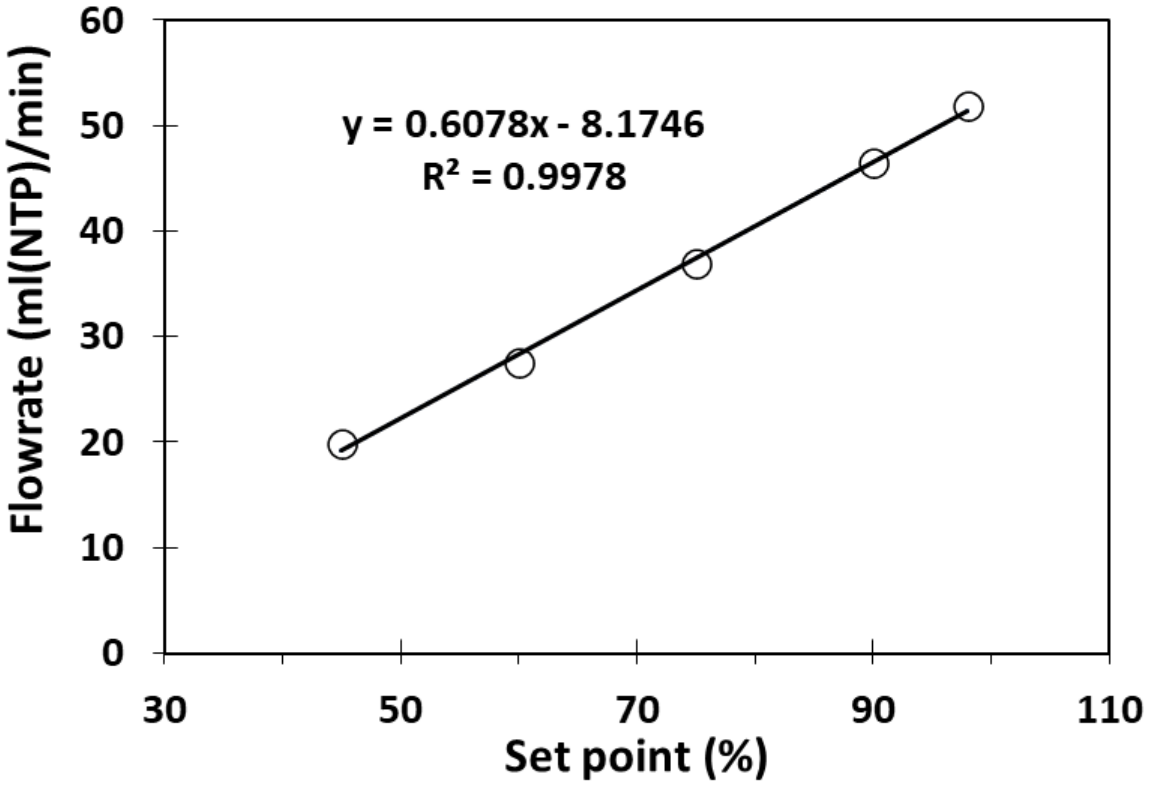

Figure 8.4: N_2 mass flow calibration curve.

Appendix C: Leak Testing

Prior to catalyst reduction and catalyst testing, the reactor was pressurized with Ar (22 barg) to test for leaks. The reactor was left for 24 hrs and the pressure drop was noted. Pressure drop of 0.5-1 barg over a period of 24 hrs was deemed acceptable.

Appendix D: Degree of reduction of Co sample calculations for Co_3O_4/SiO_2 catalyst.

Sample calculations for reduction times of 4 hrs:

$$Starting\ mass\ of\ sample = 0.9914g$$

$$Mass\ of\ Co\ in\ sample = 0.9914g \times 22\ wt.\%$$

$$Mass\ of\ Co = 0.218108g$$

$$Moles\ of\ Co = \frac{Mass\ of\ Co}{MW\ Co}$$

$$Moles\ of\ Co = 3.701137\ \times 10^{-3} moles$$

$$Final\ mass\ of\ sample = 0.9193g$$

$$Loss\ in\ mass = 0.9914g - 0.9193g$$

$$Loss\ in\ mass = 0.0721g$$

$$Amount\ of\ oxygen\ lost = \frac{0.0721g}{MW\ of\ O}$$

$$Amount\ of\ O\ lost = 4.50625\ \times 10^{-3}\ moles\ of\ O$$

$$Degree\ of\ reduction\ of\ Co_3O_4 = \left(\frac{initial\ amount\ of\ Co\ (moles)}{moles\ of\ O\ lost}\right)\left(\frac{4}{3}\right)$$

$$Degree\ of\ reduction\ of\ Co_3O_4 = 91.31\ \%$$

The degree of reduction for Mn^{SEA}-Co_3O_4/SiO_2 catalysts was calculated the same way.

Appendix E: Autochem Loop calibration.

Loop calibration was done to verify the exact volume of the injection loop for use on pulse chemisorption analysis. The calibration gases used are a) He (10 ml (NTP)/min) as the carrier gas and b) Ar (10 ml (NTP)/min) as the loop gas. During the test, 3 manual injections of Ar were made. Here, a 0.5 ml syringe was filled up with Ar and used for manual injections. After the 3rd manual injection, the analyzer in the Autochem 2029 automatically made 3 Ar injections using the loop. Each manual and automatic injection is represented by peaks which correspond to the amount of Ar injected. The following calculations were done to obtain the exact volume of the loop (extracted from the Autochem 2029 manual).

$$V_{S_{STP}} = V_S\left(\frac{273.15}{273.15 + T_a}\right) \times \left(\frac{P_a}{760\ mmHg}\right)$$

$$V_l = \left(A_l \times \frac{V_{S_{STP}}}{A_S}\right)$$

$V_{S_{STP}}$ Volume of the syringe at STP, cm^3

V_S Physical volume of the syringe, cm^3

T_a Ambient Temperature, °C

P_a Ambient pressure, mmHg

V_l Effective loop volume, cm^3

A_l Average peak areas of automatic loop injections

A_S Average peak areas of syringe injections

Table 8.4: Summary results from the loop calibration calculations.

Number of injections	A_S	A_l	$V_{S_{STP}}$ (ml)	V_S (ml)	V_l(ml)
1	0.666815644	0.45933	0.4580748	0.5	0.31363
2	0.678305426	0.463341			
3	0.67111116	0.457789			
Average	0.67207741	0.460153			

Therefore, the volume of the loop is 0.314 ml.

Appendix F: Quantifying H_2 consumed during H_2-TPR.

H_2 pulse chemisorption measurements were conducted on a Micrometrics Autochem HP 2920. Approximately 37 mg of each Mn^{SEA}-Co_3O_4/SiO_2 sample was sandwiched between a small amount of quartz wool in a quartz U-tube reactor. A sample loop was filled by constantly flowing 5% H_2/Ar (50 ml (NTP)/min) through. 80 doses of 5% H_2/Ar were pulsed into the carrier gas, He (50 ml (NTP)/min), until the surface was saturated. This was determined from the TCD response produced by the successive injections of equal volumes of 5% H_2/Ar on the sample. During the first few injections, CO may be taken up completely by the sample, hence no change in signal is recorded by the detector. As the sample reaches saturation, peaks representing the amount of unreacted 5% H_2/Ar appear. When the surface is saturated, each of the injected gas

volumes emerges from the sample tube unchanged and the detected peak areas are constant. From the peaks obtained, an internal calibration factor was determined in order to quantify how H_2 was consumed. Below shows sample calculations for the sample Mn0-Co_3O_4/SiO_2. Similar procedure was done for all samples.

Details of the experiment

Sample=Mn0-Co_3O_4/SiO_2

Sample mass=37 mg

Carrier=He (50 ml (NTP)/min)

Pulse gas =5%H_2/Ar (50 ml (NTP)/min)

Analysis Temp=40 C

Analysis Pressure= 1 atm

Loop Vol=0.31 ml

Table 8.5: Peaks obtained from 5% H_2/Ar pulse chemisorption.

Peak	Pulse (mVs)
1	**0.21708**
2	**0.21116**
3	**0.20393**
4	**0.20559**
5	**0.20482**
6	**0.20102**
7	**0.19754**
8	**0.20045**
9	**0.20895**
10	**0.20996**
11	**0.20678**
Total	**2.26728**

$$C_F = N_s V_{loop} X_{gas} P_{inj} / (RT_{inj} \times \textbf{total sum of last peaks area})$$

$$N_s = \textbf{number of last pulses with the same area} = 4$$

$$V_{loop} = 0.31ml$$

$$X_{gas} = 5\%$$

$$P_{inj} = 1\ atm$$

$$T_{inj} = 40\ ^{\circ}C$$

$$R = gas\ constant$$

$$C_F = 4 \times 0.00031l \times (0.05) \times \frac{1atm}{\frac{0.00008205\text{latm}}{\text{mmolK}} \times 313\text{K}} \times 2.26728mVs)$$
$$= 0.00108\ mmole/mVs$$

To quantify the amount of H_2 consumed during TPR, the total peak areas in each normalized H_2-TPR profile of Mn0-Co_3O_4/SiO_2 catalyst were calculated using Origin. The total area of the peaks shown in Figure 8.5 was 1005 mVs.

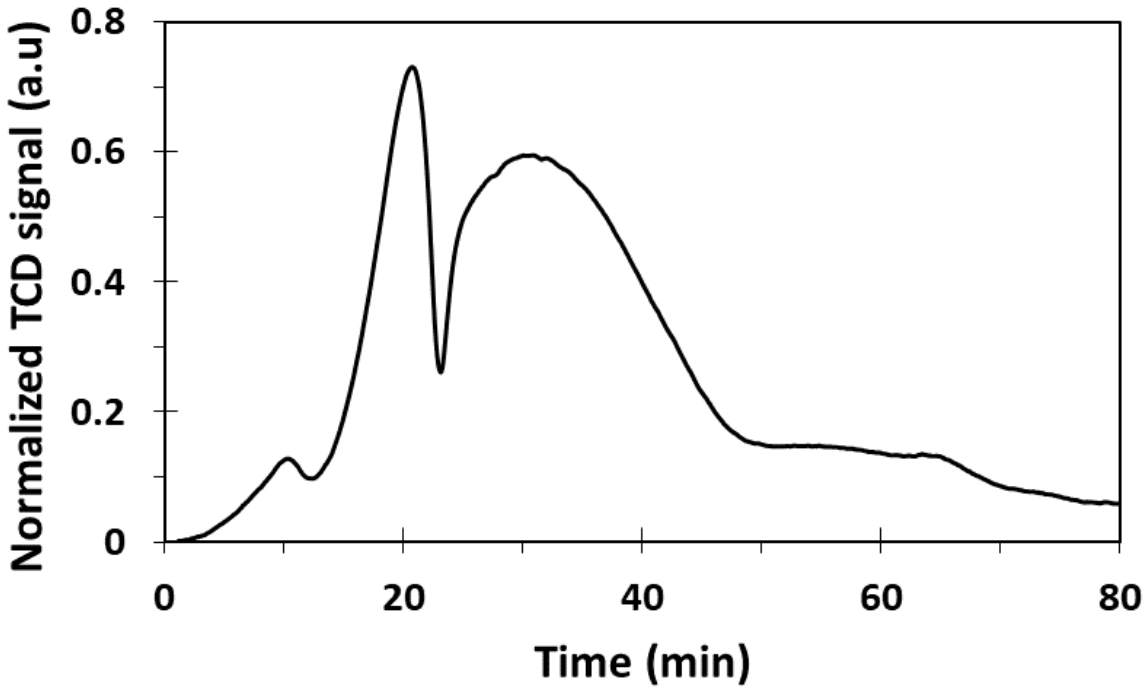

Figure 8.5: H_2-TPR profile of Mn0-Co/SiO_2.

To calculate the amount of H_2 consumed during TPR, the following equation was used:

$$n_{H_2\ consumed} = \frac{\boldsymbol{area\ under\ the\ curve\ (mVs)} \times \boldsymbol{C_F}}{\boldsymbol{Sample\ mass(\ g)}}$$

$$n_{H_2\ consumed} = \frac{\mathbf{1005\ (mVs)} \times \mathbf{0.00108}\frac{\boldsymbol{mmol}}{\boldsymbol{mVs}}}{\boldsymbol{g}}$$

$$n_{H_2\ consumed} = \mathbf{1.1}\frac{\boldsymbol{mmol}}{\boldsymbol{g}}$$

Similar procedure was followed for all Mn^{SEA}-Co/SiO_2 catalysts.

Appendix G: Quantifying amount of CO uptake during CO pulse chemisorption.

The CO uptake sample calculations were done for $Mn26^{SEA}$ -Co/SiO_2. Similar procedure was done for all Mn^{SEA}-Co/SiO_2 samples.

Internal Calibration Factor in Pulse chemisorption

Sample=$Mn26^{SEA}$ /Co/SiO_2

Sample mass=0.15 g

Carrier=He (50 ml (NTP)/min)

Pulse gas =CO (20 ml (NTP)/min)

Analysis Temp=40 C

Analysis Pressure= 101325 Pa

Loop Vol=0.31 ml

Number of pulses =80

Table 8.6: Peaks obtained from CO pulse chemisorption.

Peak	Pulse (mVs)
1	2.090256
2	5.952662
3	5.940787
4	5.953344
5	5.867226
6	5.957767
Total	31.76204

$$C_F = N_s V_{loop} X_{gas} P_{inj} / (RT_{inj} \times \textbf{total sum of last peaks area})$$

$$N_s = \textbf{number of last pulses with the area} = 5$$

$$V_{loop} = 0.31ml$$

$$X_{gas} = 1$$

$$C_F = 5 \times 0.00031l \times (1) \times \frac{1atm}{\frac{0.00008205\text{latm}}{\text{mmolK}} \times 313\text{K}} \times 31.76204221mVs)$$
$$= 0.002033879\ mmole/mVs$$

The same calculations were done for other samples and a summary of CFs is shown below.

Table 8.7: Internal calibration factors in CO pulse chemisorption for Mn^{SEA}-Co/SiO_2.

Catalysts	Calibration factor (mmol/mVs)
Mn0	0.002029
$Mn16^{SEA}$	0.002582
$Mn26^{SEA}$	0.002034
$Mn42^{SEA}$	0.002041
$Mn55^{SEA}$	0.002028
Average	0.002143

The average C_F was used to calculate adsorbed CO. The following equation was used to calculate the amount of CO adsorbed during CO pulse chemisorption. $CO\ uptake = ((N_T.A_{LP} - Total\ area\ of\ all\ peaks).CF)/sample\ mass$

Therefore, the amount of CO uptake for Mn26^{SEA}-Co/SiO_2 is:

$$CO\ uptake = (6 \times 5.9504 - 31.76204221).0.002143\ mmol/mVs)/0.15\ g$$
$$= 0.722\ mmol/g$$

Appendix H: Calculating peak areas for each peak in Mn-Co/SiO_2 CO-TPD profiles

The data presented below is data for Mn26^{SEA}-Co/SiO_2. Figure 8.6 shows the deconvolution of a normalized CO-TPD profile of Mn=0.26 wt.% using the gaussian method. The areas for the peaks are shown in Table 8.5 Similar procedure was done for all Mn^{SEA}-Co/SiO_2 catalysts.

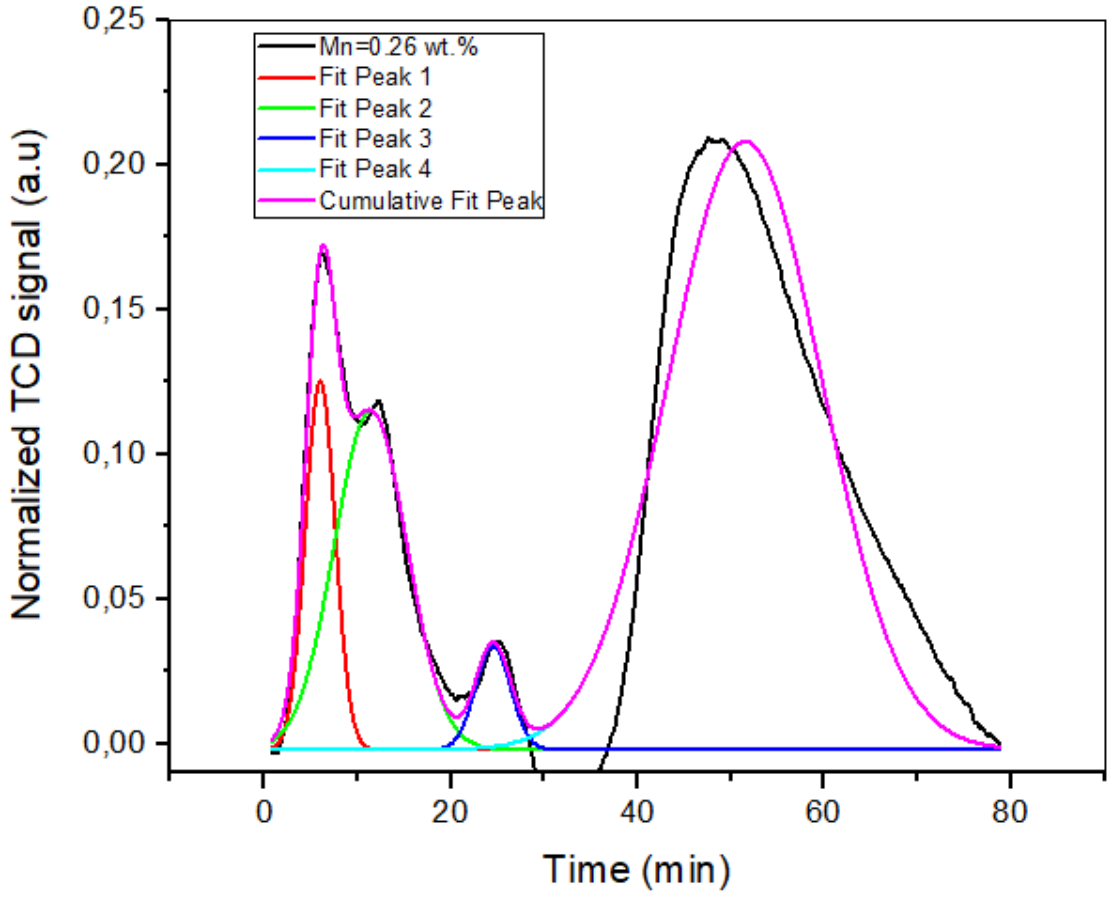

Figure 8.6: CO-TPD profile for Mn26^{SEA}-Co/SiO_2 showing deconvoluted peaks.

Table 8.8: A summary of peak areas (A) for $Mn26^{SEA}$-Co/SiO_2 obtained from a gaussian model.

Model	Gauss			
Equation	y=y0 + (A/(w*sqrt(PI/2)))*exp(-2*((x-xc)/w)^2)			
Plot	Peak1(B)	Peak2(B)	Peak3(B)	Peak4(B)
y0	-0,00191 ±	-0,00191 ±	-0,00191 ±	-0,00191 ±
xc	6,00213 ± 0	11,39909 ±	24,51147 ±	51,48762 ±
w	3,17964 ± 0	7,77667 ± 0	3,74747 ± 0	16,54243 ±
A	0,50671 ± 0	1,1395 ± 0,	0,16739 ± 0	4,35231 ± 0
Reduced	4,08014E-4			
R-Square(	0,91888			
Adj. R-Sq	0,91704			

Appendix I: Quantifying activation energy for CO desorbed from the catalyst surface.

The heat of desorption can be quantified using several methods such as Redhead analysis, complete/line analysis, leading edge analysis, Chan-Aris-Weinberg (CAW) to mention but a few (Redhead, 1962; Nieskens *et al.,* 2003; Chan & Weinberg, 1978). In this project, the Redhead analysis was used.

Redhead analysis

Below is an equation that was developed by Redhead, with the assumption that the CO desorption reaction is of first-order.

$$\frac{E_d}{RT_p} = \ln\frac{AT_p}{\beta} - 3.46$$

E_d is the activation energy, β is the heating rate (10 °C/min), T_p is the maximum peak temperature and R is the gas constant. This is a straight forward and routinely applied method of analysis and gives good estimates of E_d by $\mp$ 30% (Cvetanović & Amenomiya, 1967). The Redhead analysis method is often used to obtain activation energies from a single TPD spectrum hence an appropriate pre-exponential value (A) should be chosen, and it is normally 10^{13} s^{-1} (Schroeder & Gottfried, 2002).

Appendix J: GC-TCD raw data for Mn0-Co/SiO_2

	Area (a.u)						Selectivity	
Time (mins)	H_2	CO_2	N_2	CH_4	CO	X_{CO} (%)	CO_2 (C-%)	CH_4 (C-%)
42	58164770	77147	3788267	1772767	3522930	69.78813853	0.691868089	5.404356
84	78760588	63263	3652740	1857459	4698590	58.21091701	0.705428553	7.040614
126	66760781	51432	3591194	1557924	4015303	63.67601329	0.533267522	5.490932
168	54488779	27387	3540865	1106557	3243552	70.24050567	0.261080188	3.585843
210	80396351	28715	3736173	1354429	4673775	59.35988996	0.306983624	4.922103
252	69910638	29083	3688106	1188841	4260602	62.46973561	0.299290267	4.158773
294	89868720	35539	3709795	1473190	5417359	52.55922702	0.432148267	6.089398
336	97459686	35259	3634263	1556544	5814609	48.02216153	0.479003169	7.188162
378	77702727	29740	3812348	1250088	4695698	59.98510586	0.308341123	4.405743
420	66330557	20758	2609150	1016323	3991506	50.3005262	0.375007873	6.241294
462	64132849	20414	2460716	979036	3830310	49.43075347	0.397920066	6.487157
504	65054479	19772	2458110	997094	3893251	48.54528917	0.392851711	6.734451
546	64043122	20019	2438220	977897	3812564	49.20063249	0.395662834	6.56998
588	65480730	19871	2423123	983631	3893187	47.80320271	0.406737038	6.844067
630	64271574	21586	2424585	977899	3846800	48.45622234	0.435623859	6.70844
672	65079208	20507	2412097	973451	3871340	47.85885091	0.421183694	6.796285
714	64940692	21255	2409463	975940	3876402	47.73359866	0.438170488	6.839009
756	63750816	18133	2411101	946407	3812271	48.63321152	0.366646684	6.504952
798	64733610	20317	2396372	954487	3858829	47.68631069	0.421539303	6.731883
840	64509574	22289	2389152	950449	3869826	47.37868354	0.466863872	6.844067
882	65180342	20685	2382568	950246	3860459	47.36099258	0.434626175	6.70844
924	66244482	20176	2379948	961053	3957307	45.98102656	0.437134809	6.796285
966	65700689	18517	2376086	946888	3900943	46.66387	0.395962603	6.731883
1008	66002014	20785	2377042	947097	3939822	46.15395656	0.449190631	6.767317
1050	65920925	20402	2366537	941872	3924062	46.13128532	0.443088361	6.787103
1092	66024336	20953	2361465	947028	3955546	45.58245089	0.461523139	7.078084
1134	65484236	20383	2358122	925971	3878356	46.56873545	0.44008224	6.88288
1176	65746284	19006	2346878	970865	3867533	46.4625643	0.413260112	6.957659
1218	64958707	19598	2328346	913581	3864616	46.07714469	0.433116899	6.953405
1260	66577088	19801	2337076	933925	3956307	45.00398769	0.446364599	7.090847
1302	65667885	19648	2357635	916583	3901671	46.23642651	0.427350259	6.795965
1344	65667885	19648	2357635	916583	3901671	46.23642651	0.427350259	7.175954
1386	64932509	19440	2313576	925043	3787345	46.81794079	0.425526523	6.863229
1428	68589054	16458	2345036	948936	3861526	46.50373017	0.357821314	7.156533
1470	67644329	17842	2339094	930134	3839476	46.67408281	0.387477528	6.776812
1512	66030696	18956	2379290	855762	3812789	47.939367	0.394033801	6.776812
1554	70772843	17571	2399091	919144	4115551	44.26919478	0.392260509	6.883041
1596	60895757	15963	2361058	785940	3515039	51.63429264	0.310453156	7.013166
1638	71829926	18545	2473479	909976	4144812	45.5609346	0.390168711	6.866518
1680	74288538	22130	2492525	966708	4301578	43.93364392	0.479149587	6.046831
1722	72894493	21242	2519851	954415	4222602	45.55984674	0.438697078	6.975088
1764	73091580	21834	2503844	961028	4233576	45.069425	0.458744082	5.195879
1806	75208121	23166	2490543	1005057	4338380	43.40897025	0.5080471	6.507941
1834	73221266	20505	2470460	991800	4379357	42.41006678	0.448518878	7.11497
1876	70698273	20381	2435454	958253	4180301	44.23757214	0.460326924	6.700306
1918	70163427	21094	2428201	948509	4130003	44.74395647	0.465297092	6.863747
1960	70156467	20985	2411415	947506	4131153	44.34382278	0.485012235	7.492585
2002	70014198	21502	2392896	943104	4130149	43.92672172	0.493132021	7.629425
2044	69829038	21837	2384435	933656	4107801	44.03223556	0.458910152	7.16842
2086	69686784	20145	2375390	934529	4108041	43.81583935	0.440978937	7.236711
2156	62294896	20442	2304373	831019	3710019	47.69569842	0.426446062	6.093874
2170	64295535	19277	2310812	869861	3813922	46.38068712	0.426446062	5.404356

Appendix K: GC-TCD raw data for $Mn16^{SEA}$-Co/SiO_2

	Area (a.u)						Selectivity	
Time (mins)	H_2	CO_2	N_2	CH_4	CO	X_{CO} (%)	CO_2 (C-%)	CH_4 (C-%)
42	32724769	77247	3846453	778964	2056826	69.78813853	0.691868089	5.404356
84	45406907	118087	4022004	1543991	2991595	58.21091701	0.705428553	7.040614
126	44094049	120794	4006414	1701222	3001190	63.67601329	0.533267522	5.490932
168	45689419	137323	3970912	1916584	3222907	70.24050567	0.261080188	3.585843
210	41505069	107313	4003576	1576071	2882650	59.35988996	0.306983624	4.922103
252	46333973	115359	4072893	2321549	3235613	62.46973561	0.299290267	4.158773
294	52223168	107152	4069296	2375432	3555516	52.55922702	0.432148267	6.089398
336	52223168	107152	4069296	2375432	3555516	48.02216153	0.479003169	7.188162
378	49885166	90407	4121360	2082083	3383785	59.98510586	0.308341123	4.405743
420	64807075	96387	4111691	2458220	4151712	50.3005262	0.375007873	6.241294
462	50406863	80670	4077666	1988093	3382275	49.43075347	0.397920066	6.487157
504	70735537	99813	3951296	2607678	4611546	48.54528917	0.392851711	6.734451
546	45625872	61710	3892519	1631073	2978461	49.20063249	0.395662834	6.56998
588	66101092	91573	3873331	2377319	4424925	47.80320271	0.406737038	6.844067
630	67911846	86405	3861053	2328571	4420154	48.45622234	0.435623859	6.70844
672	56382946	70286	3898906	1914901	3678766	47.85885091	0.421183694	6.796285
714	63508163	76394	3850566	2146453	4190777	47.73359866	0.438170488	6.839009
756	60488241	70094	3864395	1981331	3920646	48.63321152	0.366646684	6.504952
798	57395019	68408	3890370	1864310	3732517	47.68631069	0.421539303	6.731883
840	59537279	65669	3872539	1866534	3797432	47.37868354	0.466863872	6.844067
882	69200697	70776	3822013	2072732	4264227	47.36099258	0.434626175	6.70844
924	68807004	67628	3756152	1435131	4321142	45.98102656	0.437134809	6.796285
966	67248333	63026	3735668	1350144	4120098	46.66387	0.395962603	6.731883
1008	67248333	63026	3735668	1350144	4120098	46.15395656	0.449190631	6.767317
1050	58707734	53622	3758507	1157082	3254779	46.13128532	0.443088361	6.787103
1092	77818757	64623	3712278	1453745	4114963	45.58245089	0.461523139	7.078084
1134	65743449	53791	3730595	1225777	3926538	46.56873545	0.44008224	6.88288
1176	60333126	54316	3770106	1152282	3680225	46.4625643	0.413260112	6.957659
1218	77151379	65506	3717230	1447098	4653054	46.07714469	0.433116899	6.953405
1260	67272397	57402	3768491	1271896	4169949	45.00398769	0.446364599	7.090847
1302	59611760	50057	3795566	1095001	3599290	46.23642651	0.427350259	6.795965
1344	70825613	66712	3697638	1403559	4459563	46.23642651	0.427350259	7.175954
1386	70350708	57776	3702872	1280843	4258104	46.81794079	0.425526523	6.863229
1428	64536066	48359	3942354	1092251	3832557	46.50373017	0.357821314	7.156533
1470	69219537	52446	3934115	1177873	4093218	46.67408281	0.387477528	6.776812
1512	77734795	60300	3755696	1353333	4676375	47.939367	0.394033801	6.776812
1554	73411007	55633	3926244	1269918	4340579	44.26919478	0.392260509	6.883041
1596	74095623	58742	3916196	1302735	4417646	51.63429264	0.310453156	7.013166
1638	64801818	53026	3912594	1166985	3931185	45.5609346	0.390168711	6.866518
1680	82768918	63890	3843919	1424824	4899265	43.93364392	0.479149587	6.046831
1722	78394502	59658	3760882	1332656	4401745	45.55984674	0.438697078	6.975088
1764	59670904	49058	3787695	1060935	3652245	45.069425	0.458744082	5.195879
1806	85611691	66365	3766134	1459742	5165572	43.40897025	0.5080471	6.507941
1834	64958999	50587	3764327	1105463	3909508	42.41006678	0.448518878	7.11497
1876	66602444	51093	3770955	1113333	3939088	44.23757214	0.460326924	6.700306
1918	69806546	50899	3760847	1111050	4134109	44.74395647	0.465297092	6.863747
1960	65932230	48379	3769825	1062474	3883666	44.34382278	0.485012235	7.492585
2002	78595448	56375	3711288	1229358	4613928	43.92672172	0.493132021	7.629425
2044	70427666	51987	3761756	1141622	4197151	44.03223556	0.458910152	7.16842
2086	67654137	50246	3747333	1074420	3986177	43.81583935	0.440978937	7.236711
2156	67780226	50510	3753262	1072798	4039965	47.69569842	0.426446062	6.093874
2170	70165070	50085	3752389	1095638	4108498	46.38068712	0.426446062	5.404356

Appendix L: GC-TCD raw data for $Mn26^{SEA}$-Co/SiO_2

	Area (a.u)						Selectivity	
Time (mins)	H_2	CO_2	N_2	CH_4	CO	X_{CO} (%)	CO_2 (C-%)	CH_4 (C-%)
42	56381448	18283	4112297	791938	3384780	73.39416082	0.142904158	2.10415
84	49100205	59248	4088762	1367974	3247317	74.32775536	0.459911464	3.609661
126	52317863	59248	4044586	1768604	3531924	71.77276987	0.4814856	4.885716
168	58708532	73766	4069031	1935093	3840294	69.49265148	0.61541736	5.487865
210	73733547	87224	3998101	2410598	5089918	58.848278	0.874564548	8.216156
252	64078215	62012	3958262	1941807	4330642	64.63458695	0.571807192	6.086505
294	74787983	62333	4193874	2065397	4834271	62.73967812	0.558860937	6.294733
336	72310138	52959	4194168	1895855	4676980	63.95453117	0.465764113	5.667864
378	74424810	57780	4205559	2009037	4921512	62.17265969	0.521312034	6.161638
420	79588387	57006	4200508	2060921	5203465	59.95744232	0.533972688	6.562176
462	80555324	46808	4439292	1995381	5172390	62.33755248	0.399024917	5.782209
504	85010292	52447	4418492	1995381	5596813	59.05529826	0.474166755	6.132313
546	73891155	39944	4287064	1726345	4732130	64.31976646	0.341735831	5.020588
588	82554849	38732	4252027	1791390	5082464	61.36247618	0.350198614	5.505829
630	78438540	37668	4311923	1747887	5051123	62.13413034	0.331676522	5.231709
672	84522911	39125	4315385	1813161	5321253	60.14109637	0.355636929	5.602436
714	96122705	42289	4371329	2050257	6230311	53.92904442	0.42318921	6.974346
756	96122705	42289	4371329	2050257	6230311	53.92904442	0.42318921	6.974346
798	95081637	40940	4384313	1991518	6191911	54.34859561	0.405323095	6.70233
840	1.01E+08	36994	4391412	1982619	6221876	54.20182676	0.366654124	6.679633
882	92505592	32955	4416770	1765895	5641276	58.71392928	0.299791128	5.460726
924	1.04E+08	37319	4467589	2004494	6476506	53.14040318	0.3708304	6.973981
966	1.09E+08	35695	4476851	2052086	6704385	51.59198285	0.364582582	5.61787
1008	90214383	33447	4564211	1829746	6039849	57.22486822	0.302099527	6.442042
1050	1.03E+08	35965	4612232	1981954	6635996	53.49218254	0.343891936	5.909605
1092	1.06E+08	33472	4676002	1914429	6429077	55.55684033	0.303957474	6.35124
1134	1.17E+08	35115	4758057	2118250	6445621	56.2108905	0.309731914	6.38733
1176	99871920	39975	4738501	2141970	6339743	56.75243456	0.350676278	5.532935
1218	1.03E+08	30565	4880383	1927275	6456633	57.23552112	0.093305615	5.379406
1260	1.11E+08	32010	4940038	1937002	6349696	58.45166429	0.261518185	5.97625
1302	1.19E+08	32417	5104222	2104258	7055441	55.31872085	0.270841073	5.432099
1344	1.15E+08	30597	5216001	2039501	6821963	57.72314407	0.239736738	5.061086
1386	1.17E+08	26360	5355388	1967278	6924385	58.20529597	0.199496533	4.828162
1428	1.15E+08	29132	5542122	1995125	6893769	59.79207758	0.207392939	5.95071
1470	1.25E+08	32151	5420930	2207196	7568581	54.86934339	0.254996555	4.944227
1512	1.5E+08	24763	5894273	1879891	8802055	51.72916411	0.191593574	5.702204
1554	1.15E+08	27510	5623868	2339722	7218798	58.50834491	0.197233667	6.763709
1596	1.34E+08	30033	5823500	2664657	8242130	54.25049824	0.224261279	6.690023
1638	1.25E+08	31323	5998185	2630365	8802055	52.56540359	0.23436183	5.871187
1680	1.14E+08	28955	5433378	2291220	7127416	57.59733273	0.218270311	6.043289
1722	1.34E+08	29924	5454422	2570309	8394944	50.24920143	0.257563985	7.130362
1764	1.23E+08	27276	5511995	2289376	7653909	55.11456196	0.211811188	5.896245
1806	1.37E+08	25396	5484747	2453225	8432356	50.30378391	0.21714581	6.758775
1834	1.26E+08	25043	5585633	2238844	7859954	54.51391115	0.194021565	6.538296
1876	1.37E+08	23042	5561337	2374006	8490810	50.64843852	0.19298266	6.227118
1918	1.39E+08	25078	5628376	2339756	8534317	50.98639391	0.206157381	6.021428
1960	1.37E+08	24667	5651019	2274345	8421322	51.82912953	0.198682237	5.983877
2002	1.36E+08	24019	5700386	2245667	8382684	52.46540276	0.189461528	6.364676
2044	1.35E+08	24515	5754774	2257775	8442681	52.57764737	0.191137484	6.305173
2086	1.4E+08	25205	5761402	2314417	8802443	50.61375225	0.203907583	5.03918
2156	1.44E+08	24456	5787214	2364699	8599319	51.96857117	0.19183087	5.205071
2170	1.42E+08	23848	5675582	1863370	8384579	52.24686958	0.18972505	5.03918

Appendix M: GC-TCD raw data for Mn42^{SEA}-Co/SiO_2

	Area (a.u)						Selectivity	
Time (mins)	H_2	CO_2	N_2	CH_4	CO	X_{CO} (%)	CO_2 (C-%)	CH_4 (C-%)
42	70827126	0	2994989	676306	3906459	57.83821132	0	3.130867
84	61910443	7225	2821088	776355	3554076	59.27687802	0.101924663	3.722973
126	79973747	19225	3019270	1216853	4438361	52.48271047	0.286214433	6.158165
168	79220572	18665	3084448	1201020	4414312	53.73883549	0.265647467	5.810533
210	78326299	16576	3108440	1144287	4474127	53.47388316	0.235255029	5.520548
252	78071200	14719	3126161	1037274	4552491	52.92733966	0.2098603	5.027285
294	82419962	14709	3173439	1048623	4756720	51.54836672	0.212119929	5.140505
336	87928580	11118	3078832	1058499	4787865	49.73254556	0.171294484	5.543642
378	96197058	0	3611007	992071	5610313	49.77849198	0	4.425926
420	1.07E+08	10159	3162863	1143715	5978936	38.89531464	0.194812437	7.455411
462	96295020	9073	3289752	1061565	5458557	46.36532191	0.140325908	5.581123
504	93908035	10168	3334443	1045836	5391741	47.7319001	0.150711678	5.269422
546	1.01E+08	9704	3222907	1089030	5757075	42.25889353	0.168084738	6.412175
588	98101867	9746	3423457	1037345	5620849	46.92768529	0.143111913	5.177983
630	96162814	8903	3287845	984691	5404712	46.86358994	0.136311618	5.12489
672	1.07E+08	11025	3643065	1080832	5672028	49.67283875	0.143726248	4.789649
714	99632923	9271	3244394	1004027	5644001	43.76787693	0.154021341	5.670061
756	1E+08	8458	3284639	978642	5636851	43.41988327	0.136426207	5.365893
798	1.01E+08	8993	3250892	971064	5690303	43.40479581	0.136179769	5.516811
840	1.03E+08	8331	3324989	947119	5821553	43.40479581	0.136179769	5.262693
882	1.03E+08	8331	3324989	947119	5821553	42.41982871	0	5.262693
924	1.05E+08	0	3272038	933815	5828547	44.64342815	0.091394008	5.395169
966	1.02E+08	5778	3340763	913406	5721157	41.89220653	0	4.911251
1008	1.08E+08	0	3393835	959790	6100903	41.2299612	0	5.413569
1050	1.12E+08	0	3417275	961533	6213051	37.5143408	0.178589706	5.472714
1092	1.18E+08	0	3562518	1014456	6886625	37.82785538	0	6.087098
1134	1.07E+08	8849	3090078	956015	5943391	37.93631009	0	6.558658
1176	1.14E+08	0	3305757	946310	6347132	39.43717074	0	6.051163
1218	1.2E+08	0	3606348	943152	6756827	39.18239453	0	5.317895
1260	1.24E+08	0	3684725	980566	6932716	37.56403344	0	5.446434
1302	1.3E+08	0	3733719	1023568	7211830	41.28510906	0	5.852404
1344	1.19E+08	0	3753397	945354	6817761	39.92023499	0	4.892242
1386	1.26E+08	0	3785970	969899	7036787	36.13263261	0	5.146212
1428	1.32E+08	0	3804311	1014665	7516645	40.25038382	0	5.919411
1470	1.19E+08	0	3680983	936889	6804057	39.83870201	0	5.070908
1512	1.15E+08	0	3501156	877396	6516249	37.69914916	0	5.044411
1554	1.22E+08	0	3613221	911766	6963980	36.72169547	0	5.367706
1596	1.2E+08	0	3485077	889043	6822385	38.07252964	0	5.57082
1638	1.19E+08	0	3523087	898749	6749564	38.03019438	0	5.373222
1680	1.2E+08	0	3557114	902392	6819412	37.11704079	0	5.585689
1722	1.22E+08	0	3569967	922960	6944903	36.74146386	0	5.650448
1764	1.22E+08	0	3570952	924468	6988310	38.5569662	0	5.243992
1806	1.21E+08	0	3603333	908527	6849298	37.66027214	0	5.327596
1834	1.23E+08	0	3616296	904789	6974256	38.06753478	0	5.293878
1876	1.23E+08	0	3659355	919606	7011193	37.71377169	0	5.466821
1918	1.22E+08	0	3608795	913258	6953817	36.95911681	0	5.536272
1960	1.24E+08	0	3638725	935519	7096440	36.73921334	0	5.417163
2002	1.26E+08	0	3638685	922912	7121116	37.71017566	0	5.52825
2044	1.25E+08	0	3693742	940948	7117913	36.90123462	0	5.35071
2086	1.25E+08	0	3649417	928369	7123827	37.85082147	0	5.575001
2156	1.24E+08	0	3649417	921677	7016619	36.75740774	0	5.444116
2170	1.42E+08	23848	5675582	1863370	8384579	36.72842625	0	5.444116

Appendix N: GC-TCD raw data for $Mn55^{SEA}$-Co/SiO_2

	Area (a.u)						Selectivity	
Time (mins)	H_2	CO_2	N_2	CH_4	CO	X_{CO} (%)	CO_2 (C-%)	CH_4 (C-%)
42	1.15E+08	0	4192763	1783194	6564704	49.3888946	0	6.905584
84	1.28E+08	9202	4136335	1971651	7295565	42.98695791	0.122088063	8.892197
126	1.13E+08	0	4205505	1698442	6430859	50.57100024	0	6.404164
168	63798912	0	4113960	1048445	3725905	70.72460921	0	2.889658
210	1.18E+08	0	4137467	1701402	6667524	47.90919931	0	6.883113
252	42519042	0	2331678	630599	2545058	64.7174393	0	3.351157
294	63798912	0	4137467	1048445	3725905	70.89093721	0	2.866499
336	1.18E+08	0	4137467	1701402	6667524	47.90919931	0	6.883113
378	42519042	0	2331678	630599	2545058	64.7174393	0	3.351157
420	79254068	0	2397994	1042109	4594028	38.07350014	0	9.153215
462	72837319	0	2465574	956041	**4229024**	44.55618619	0	6.978818
504	75899788	0	2383202	1002440	4411231	40.16849401	0	8.397372
546	76201795	0	2399409	1011063	4346315	41.44716824	0	8.15287
588	78162324	0	2410972	1037336	4474829	40.00497128	0	8.624715
630	76808865	0	2397140	1011408	4382505	40.90373823	0	8.673446
672	77998332	0	2384545	1020609	4457682	39.5725108	0	8.614766
714	78554284	0	2384850	1010088	4469039	39.42630527	0	8.042708
756	76326754	0	2378613	977675	4342828	40.98263308	0	8.235091
798	77815226	0	2385672	984987	4413090	40.20525207	0	8.421964
840	78415083	0	2392964	994807	4472563	39.58409437	0	8.326685
882	77942435	0	2383168	983096	4443618	39.72835472	0	8.837333
924	79953487	0	2387246	1006018	4561135	38.24007774	0	8.373043
966	79774812	0	2392505	995842	4450955	39.86444302	0	7.947506
1008	78067668	0	2393481	974091	4363887	41.06483547	0	8.367638
1050	79870194	0	2392021	991869	4459331	39.73908664	0	8.159685
1092	79764711	0	2389117	972844	4433245	40.01877893	0	8.408858
1134	80225273	0	2379960	982313	4464627	39.36177059	0	8.078224
1176	78486917	0	2363989	962545	4357310	40.41952027	0	8.613478
1218	80668104	0	2367140	983564	4490210	38.68401676	0	8.63527
1260	83187761	0	2433314	1005370	4639430	38.36924899	0	7.676949
1302	79897983	0	2439885	957491	4453926	40.99285145	0	8.259619
1344	82764782	0	2444108	992595	4579830	39.42966811	0	8.386374
1386	82764782	0	2439919	1013258	4550807	39.71017867	0	9.141017
1428	84502083	0	2442193	1053184	4696937	37.83216529	0	8.107379
1470	85964071	0	2539785	996799	4806972	38.82054177	0	8.269896
1512	84077551	0	2512443	1023965	4700833	39.52030483	0	8.340247
1554	86674571	0	2537181	1022832	4806644	38.76192991	0	8.095505
1596	86371864	0	2549915	999727	4824864	38.83677723	0	8.576635
1638	92121131	0	2572208	1069178	4864802	38.86497803	0	7.862948
1680	88965633	0	2658237	1021816	4999668	39.2035171	0	8.35961
1722	88753481	0	2641436	1065352	5010033	38.68997654	0	8.173586
1764	78141060	0	2413532	968176	4527975	39.3568227	0	7.664157
1806	79698477	0	2473979	939458	4612608	39.73272886	0	7.773764
1834	81951982	0	2467281	950400	4599844	39.73634375	0	8.199806
1876	83181318	0	2456029	963850	4681930	38.37989783	0	8.04669
1918	83217394	0	2456747	969397	4611560	39.32379396	0	8.42456
1960	85934675	0	2459843	994988	4679832	38.50300965	0	7.922881
2002	81911821	0	2430205	942349	4567439	39.24796442	0	7.925541
2044	81887106	0	2438986	942006	4596668	39.07930934	0	8.268869
2086	82617214	0	2432191	972681	4606045	38.78448778	0	8.121189
2156	83114950	0	2430888	945494	4631997	38.40658158	0	8.083419
2170	82430502	0	2408825	932500	4590126	38.40430701	0	8.114912

Appendix O: GC-TCD raw data for $Mn16^{IMPR}$-Co/SiO_2

	Area (a.u)						Selectivity	
Time (mins)	H_2	CO_2	N_2	CH_4	CO	X_{CO} (%)	CO_2 (C-%)	CH_4 (C-%)
42	84742578	0	2704981	447589	3257642	61.07127992	0	2.172749
84	73772169	0	2838587	484018	2982546	66.03622701	0	12.75951
126	50452905	24636	2900212	572242	2210605	75.36160627	0.265909402	2.099574
168	47810075	57151	2966841	796653	2233183	75.66894002	0.600558477	2.845697
210	48889024	65145	2936320	851922	2293221	74.75510811	0.700132473	3.11234
252	52042490	63468	3833931	1969631	3379615	71.50596688	0.546149609	5.761423
294	56064074	52761	3857342	1912690	3579200	70.00638524	0.460925365	5.680025
336	56854354	50480	3898214	1828617	3646297	69.76448631	0.437887611	5.392052
378	60591604	46134	3936422	1861633	3854117	68.35141975	0.404497005	5.548509
420	59402456	39788	3933810	1753845	3730852	69.34328408	0.344094486	5.155904
462	60270794	40888	3929477	1747401	3783380	68.87737636	0.35639197	5.177411
504	62108710	38603	3885739	1730545	3868419	67.20887898	0.345569438	5.266053
546	63452384	35624	3881155	1712459	3937189	66.79908616	0.322179893	5.264583
588	64402701	34952	3861929	1679762	3966645	65.63252908	0.319624907	5.221609
630	66316093	32793	3844411	1692628	4087393	65.41297071	0.306602427	5.379526
672	68139008	32703	3931051	1701382	4206210	64.42268647	0.300025683	5.30592
714	69274077	32824	3883752	1688631	4274582	64.90133326	0.30948854	5.412225
756	69635343	31547	3928669	1660143	4265845	64.32230311	0.294506191	5.221291
798	70287013	30203	3899947	1650810	4304518	64.08112078	0.282797994	5.277257
840	71243502	30133	3922648	1657532	4358842	64.22479546	0.297816794	5.287908
882	71593364	31781	3919756	1647933	4338206	63.36774346	0.28989189	5.249395
924	72707780	30415	3905952	1673447	4426491	62.65318763	0.305668878	5.421859
966	74118621	31842	3922377	1699058	4531812	63.1923942	0.279725014	5.544305
1008	73749354	29552	3943975	1677120	4490976	63.7253849	0.258769322	5.396306
1050	74286765	28180	4031430	1652804	4524087	62.47251723	0.273335005	5.159186
1092	75539521	28646	3957520	1658201	4594535	62.01021364	0.270634456	5.378442
1134	77848412	28523	4009519	1676720	4712248	62.41672867	0.273283435	5.407997
1176	82446080	29269	4047967	1762536	4706527	62.24693393	0.248068296	4.344231
1218	77720868	26357	4026708	1357843	4702961	61.16562572	0.271420771	5.431543
1260	81057062	28481	4047139	1676669	4862207	61.28410702	0.259380175	5.37048
1302	79506956	27041	4013114	1647066	4806620	62.02483067	0.247431482	5.122588
1344	78649044	26190	4025857	1595078	4729629	61.30793116	0.264575737	5.350112
1386	79542279	27406	3985863	1630311	4771043	62.02325336	0.223548179	5.233087
1428	82994969	23674	4027999	1630311	4732342	60.57930188	0.248930863	5.563174
1470	87934471	26031	4072220	1711381	4966204	62.11883638	0.219236095	4.949688
1512	81233060	23850	4131392	1584040	4841598	62.17193353	0.225998452	4.978753
1554	82155123	25340	4254516	1642229	4978899	61.91242366	0.236795769	5.115178
1596	84547566	26944	4335645	1712225	5108649	58.34107481	0.290248821	5.960654
1638	97320574	32700	4555607	1975528	5871152	61.44676827	0.275325438	5.470762
1680	91877684	33506	4672191	1958556	5572504	61.22070176	0.284483351	5.60094
1722	89967584	33550	4544444	1943160	5451923	66.60780112	0.24411947	5.04351
1764	72494713	29161	4230759	1620573	4370512	60.9044321	0.26653906	5.017617
1806	92012385	31708	4607894	1900263	5573128	63.15283632	0.250536609	4.507755
1834	88275032	31000	4622118	1826417	5268829	65.43297985	0.226182862	5.21195
1876	81003528	28890	4605052	1693792	4924538	61.71493928	0.268552862	6.703088
1918	89537774	32258	4591565	1841704	5438249	55.23100329	0.338525402	5.772484
1960	1.04E+08	36150	4561183	2105736	6317189	58.44779976	0.278350683	6.140027
2002	98289673	31298	4538366	1909409	5833948	56.56063095	0.30086062	4.828006
2044	1.01E+08	32718	4535765	1964281	6095412	61.91178595	0.236742692	5.485691
2086	89918659	28446	4578410	1706571	5394787	58.72149769	0.268735646	4.914061
2156	99062932	30555	4567760	1834849	5833057	61.17441078	0.242294877	4.771195
2170	93052074	28776	4579940	1716875	5501066	61.77030787	0.247939991	4.914767

Appendix P: GC-TCD raw data for $Mn26^{IMPR}$-Co/SiO_2

	Area (a.u)						Selectivity	
Time (mins)	H_2	CO_2	N_2	CH_4	CO	X_{CO} (%)	CO_2 (C-%)	CH_4 (C-%)
42	75224262	140889	3923785	1100544	4180367	65.56181962	1.29200524	2.172749
84	80543726	89842	3985070	1225371	4590414	62.76538314	0.84735747	12.75951
126	82232499	89754	4227224	131099	4718771	63.91683466	0.783658198	2.099574
168	83577135	91308	4204190	1323131	4760843	63.39566568	0.808184131	2.845697
210	78410919	86801	3909183	1293883	4436818	63.3126282	0.827354769	3.11234
252	85155186	94293	4407136	2342314	5326361	60.93344338	0.828343883	5.761423
294	88762979	80738	4335967	2246145	5436886	59.46826011	0.738669515	5.680025
336	80433872	67659	4316549	1999340	5037546	62.27638204	0.593757235	5.392052
378	73073828	57978	4357471	1775270	4541951	66.30705854	0.473382667	5.548509
420	80874331	60948	4359631	1933856	5028552	62.71585384	0.525866829	5.155904
462	75610684	55760	4393730	1769645	4655979	65.74620962	0.45536754	5.177411
504	96847957	62562	4466202	2190820	5880821	57.43716111	0.575337505	5.266053
546	86923317	56281	4444129	1981493	5399948	60.72339788	0.491997021	5.264583
588	81142578	49829	4527680	1793983	4977482	64.4642929	0.402745423	5.221609
630	93568872	57474	4550264	2068672	5821647	58.64383476	0.508107795	5.379526
672	86094465	50060	4626826	1857458	5277881	63.12708987	0.404329379	5.30592
714	1.13E+08	59456	4684883	2392496	6898481	52.40232805	0.571333575	5.412225
756	1.04E+08	56863	4735647	2212196	6445103	56.00720769	0.505766332	5.221291
798	97415221	50051	4781192	2037439	6011446	59.35812326	0.574464929	5.277257
840	1.19E+08	59592	4817623	2460552	7333251	50.79664385	0.554601435	5.287908
882	1.21E+08	58106	4884688	2464022	7465121	50.599538	0.37068287	5.249395
924	98614683	47407	4963073	1973806	6020266	60.79007552	0.433565941	5.421859
966	1.08E+08	52356	5007890	2170027	6679583	56.88528118	0.433565941	5.544305
1008	1.11E+08	49880	5039712	2217646	6875124	55.90332895	0.366828466	5.396306
1050	1.04E+08	47022	5096161	2069620	6410516	59.33873958	0.431916641	5.159186
1092	1.21E+08	50728	5166496	2322438	7411684	53.62843155	0.380182384	5.378442
1134	1.26E+08	46091	5285723	2301713	7504270	54.10820556	0.345348986	5.407997
1176	1.26E+08	44192	5431180	2232807	7463140	55.58206334	0.36074853	4.344231
1218	1.24E+08	49428	5623057	2311313	7396124	57.48299285	0.343647348	5.431543
1260	1.3E+08	49208	5885861	2361058	7758250	57.39262714	0.343647348	5.37048
1302	1.3E+08	49208	5885861	2361058	7758250	57.39262714	0.451738955	5.122588
1344	1.55E+08	55115	5905887	2843334	9366461	48.73495012	0.407746872	5.350112
1386	1.4E+08	51810	5804377	2609450	8683299	51.64291298	0.408347612	5.233087
1428	1.48E+08	53413	6056312	2742544	9189842	50.95092827	0.401288863	5.563174
1470	1.59E+08	49858	5919480	2799508	9245154	49.51509068	0.332919521	4.949688
1512	1.43E+08	48063	6167586	2518769	8544057	55.22043078	0.284846377	4.978753
1554	1.38E+09	42312	6195286	2388636	8325053	56.5633188	0.344621695	5.115178
1596	1.38E+08	46965	5925681	2437318	8385991	54.25463343	0.330634406	5.960654
1638	1.35E+08	47062	5987467	2404700	8134968	56.0818837	0.293352741	5.470762
1680	1.42E+08	40682	6033553	2373199	8544582	54.22285765	0.319122485	5.60094
1722	1.29E+08	43833	5785420	2269841	7873626	56.00828658	0.340782273	5.04351
1764	1.39E+08	44706	5831766	2417543	8467181	53.06792647	0.310189451	5.017617
1806	1.36E+08	42331	5881600	2341539	8235875	54.73680051	0.31084454	4.507755
1834	1.35E+08	42587	5898873	2326795	8250196	54.79086388	0.293518123	5.21195
1876	1.4E+08	43197	5922110	2365871	8480267	53.71246595	0.277776903	6.703088
1918	1.39E+08	39763	5888775	2308217	8330898	54.27035347	0.331551522	5.772484
1960	1.38E+08	39100	6000436	2288090	8290257	55.34026165	0.299008866	6.140027
2002	1.57E+08	42210	5967318	2590744	9169396	50.33018582	0.323546327	4.828006
2044	1.46E+08	40877	6087725	2413072	8856027	52.97650612	0.319660196	5.485691
2086	1.6E+08	42586	6146099	2644021	9407780	50.52126477	0.316622764	4.914061
2156	1.59E+08	43867	6293376	2636459	9454156	51.44096217	0.289950427	4.771195
2170	1.68E+08	43193	6371069	2703643	9753788	50.51290146	0.264905551	4.914767

Appendix Q: Data obtained from GC-FID analysis for Mn0-Co/SiO_2

Name	Time [Min]	Area [uV.Min]	C_N	RF	n_i	A_i/C_N	Molar flow rate (mmol C/min)	Selectivity
Methane	1.07	2803.9	1	1	2803.9	2803.9	0.029506057	7%
Ethylene	1.48	71.5	2	1	71.5	35.75	0.00075241	0%
Ethane	1.82	311	2	1	311	155.5	0.003272721	1%
Propene	4.24	726	3	1	726	242	0.007639858	2%
Propane	4.45	369.4	3	1	369.4	123.1333	0.003887278	1%
2-Methyl-1-propane	7.26	9.8	4	1	9.8	2.45	0.000103128	0%
Butene	8.17	806.1	4	1	806.1	201.525	0.008482768	2%
Butane	8.57	540.2	4	1	540.2	135.05	0.005684644	1%
Trans-2-butene	9.15	19.1	4	1	19.1	4.775	0.000200994	0%
Cis-2-butene	9.86	32	4	1	32	8	0.000336743	0%
Ethanol	11.5	140	2	1.3	182	91	0.001915226	0%
3-Methyl-1-Butene	12.73	3.5	5	1	3.5	0.7	3.68313E-05	0%
3-Methyl-Butane	13.25	7.1	5	1	7.1	1.42	7.47149E-05	0%
Pentene	13.85	678.9	5	1	678.9	135.78	0.007144214	2%
Pentane	14.32	604.3	5	1	604.3	120.86	0.006359182	1%
Trans-2-pentene	14.73	24.3	5	1	24.3	4.86	0.000255714	0%
Cis-2-pentene	15.39	2.1	5	1	2.1	0.42	2.20988E-05	0%
2-Methyl-butane	16.86	2.6	5	1	2.6	0.52	2.73604E-05	0%
2-Me-2-butene	17.69	0.7	5	1	0.7	0.14	7.36625E-06	0%
Propanol	18.34	55	3	1	55	18.33333	0.000578777	0%
3-Methyl-pentane	18.79	0.9	6	1	0.9	0.15	9.4709E-06	0%
Hexene	19.39	576.7	6	1	576.7	96.11667	0.006068741	1%
Hexane	19.66	681.8	6	1	681.8	113.6333	0.007174731	2%
Trans-2-hexene	20.15	26.7	6	1	26.7	4.45	0.00028097	0%
Cis-2-hexene	22.19	26.9	6	1	26.9	4.483333	0.000283075	0%
Butanol	23.44	42.9	4	1	42.9	10.725	0.000451446	0%
2-Methyl-hexane	24.06	2.6	7	1	2.6	0.371429	2.73604E-05	0%
3-Methyl-hexane	24.63	5.9	7	1	5.9	0.842857	6.2087E-05	0%
Heptene	24.86	437.4	7	1	437.4	62.48571	0.004602856	1%
Heptane	25.29	715.9	7	1	715.9	102.2714	0.007533573	2%

Appendix Q: Data obtained from GC-FID analysis for Mn0-Co/SiO_2 (continuation)

Name	Time [Min]	Area [uV.Min]	C_N	RF	n_i	A_i/C_N	Molar flow rate (mmol C/min)	Selectivity
Trans-2-heptene	27.17	31.7	7	1	31.7	4.528571	0.000333586	0%
Cis-2-heptene	27.86	30.7	7	1	30.7	4.385714	0.000323063	0%
Pentanol	28.49	29.9	5	1	29.9	5.98	0.000314644	0%
4-Methyl-heptane	28.97	6.2	8	1	6.2	0.775	6.5244E-05	0%
3-Methyle-heptane	29.58	0.8	8	1	0.8	0.1	8.41858E-06	0%
Octene	29.74	295.3	8	1	295.3	36.9125	0.003107507	1%
Octane	30.24	658.8	8	1	658.8	82.35	0.006932697	2%
Trans-2-octene	33.3	27.7	8	1	27.7	3.4625	0.000291493	0%
Cis-2-octene	34.24	33.4	8	1	33.4	4.175	0.000351476	0%
2-Methyl-octane	34.73	5.2	9	1	5.2	0.577778	5.47207E-05	0%
4-Methyl-octane	35.44	0.9	9	1	0.9	0.1	9.4709E-06	0%
Nonene	35.59	171	9	1	171	19	0.001799471	0%
Nonane	36.2	520.4	9	1	520.4	57.82222	0.005476284	1%
Trans-2-nonane	41.44	19.9	9	1	19.9	2.211111	0.000209412	0%
Cis-2-nonane	42.16	22.9	9	1	22.9	2.544444	0.000240982	0%
Methyl-nonane	42.9	1.8	10	1	1.8	0.18	1.89418E-05	0%
Decene	46.26	93.5	10	1	93.5	9.35	0.000983921	0%
Decane	47.11	414	10	1	414	41.4	0.013069839	0%
Undecane	47.64	64.1	11	1	64.1	5.827273	0.002023615	0%
Undecene	52.03	475.4	11	1	475.4	43.21818	0.015008217	0%
Dodecane	56.36	53.6	12	1	53.6	4.466667	0.001692134	0%
Dodecane	60.3	452.1	12	1	452.1	37.675	0.014272643	0%
Tridecane	60.44	248	13	1	248	19.07692	0.007829276	0%

Appendix R: Data obtained from GC-FID analysis for $Mn16^{SEA}$-Co/SiO_2

Name	Time [Min]	Area [uV.Min]	C_N	RF	n_i	A_i/C_N	Molar flow rate (mmol C/min)	Selectivity
Methane	1.07	902.6	1	1	902.6	902.6	0.021501212	4%
Ethylene	1.51	37.3	2	1	37.3	18.65	0.000888539	0%
Ethane	1.87	191.7	2	1	191.7	95.85	0.004566566	1%
Propene	4.38	457.3	3	1	457.3	152.43	0.010893535	2%
Propane	4.58	341	3	1	341	113.67	0.008123104	1%
Butene	8.04	493.3	4	1	493.3	123.33	0.011751106	2%
Butane	8.34	494.8	4	1	494.8	123.7	0.011786838	2%
Trans-2-butene	9.16	29.2	4	1	29.2	7.3	0.000695585	0%
Cis-2-butene	9.86	37	4	1	37	9.25	0.000881392	0%
Ethanol	11.48	53.3	2	1.3	69.29	34.645	0.001650586	0%
3-Methyl-1-butene	12.03	27.6	5	1	27.6	5.52	0.000657471	0%
Pentene	12.86	454.5	5	1	454.5	90.9	0.010826835	0%
Pentane	13.85	454.5	5	1	454.5	90.9	0.010826835	0%
Trans-2-pentene	14.33	31.5	5	1	31.5	6.3	0.000750375	0%
Cis-2-pentene	14.72	32.3	5	1	32.3	6.46	0.000769432	0%
Propanol	16.87	14.9	3	1.2	17.88	5.96	0.000425927	0%
2-Methyl-pentane	18.68	13.8	6	1	13.8	2.3	0.000328736	2%
3-Methyl-pentane	18.25	14.2	6	1	14.2	2.3667	0.000338264	0%
Hexene	19.39	363.1	6	1	363.1	60.517	0.008649557	0%
Hexane	19.66	643.6	6	1	643.6	107.27	0.015331465	2%
Trans-2-hexene	20.15	34.3	6	1	34.3	5.7167	0.000817075	0%
Cis-2-hexene	22.19	33.6	6	1	33.6	5.6	0.0008004	0%
Butanol	23.44	27.6	4	1.1	30.36	7.59	0.000723218	0%
2-Methyl-hexane	23.57	13.1	7	1	13.1	1.8714	0.000312061	0%
Heptene	24.16	228.1	7	1	228.1	32.586	0.005433666	0%
Heptane	24.28	555.6	7	1	555.6	79.371	0.01323518	0%
Trans-2-heptene	24.86	59.2	7	1	59.2	8.4571	0.001410228	1%
Cis-2-heptene	25.27	30.2	7	1	30.2	4.3143	0.000719407	3%
Pentanol	27.17	11.5	5	1.1	12.65	2.53	0.000301341	0%
2-Methyl-heptane	27.87	10.2	8	1	10.2	1.275	0.000242978	0%
4-Methyl-heptane	28.5	9.6	8	1	9.6	1.2	0.000228686	0%
Octene	28.98	113.3	8	1	113.3	14.163	0.002698967	0%

Appendix R: Data obtained from GC-FID analysis for $Mn16^{SEA}$-Co/SiO_2 (continuation)

Name	Time [Min]	Area [uV.Min]	C_N	RF	n_i	A_i/C_N	Molar flow rate (mmol C/min)	Selectivity
Octane	30.24	374.1	8	1	374.1	46.763	0.008911593	0%
Trans-2-octene	33.3	23.8	8	1	23.8	2.975	0.00056695	1%
Cis-2-octene	34.24	21.2	8	1	21.2	2.65	0.000505014	2%
2-Methyl-octane	34.73	54.4	9	1	54.4	6.0444	0.001295885	0%
4-Methyl-octane	35.44	20.2	9	1	20.2	2.2444	0.000481193	0%
Nonene	35.59	47.4	9	1	47.4	5.2667	0.001129135	0%
Nonane	36.2	205.3	9	1	205.3	22.811	0.004890537	0%
Trans-2-nonene	41.44	13.4	9	1	13.4	1.4889	0.000319207	0%
Cis-2-nonene	42.16	16.7	9	1	16.7	1.8556	0.000397818	0%
Decene	42.9	18.5	10	1	18.5	1.85	0.000440696	1%
Decane	46.26	100.5	10	1	100.5	10.05	0.002394053	0%
Undecene	47.11	10.5	11	1	10.5	0.954545	0.000250125	0%
Undecene	47.64	64	11	1	64	5.818182	0.001524571	0%
Dodecene	52.03	13.8	12	1	13.8	1.15	0.000328736	0%
Dodecane	56.36	56	12	1	56	4.666667	0.001333999	0%
Tridecane	60.3	37	13	1	37	2.846154	0.000881392	1%

Appendix S: Typical data obtained from GC-FID analysis for $Mn26^{SEA}$-Co/SiO_2

Name	Time [Min]	Area [uV.Min]	C_N	RF	n_i	A_i/C_N	Molar flow rate (mmol C/min)	Selectivity
Methane	1.07	8979.3	1	1	8979.3	8979.3	0.030923087	6%
Ethylene	1.51	269.8	2	1	269.8	134.9	0.000929142	0%
Ethane	1.87	1218.9	2	1	1218.9	609.45	0.004197671	1%
Propene	4.38	3431.7	3	1	3431.7	1143.9	0.011818155	2%
Propane	4.58	1384.7	3	1	1384.7	461.57	0.004768657	1%
Butene	8.04	3327.8	4	1	3327.8	831.95	0.011460342	2%
Butane	8.34	1963.5	4	1	1963.5	490.88	0.006761939	1%
Trans-2-butene	9.16	74.3	4	1	74.3	18.575	0.000255876	0%
Cis-2-butene	9.86	133.3	4	1	133.3	33.325	0.000459061	0%
Ethanol	11.48	418.1	2	1.3	543.53	271.77	0.001871819	0%
3-Methyl-Butane	12.03	69.2	5	1	69.2	13.84	0.000238312	0%
Pentene	12.86	2919.9	5	1	2919.9	583.98	0.010055608	2%
Pentane	13.85	2129.5	5	1	2129.5	425.9	0.007333613	1%
Trans-2-pentene	14.33	83.6	5	1	83.6	16.72	0.000287903	0%
Cis-2-pentene	14.72	113	5	1	113	22.6	0.000389152	0%
2-Methyl-2-Pentane	16.87	28.7	6	1	28.7	4.7833	9.88376E-05	0%
3-Methyly-pentene	18.68	35.8	6	1	35.8	5.9667	0.000123289	0%
Hexene	18.25	2395.1	6	1	2395.1	399.18	0.008248292	2%
Hexane	19.39	2362.4	6	1	2362.4	393.73	0.008135679	2%
Trans-2-hexene	19.66	107.1	6	1	107.1	17.85	0.000368833	0%
Cis-2-hexene	20.15	129.6	6	1	129.6	21.6	0.000446319	0%
2-Methyl-hexane	22.19	13.2	7	1	13.2	1.8857	4.54584E-05	0%
Heptene	23.44	1703.9	7	1	1703.9	243.41	0.005867924	1%
Heptane	23.57	2454.7	7	1	2454.7	350.67	0.008453543	2%
Trans-2-heptene	24.16	116.2	7	1	116.2	16.6	0.000400172	0%
Cis-2-heptene	24.28	136.8	7	1	136.8	19.543	0.000471114	0%
Pentanol	24.86	127.4	5	1.1	140.14	28.028	0.000482617	0%
2-Methyl-heptane	25.27	27.7	8	1	27.7	3.4625	9.53938E-05	0%
4-Methyl-heptane	27.17	10.8	8	1	10.8	1.35	3.71932E-05	0%
Octene	27.87	1013.4	8	1	1013.4	126.68	0.003489967	1%
Octane	28.5	2219.5	8	1	2219.5	277.44	0.007643557	1%
Trans-2-octene	28.98	111.8	8	1	111.8	13.975	0.000385019	0%
Cis-2-octene	30.24	125.8	8	1	125.8	15.725	0.000433232	0%
2-Methyl-octane	33.3	20.1	9	1	20.1	2.2333	6.92208E-05	0%
4-Methyl-octane	34.24	3.2	9	1	3.2	0.3556	1.10202E-05	0%

Appendix S: Data obtained from GC-FID analysis for $Mn26^{SEA}$-Co/SiO_2 (continuation)

Name	Time [Min]	Area [uV.Min]	C_N	RF	n_i	A_i/C_N	Molar flow rate (mmol C/min)	Selectivity
Nonene	34.73	465.2	9	1	465.2	51.689	0.001602065	0%
Nonane	35.44	1549.2	9	1	1549.2	172.13	0.005335165	1%
Trans-2-nonene	35.59	75.6	9	1	75.6	8.4	0.000260353	0%
Cis-2-nonene	36.2	84.4	9	1	84.4	9.3778	0.000290658	0%
Decene	41.44	158.7	10	1	158.7	15.87	0.000546534	0%
Decane	42.16	822.1	10	1	822.1	82.21	0.002831164	1%
Undecane	42.9	324	11	1	324	29.455	0.001115797	0%
Dodecane	46.26	167.6	12	1	167.6	13.967	0.000577184	0%
Tridecane	47.11	93.8	13	1	93.8	7.2154	0.00032303	0%

Appendix T: Data obtained from GC-FID analysis for Mn42^{SEA}-Co/SiO_2

Name	Time [Min]	Area [uV.Min]	C_N	RF	n_i	A_i/C_N	Molar flow rate (mmol C/min)	Selectivity
Methane	1.07	5815.3	1	1	5815.3	5815.3	0.42014591	5%
Ethylene	1.51	273.6	2	1	273.6	136.8	0.019767152	0%
Ethane	1.87	963.4	2	1	963.4	481.7	0.069604074	1%
Propene	4.38	2786.6	3	1	2786.6	928.87	0.20132729	3%
Propane	4.58	1092.5	3	1	1092.5	364.17	0.078931337	1%
Butene	8.04	2648.2	4	1	2648.2	662.05	0.191328117	2%
Butane	8.34	1436.1	4	1	1436.1	359.03	0.103755875	1%
Trans-2-butene	9.16	56.7	4	1	56.7	14.175	0.004096482	0%
Cis-2-butene	9.86	101.3	4	1	101.3	25.325	0.007318759	0%
Ethanol	11.48	385.8	2	1.3	501.54	250.77	0.036235444	0%
3-Methyl-1-butene	12.03	55.9	5	1	55.9	11.18	0.004038684	0%
Pentene	12.86	2328	5	1	2328	465.6	0.168194191	2%
Pentane	13.85	1503.8	5	1	1503.8	300.76	0.108647089	1%
Trans-2-butene	14.33	62	5	1	62	12.4	0.004479399	0%
Cis-2-butene	14.72	81.6	5	1	81.6	16.32	0.005895466	0%
Propanol	16.87	157	3	1.2	188.4	62.8	0.013611592	0%
2-Methyl-pentane	18.68	21.7	6	1	21.7	3.6167	0.001567789	0%
3-Methyl-pentane	18.25	26.1	6	1	26.1	4.35	0.001885682	0%
Hexene	19.39	1969.8	6	1	1969.8	328.3	0.142314827	2%
Hexane	19.66	1667.8	6	1	1667.8	277.97	0.120495821	2%
Trans-2-hexene	20.15	75.6	6	1	75.6	12.6	0.005461976	0%
Cis-2-hexene	22.19	89.4	6	1	89.4	14.9	0.006459004	0%
Butanol	23.44	127.8	4	1.1	140.58	35.145	0.010156675	0%
2-methyl-hexane	23.57	11.4	7	1	11.4	1.6286	0.000823631	0%
Heptene	24.16	1465	7	1	1465	209.29	0.105843853	1%
Heptane	24.28	1748.2	7	1	1748.2	249.74	0.12630459	2%
Trans-2-heptene	24.86	82.9	7	1	82.9	11.843	0.005989389	0%
Cis-2-heptene	25.27	93.1	7	1	93.1	13.3	0.006726323	0%
Pentanol	27.17	100.3	5	1.2	120.36	24.072	0.008695813	0%
2-Methyl-heptane	27.87	17.4	8	1	17.4	2.175	0.001257122	0%
Octene	28.5	880.6	8	1	880.6	110.08	0.063621909	1%
Octane	28.98	1526.8	8	1	1526.8	190.85	0.110308802	1%
Trans-2-octene	30.24	75.2	8	1	75.2	9.4	0.005433077	0%
Cis-2-octene	33.3	80.3	8	1	80.3	10.038	0.005801544	0%
Hexanol	34.24	35.6	8	1	35.6	4.45	0.002572042	0%
Unknown	34.73	84.453	8	1	84.4526	10.557	0.006101562	0%
2-Methyl-Octane	35.44	11.7	9	1	11.7	1.3	0.000845306	0%

Appendix T: Data obtained from GC-FID analysis for $Mn42^{SEA}$-Co/SiO_2 (continuation)

Name	Time [Min]	Area [uV.Min]	C_N	RF	n_i	A_i/C_N	Molar flow rate (mmol C/min)	Selectivity
Nonene	35.59	385.1	9	1	385.1	42.789	0.027822845	0%
Nonane	36.2	995.7	9	1	995.7	110.63	0.071937696	1%
Trans-2-nonene	41.44	46.9	9	1	46.9	5.2111	0.003388448	0%
Cis-2-nonene	42.16	51.4	9	1	51.4	5.7111	0.003713566	0%
Decene	42.9	127.9	10	1	127.9	12.79	0.009240566	0%
Decane	46.26	503.3	10	1	503.3	50.33	0.036362601	0%
Undecane	47.11	198.9	11	1	198.9	18.082	0.0143702	0%
Tridecane	47.64	0.6	11	1	0.6	0.0545	4.3349E-05	0%

Appendix U: Data obtained from GC-FID analysis for $Mn55^{SEA}$-Co/SiO_2

Name	Time [Min]	Area [uV.Min]	C_N	RF	n_i	A_i/C_N	Molar flow rate (mmol C/min)	Selectivity
Methane	1.07	3154.8	1	1	3154.8	3154.8	0.030274814	8%
Ethylene	1.51	161.1	2	1	161.1	80.55	0.001545985	0%
Ethane	1.87	523	2	1	523	261.5	0.005018932	1%
Propene	4.38	1301.1	3	1	1301.1	433.7	0.012485914	3%
Propane	4.58	565.8	3	1	565.8	188.6	0.00542966	1%
2-Methyl-1-propane	8.04	32.5	4	1	32.5	8.125	0.000311884	0%
Butene	8.34	1242.2	4	1	1242.2	310.55	0.011920684	3%
Butane	9.16	719.5	4	1	719.5	179.88	0.006904631	2%
Trans-2-butene	9.86	25.5	4	1	25.5	6.375	0.000244709	0%
Cis-2-butene	11.48	36.7	4	1	36.7	9.175	0.000352189	0%
Ethanol	12.03	151.5	2	1.3	196.95	98.475	0.001890017	1%
3-Methyl-butane	12.86	7.1	5	1	7.1	1.42	6.81346E-05	0%
Pentene	13.85	1055.7	5	1	1055.7	211.14	0.01013095	3%
Pentane	14.33	712.7	5	1	712.7	142.54	0.006839375	2%
Trans-2-pentene	14.72	26.9	5	1	26.9	5.38	0.000258144	0%
Cis-2-pentene	16.87	28.1	5	1	28.1	5.62	0.00026966	0%
Propanol	18.68	82.8	3	1.2	99.36	33.12	0.000953501	0%
2-Methyl-pentane	18.25	12.8	6	1	12.8	2.1333	0.000122834	0%
3-Methyl-pentene	19.39	2.5	6	1	2.5	0.4167	2.39911E-05	0%
Hexene	19.66	900.8	6	1	900.8	150.13	0.008644463	2%
Hexane	20.15	708.5	6	1	708.5	118.08	0.00679907	2%
Trans-2-hexene	22.19	24.8	6	1	24.8	4.1333	0.000237991	0%
Cis-2-hexane	23.44	28.7	6	1	28.7	4.7833	0.000275418	0%
Butanol	23.57	49.8	4	1.1	54.78	13.695	0.000525692	0%
2-Methyl-hexane	24.16	24.1	7	1	24.1	3.4429	0.000231274	0%
Heptene	24.28	709.8	7	1	709.8	101.4	0.006811545	2%
Heptane	24.86	697.3	7	1	697.3	99.614	0.00669159	2%
Trans-2-heptene	25.27	29.7	7	1	29.7	4.2429	0.000285014	0%
Cis-2-heptene	27.17	31.8	7	1	31.8	4.5429	0.000305166	0%
Pentanol	27.87	38.8	5	1.1	42.68	8.536	0.000409576	0%
2-Methyl-heptane	28.5	10	8	1	10	1.25	9.59643E-05	0%
4-Methyl-heptane	28.98	6.9	8	1	6.9	0.8625	6.62154E-05	0%
Octene	30.24	519.9	8	1	519.9	64.988	0.004989183	1%
Octane	33.3	651.3	8	1	651.3	81.413	0.006250154	2%
Trans-2-octene	34.24	28.6	8	1	28.6	3.575	0.000274458	0%
Cis-2-octene	34.73	30.5	8	1	30.5	3.8125	0.000292691	0%

Appendix U: Data obtained from GC-FID analysis for $Mn55^{SEA}$-Co/SiO_2 (continuation)

2-Methyl-octane	**35.44**	**10.3**	**9**	**1**	**10.3**	**1.1444**	**9.88432E-05**	**0%**
4-Methyly-octane	35.59	3.2	9	1	3.2	0.3556	3.07086E-05	0%
Nonene	36.2	338.5	9	1	338.5	37.611	0.003248391	1%
Nonane	41.44	558.5	9	1	558.5	62.056	0.005359606	1%
Trans-2-nonene	42.16	23.9	9	1	23.9	2.6556	0.000229355	0%
Cis-2-nonene	42.9	27.5	9	1	27.5	3.0556	0.000263902	0%
Decene	46.26	186.5	10	1	186.5	18.65	0.001789734	0%
Decane	47.11	439.3	10	1	439.3	43.93	0.004215711	1%
Undecene	47.64	79	11	1	79	7.1818	0.000758118	0%
Undecane	52.03	267.5	11	1	267.5	24.318	0.002567045	1%
Dodecane	56.36	117.2	12	1	117.2	9.7667	0.001124701	0%

Appendix V: Data obtained from GC-FID analysis for $Mn16^{IMPR}$-Co/SiO_2

Name	Time [Min]	Area [uV.Min]	C_N	RF	n_i	A_i/C_N	Molar flow rate (mmol C/min)	Selectivity
Methane	1.07	6161.5	1	1	6161.5	6161.5	0.030793734	5%
Ethylene	1.51	168.5	2	1	168.5	84.25	0.000842124	0%
Ethane	1.87	657.9	2	1	657.9	328.95	0.00328803	1%
Propene	4.38	1712.2	3	1	1712.2	570.7333	0.008557175	1%
Propane	4.58	840.6	3	1	840.6	280.2	0.004201122	1%
Butene	8.04	1692.2	4	1	1692.2	423.05	0.008457219	1%
Butane	8.34	1182.8	4	1	1182.8	295.7	0.005911357	1%
Trans-2-butene	9.16	51.8	4	1	51.8	12.95	0.000258884	0%
Cis-2-butene	9.86	75.6	4	1	75.6	18.9	0.000377831	0%
Ethanol	11.48	257.4	2	1.3	334.62	167.31	0.001672352	0%
Pentene	12.86	1438.9	5	1	1438.9	287.78	0.007191285	1%
Pentane	13.85	1297.3	5	1	1297.3	259.46	0.006483602	1%
Trans-2-pentene	14.33	64.4	5	1	64.4	12.88	0.000321856	0%
Cis-2-pentene	14.72	69.9	5	1	69.9	13.98	0.000349344	0%
Propanol	16.87	66.9	3	1.2	80.28	26.76	0.000401221	0%
2-Methyl-pentane	18.68	0	6	1	0	0	0	0%
3-Methyl-pentane	18.25	0	6	1	0	0	0	0%
Hexene	19.39	1325.2	6	1	1325.2	220.8667	0.006623039	1%
Hexane	19.66	1577.3	6	1	1577.3	262.8833	0.007882976	1%
Trans-2-hexene	20.15	89.2	6	1	89.2	14.86667	0.000445801	0%
Cis-2-hexene	22.19	78.2	6	1	78.2	13.03333	0.000390825	0%
Butanol	23.44	69.6	4	1.1	76.56	19.14	0.000347845	0%
2-Methyl-hexane	23.57	0	7	1	0	0	0	0%
Heptene	24.16	981.1	7	1	981.1	140.1571	0.004903308	1%
Heptane	24.28	1674.6	7	1	1674.6	239.2286	0.008369259	1%
Trans-2-heptene	24.86	85.1	7	1	85.1	12.15714	0.00042531	0%
Cis-2-heptene	25.27	82.6	7	1	82.6	11.8	0.000412815	0%
Pentanol	27.17	72.1	5	1.1	79.31	15.862	0.000360339	0%
2-Methyl-heptane	27.87	0	8	1	0	0	0	0%
4-Methyl-heptane	28.5	0	8	1	0	0	0	0%
Octene	28.98	645	8	1	645	80.625	0.003223559	1%
Octane	30.24	1562.5	8	1	1562.5	195.3125	0.007809009	1%
Trans-2-octene	33.3	81.1	8	1	81.1	10.1375	0.000405319	0%
Cis-2-octene	34.24	77.3	8	1	77.3	9.6625	0.000386327	0%
2-Methyl-octane	34.73	52.6	9	1	52.6	5.844444	0.000262882	0%
4-Methyl-octane	35.44	347.3	9	1	347.3	38.58889	0	0%
Nonene	35.59	1199.4	9	1	1199.4	133.2667	0.001735724	0%
Nonane	36.2	63.8	9	1	63.8	7.088889	0.00599432	1%
Trans-2-nonene	41.44	60.3	9	1	60.3	6.7	0.000318857	0%

Appendix V: Data obtained from GC-FID analysis for $Mn16^{IMPR}$-Co/SiO_2 (continuation)

Cis-2-nonene	**42.16**	**186.9**	**9**	**1**	**186.9**	**20.76667**	**0.000301365**	**1%**
Decene	42.9	309.2	10	1	309.2	30.92	0.001545309	0%
Decane	46.26	890.2	10	1	890.2	89.02	0.004449011	1%
Undecene	47.11	135.4	11	1	135.4	12.30909	0.000676697	0%
Undecene	47.64	977.2	11	1	977.2	88.83636	0.004883817	1%
Dodecene	52.03	73.1	12	1	73.1	6.091667	0.000365337	0%
Dodecane	56.36	707.7	12	1	707.7	58.975	0.003536919	1%
Tridecane	60.3	308	13	1	308	23.69231	0.001539312	0%

Appendix W: Data obtained from GC-FID analysis for $Mn26^{IMPR}$-Co/SiO_2

Name	Time [Min]	Area [uV.Min]	C_N	RF	n_i	A_i/C_N	Molar flow rate (mmol C/min)	Selectivity
Methane	1.07	9403.9	1	1	9403.9	9403.9	0.0317	6%
Ethylene	1.51	408.4	2	1	408.4	204.2	0.001376693	0%
Ethane	1.87	1373.2	2	1	1373.2	686.6	0.004628977	1%
Propene	4.38	2878.9	3	1	2878.9	959.63	0.009704604	2%
Propane	4.58	1516.3	3	1	1516.3	505.43	0.005111359	1%
Butene	8.04	2843.8	4	1	2843.8	710.95	0.009586284	2%
Butane	8.34	2101.7	4	1	2101.7	525.43	0.007084708	1%
Trans-2-butene	9.16	272	4	1	272	68	0.000916896	0%
Cis-2-butene	9.66	354.7	4	1	354.7	88.675	0.001195673	0%
Ethanol	11.48	441.4	2	1.3	573.82	286.91	0.001934314	0%
3-Methyl-butane	12.03	107.4	5	1	107.4	21.48	0.000362039	0%
4-Methyl-butane	12.83	95.1	5	1	95.1	19.02	0.000320577	0%
Pentene	12.86	2530.4	5	1	2530.4	506.08	0.008529831	2%
Pentane	13.85	2345.5	5	1	2345.5	469.1	0.007906544	2%
Trans-2-pentene	14.33	306.5	5	1	306.5	61.3	0.001033194	0%
Cis-2-pentene	14.72	420.1	5	1	420.1	84.02	0.001416133	0%
Propanol	16.87	432.2	3	1.2	518.64	172.88	0.001748305	0%
Hexene	19.39	2213.8	6	1	2213.8	368.97	0.007462591	1%
Hexane	19.66	2582.7	6	1	2582.7	430.45	0.008706131	2%
Trans-2-hexene	20.15	510.3	6	1	510.3	85.05	0.001720192	0%
Cis-2-hexene	22.19	547.5	6	1	547.5	91.25	0.001845591	0%
Butanol	23.44	597.9	4	1	597.9	149.48	0.002015486	0%
Heptene	24.16	2017.3	7	1	2017.3	288.19	0.006800201	1%
Heptane	24.28	2656.9	7	1	2656.9	379.56	0.008956255	2%
Trans-2-heptene	24.86	376.4	7	1	376.4	53.771	0.001268823	0%
Cis-2-heptene	25.27	626.2	7	1	626.2	89.457	0.002110884	0%
Pentanol	27.17	488.6	5	1	488.6	97.72	0.001647042	0%
Octene	28.98	1651.7	8	1	1651.7	206.46	0.005567785	1%
Octane	30.24	2342	8	1	2342	292.75	0.007894746	2%
Trans-2-octene	33.3	422.3	8	1	422.3	52.788	0.001423549	0%
Cis-2-octene	34.24	473.4	8	1	473.4	59.175	0.001595804	0%
2-Methyl-octane	34.73	173.2	9	1	173.2	19.244	0.000583847	0%
Nonene	35.59	1204.6	9	1	1204.6	133.84	0.004060637	1%

Appendix W: Data obtained from GC-FID analysis for $Mn26^{IMPR}$-Co/SiO_2 (continuation)

Nonane	**36.2**	**1704.8**	**9**	**1**	**1704.8**	**189.42**	**0.005746782**	**1%**
Trans-2-nonene	41.44	285.4	9	1	285.4	31.711	0.000962067	0%
Cis-2-nonene	42.16	360.6	9	1	360.6	40.067	0.001215562	0%
Decene	42.9	428.5	10	1	428.5	42.85	0.001444449	0%
Decane	46.26	1288	10	1	1288	128.8	0.004341773	1%
Undecene	47.11	481.9	11	1	481.9	43.809	0.001624457	0%
Undecane	47.64	1474.1	11	1	1474.1	134.01	0.004969105	1%
Dodecene	52.03	331.9	12	1	331.9	27.658	0.001118816	0%
Dodecane	56.36	1077.2	12	1	1077.2	89.767	0.003631179	1%
Tridecane	60.3	279.7	13	1	279.7	21.515	0.000942852	0%

9 ETHICS CLEARANCE FORM

Application for Approval of Ethics in Research (ER) Projects
Faculty of Engineering and the Built Environment, University of Cape Town

ETHICS APPLICATION FORM

Please Note:
Any person planning to undertake research in the Faculty of Engineering and the Built Environment (EBE) at the University of Cape Town is required to complete this form **before** collecting or analysing data. The objective of submitting this application prior to embarking on research is to ensure that the highest ethical standards in research, conducted under the auspices of the EBE Faculty, are met. Please ensure that you have read, and understood the **EBE Ethics in Research Handbook** (available from the UCT EBE, Research Ethics website) prior to completing this application form: http://www.ebe.uct.ac.za/ebe/research/ethics

APPLICANT'S DETAILS		
Name of principal researcher, student or external applicant		SILETSHENKOSI MATIE
Department		CHEMICAL ENGINEERING DEPARTMENT
Preferred email address of applicant:		MTHSIL004@myuct.ac.za
If Student:	Your Degree: e.g., BSc, PhD, etc.	MSc
	Credit Value of Research: e.g., 60/120/180/360 etc.	60/120
	Name of Supervisor (if supervised):	ERIC VAN STEEN
If this is a research contract, indicate the source of funding/sponsorship		C*CHANGE
Project Title		EFFECT OF MANGANESE ON SELECTIVITY & ACTIVITY ON CO/SiO2 FISCHER TROPCH SYNTHESIS

I hereby undertake to carry out my research in such a way that:

- there is no apparent legal objection to the nature or the method of research; and
- the research will not compromise staff or students or the other responsibilities of the University;
- the stated objective will be achieved, and the findings will have a high degree of validity;
- limitations and alternative interpretations will be considered;
- the findings could be subject to peer review and publicly available; and
- I will comply with the conventions of copyright and avoid any practice that would constitute plagiarism.

APPLICATION BY	Full name	Signature	Date
Principal Researcher/ Student/External applicant	SILETSHENKOSI MATIE	Signed by candidate	10/11/2020
SUPPORTED BY	**Full name**	**Signature**	**Date**
Supervisor (where applicable)	ERIC VAN STEEN		10/11/20

APPROVED BY	Full name	Signature	Date
HOD (or delegated nominee) Final authority for all applicants who have answered NO to all questions in Section 1; and for all Undergraduate research (including Honours).	Prof H von Blottnitz		7 March 2021
Chair: Faculty EIR Committee For applicants other than undergraduate students who have answered YES to any of the questions in Section 1			